

**This dissertation has been
microfilmed exactly as received**

68-15,659

**SCHIELD, Milo Arvid, 1940-
THE CONFIGURATION OF GEOMAGNETIC FIELD
LINES ABOVE THE AURORAL ZONES.**

**Rice University, Ph.D., 1968
Geophysics**

University Microfilms, Inc., Ann Arbor, Michigan

RICE UNIVERSITY

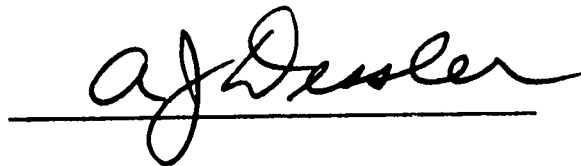
THE CONFIGURATION OF GEOMAGNETIC
FIELD LINES ABOVE THE AURORAL ZONES

by
MILO A. SCHIELD

A THESIS SUBMITTED
IN PARTIAL FULFILLMENT OF THE
REQUIREMENTS FOR THE DEGREE OF

DOCTOR OF PHILOSOPHY

Thesis Director's Signature:



Houston, Texas

May, 1968

TABLE OF CONTENTS

	Page
I. INTRODUCTION	1
A. The geomagnetic field	7
B. The auroral oval	10
II. BOUNDARY BETWEEN A MAGNETIC FIELD AND A PLASMA	13
A. Physics of the boundary layer	13
B. Methods of calculating the boundary surface	16
III. INTERNAL PRESSURES	24
A. The quiet-day ring current field	24
B. The neutral-sheet tail field	33
IV. COMPUTATIONAL DETAILS	37
A. Detailed explanation of computer programs	40
B. Comparison with Mead's work	51
V. GEOMAGNETIC FIELD CONFIGURATION	56
A. Effects of the quiet-day ring current	56
B. Effect of the tail-current field	66
C. Calibration of the model	70
D. Discussion	80

	Page
VI. THE ALFVÉN LAYER AND FIELD-ALIGNED CURRENTS	86
A. Introduction	86
B. Size of the forbidden region	92
C. Auroral zones and the Alfvén layer	98
D. Field-aligned currents and the Alfvén layer	100
E. Energy dependence of particles in the Alfvén layer	108
F. Nature of particles in the field-aligned currents	113
G. Discussion	120
VII. CONCLUSION	122
APPENDIX	128
ACKNOWLEDGMENTS	130
BIBLIOGRAPHY	131
FIGURE CAPTIONS	141
FIGURES	

I. INTRODUCTION

Auroral theory has been largely concerned with how to take solar wind plasmas, accelerate them to auroral energies, and inject them upon the auroral zone. Although a number of acceleration mechanisms have been proposed, auroral theories may be divided into two broad categories, based on how they treat the problem of injection.

The older and most widely applied approach has been to assert that the location of the auroral zones is specified entirely by the geomagnetic field configuration. This was first applied by Störmer (1912) in describing the motion of noninteracting particles in a dipole magnetic field. He noted the existence of cutoff latitudes below which solar particles could not reach the earth's surface. Chapman and Ferraro (1931, 1932, 1933), in describing the containment of the geomagnetic field to a cavity within a streaming plasma, suggested that solar plasma, upon injection into the two neutral points on the noon meridian, would intersect the atmosphere at the observed auroral zones. Johnson (1960), in describing the shape of the magnetosphere as a teardrop, implied that the field lines through the auroral zone formed the boundary of the polar cap field lines. These are field lines which intersect the earth above the surface latitude of the

field line through the noon-meridian neutral points. Each of these closed-tail magnetospheric configurations had difficulty in explaining the nighttime aurora, where auroral field lines had no direct relation to those which formed the surface of the magnetosphere. Dessler and Juday (1965), using the open-tail model (See Figure 1), proposed the auroral zone was on the equatorward boundary of the open-tail field lines, thus deriving a quasi-circular auroral zone on the earth's surface. The subsequent discovery of the neutral sheet (Ness, 1965) provided a new region of possible particle energization. The associated auroral theories (Speiser, 1967) necessarily asserted that the auroral zone was defined by the geomagnetic field configuration, specifically by the boundary between field lines which closed within the magnetosphere and field lines which were open to 'infinity' (i.e., they closed beyond 15 to 30 R_E behind the earth).

A second category of auroral theories asserted that the field lines through the auroral zone were specified by the magnetospheric configuration of both electric and magnetic fields. The geomagnetic field configuration was necessary but not sufficient. Alfvén (1939) noted the existence of a forbidden region - a region inside which particles could not drift under the influence of an

external electric field. The existence of a charge separation along the outer boundary of this forbidden region was used to create polar disturbances. The auroral zone was identified by those field lines which passed through the outer boundary of the forbidden zone (the Alfvén layer. See Chapter VI). The source of this electric field was the interaction of the streaming solar wind and northward directed interplanetary field $\bar{E} = -\bar{v} \times \bar{B} = (.1 \text{ mv/m})v(100 \text{ km/sec}) B(\gamma)$. In the unifying theory of Axford and Hines (1961), the auroral zone was specifically placed on closed field lines at a slightly lower latitude than that of the zone of confusion - a zone identified as the location at which the field line to the neutral point intersects the earth. The proposed circulation pattern for energetic particles depicted Alfvén's boundary of the forbidden region (including the effects of charge separation). However, the relationship between the Alfvén boundary and the auroral zone was not examined. The calculations of Taylor and Hones (1965) indicated that the auroral oval corresponded with an equipotential contour of the magnetospheric electric field, a contour which was equipotential with the surface of the magnetopause.

The validity of the first category of theories became doubtful when the first self-consistent solution of the geomagnetic configuration by Mead (1964) indicated the field line to the neutral point intersected the earth at between 80° and 85° as the subsolar distance to the magnetopause increased from 5 to 15 R_E . Since the daytime aurora are observed well below these latitudes (75° - 78° , Bates, 1966), Dessler and Juday (1965) proposed that inclusion of the quiet-day ring current would lower the neutral-point field-line surface latitude to the observed latitude for quiet-day auroras.

Based on this prediction, the initial purpose of this thesis was:

(1) The calculation of the shape of the magnetosphere and the dayside configuration of the geomagnetic field in a self-consistent manner, while including the quiet-day ring current field; and the analysis of the effect of the quiet-day ring current field upon the surface latitude of the field lines which intersect the neutral points in the noon-meridian plane.

This calculation indicated that the dayside aurora occurred on field lines which did not extend into the geomagnetic tail, but were closed within the magnetosphere. Based on this result, the purpose of this thesis was

expanded to include:

(2) The calculation of the nightside configuration of the geomagnetic field and the evaluation of the mapping of the auroral oval onto the equatorial plane.

These calculations predicted that the mapping of the auroral oval onto the equatorial plane would be similar to the location of the inner boundary of the plasma sheet observed by Vasyliunas. Alfvén's electric field theory of the aurora (See Chapter VI-A) predicted that the auroral zone would be located on field lines which intersected the inner boundary (described here as the Alfvén layer) of a plasma being convected into a dipole field. In order to analyze quantitatively the applicability of Alfvén's theory to this plasma sheet boundary, the purpose of the thesis was expanded to show that:

(3) The concept that the inner boundary of the plasma sheet is an Alfvén layer of unbalanced charge would be sufficient to explain:

- (a) the location of this boundary
- (b) the magnitude of the transverse magnetic disturbances (assuming these disturbances are produced by the field-aligned currents necessary to neutralize the excess charge in a thick Alfvén layer)

- (c) the width of the zone of these transverse magnetic disturbances
- (d) the energy dependence of particles in the Alfvén layer.

A. The Geomagnetic Field.

The general configuration of the geomagnetic field has been qualitatively understood for some time. The confinement of the geomagnetic field by the solar plasma was first suggested by Birkeland (1908) based on laboratory experiments with a terella. Quantitative calculations were made by Chapman and Ferraro (1931, 1932, 1933). The solar plasma was assumed to be free of any interplanetary field and the earth's dipole field was assumed to be free of any internal plasmas. The size of the magnetosphere was estimated by solving for the distance at which the geomagnetic field pressure balanced the solar wind pressure. (See Schiold, 1968 for a review.) The existence of two points in the noon meridian of no net magnetic field (neutral points) was also predicted. The existence of a shock upstream from the earth was predicted (Axford, 1962; Dessler, 1962; Kellogg, 1962; and others). Early observations confirmed the existence of the Chapman-Ferraro boundary between the solar wind and the magnetosphere (Freeman et al., 1963), the existence of a region of quasi-thermalized plasma outside the magnetosphere, as well as observing the presence of a region of high fluxes for low energy electrons. (See Freeman, 1964 and references therein.)

The nightside of the magnetosphere was also investigated theoretically. Johnson (1960) predicted the magnetosphere would have a teardrop shape because of transverse pressures in the solar wind. Dessler (1964) argued that the geomagnetic tail would be blown open by hydromagnetic waves to distances of several hundred earth radii. Following the discovery of a neutral sheet in the magnetospheric tail (Ness, 1965) Dessler and O'Brien (Johnson, 1965) indicated (Figure 1a) that the neutral sheet terminated at a neutral line through which auroral zone field lines pass in accordance with the Dessler-Juday (1965) theory. An alternative configuration was proposed by Axford et al. (1965) (Figure 1b). Their model does not have a true neutral sheet. The equatorial magnetic field was directed northward out to several hundreds of earth radii (See Dessler and Michel, 1966 for a review of magnetospheric models). More recently, Dessler (1968) has illustrated the geomagnetic field (Figure 2) in agreement with the configuration of Axford et al. but with the neutral line located about $20 R_E$ downstream from the earth.

Thus, the only points of theoretical debate on the geomagnetic configuration are quantitative. These quantities are the location of the two neutral points in the noon-meridian plane and of the neutral line in the tail,

as well as the surface latitude of the field lines which passed through these neutral points and the neutral line.

B. The Auroral Oval.

Recent studies of the aurora indicate that auroral arcs tend to lie in an oval belt encircling the geomagnetic poles. Such an oval shaped zone for visual aurora was first suggested by Feldstein and substantiated by later research. (See Feldstein, 1966 for a review.) The location of the auroral oval is based on statistical data of the latitudinal variation of the auroral occurrence frequency. The statistical data used by Feldstein is taken from the ascaplots (all sky camera plots) compiled during the International Geophysical Year 1957 to 1959 for the Northern Hemisphere (Annals of the IGY, 1962). The probability of seeing an aurora was taken to be the ratio between the number of half hour intervals with an aurora in the zenith to the total number of intervals under observation, assuming one could see an aurora if it were present.

The region of magnetic latitude and local time in which the auroral occurrence probability exceeds 60% per half hour is shown in Figure 3. (From McDiarmid and Burrows, 1967 based upon Figure 2 of Feldstein, 1966.) This auroral oval ranged from 65° to 71° at midnight to between 75° and 77° near noon. However, this auroral oval was obtained without discriminating according to magnetic activity.

The dependence of the auroral belt upon the local magnetic activity (the Q index) is illustrated in Figure 4 for $Q \approx 0$ and for $Q = 6$. (See Figure 2 of Feldstein and Starkov, 1967.) The configuration of the auroral oval was found to be more closely related to this local parameter of magnetic activity than to planetary indices Q_p or K_p . In moving from magnetically quiet times to magnetically disturbed periods, in the night the auroral oval expands equatorward, while during the day it is displaced equatorward. For $Q \approx 0$ the auroral oval is located between 70° and 72° (night) and between 76° and 78° (day). For increased magnetic activity, $Q = 6$, the auroral oval shows increasing symmetry and is located between 59° and 74° (midnight) and between 72° and 75° noon.

The center line of the auroral belt is at 67° near midnight for Q between 2 and 6. Since most aurora occur near midnight, this interpretation accounts for the 67° latitude of the auroral zone. The auroral zone is defined as the latitude of maximum auroral activity independent of local time.

Although this data was all acquired during a period of maximum solar activity, Feldstein and Starkov (1967) have concluded that the distribution of auroral displays

II. THE BOUNDARY BETWEEN A MAGNETIC FIELD AND A PLASMA.

A. Physics of the Boundary Layer.

The confinement of a magnetic field by a plasma (or vice versa) has been the subject of considerable attention for both theoretical and practical reasons (Ferraro, 1952; Rosenbluth, 1954; and Weibel, 1959). The problem has been that although a magnetic field-plasma boundary must satisfy Maxwell's equation, the solution must be self-consistent with the motion of the plasma particles. Theoretical studies of the equilibrium boundary have been carried out in a reference frame in which the plasma is at rest, or is streaming in a direction which is perpendicular to the boundary.

The steady-state boundary condition may be obtained from Maxwell's equations, the force equation, and the frozen in flux condition. (See Spitzer, 1962 for a review) These are expressed by:

$$(1) \quad \begin{array}{ll} \bar{\nabla} \times \bar{B} = \mu_0 \bar{j} & \bar{\nabla} \times \bar{E} = 0 \\ \bar{\nabla} p = \bar{j} \times \bar{B} & \bar{E} = -\bar{v} \times \bar{B} \end{array}$$

These equations may be combined to solve for the pressure gradient $\bar{\nabla} p$ in terms of the magnetic field \bar{B} :

$$(2) \quad \bar{\nabla} p = \left[(\bar{\nabla} \times \bar{B}) / \mu_0 \right] \times \bar{B} = \left[(\bar{B} \cdot \bar{\nabla}) \bar{B} - \bar{\nabla} (B^2) / 2 \right] / \mu_0$$

This equation is often called the magnetostatic equation. In a plasma-free magnetic field, the tension must balance the stresses produced by the mutual repulsion of the field lines. The tension term is ignorable whenever $\nabla_{\perp} B \gg \nabla_{\parallel} B$, or whenever the radius of curvature of the field lines is much larger than the thickness of the boundary layer. If the tension is ignorable, the magnetostatic equation may be integrated to:

$$(3) \quad P + B^2/2\mu_0 = \text{constant}$$

This equation has been the basis of nearly all of the magnetospheric modeling to date. The stability of various configurations based on this relationship has been investigated (Sen, 1965; Spitzer, 1962; and Lerche, 1966). The possibility of a more fundamental problem has been raised by Parker (1967) and Lerche (1967) involving the inability of a beam that has a tangential velocity across the boundary to confine the magnetic field. However, this pressure balance equation appears to be valid across the magnetopause (Siscoe and Formisano, 1968) and within the geomagnetic tail and across the neutral sheet (Lazarus et. al., 1968). Therefore, the magnetostatic pressure relation has been used in the following analysis, ignoring the tension. The basic problem of

solving for the boundary of the magnetopause is contained in the pressure balance equation. The body pressure applied by a shocked hypersonic solar wind on a blunt-nosed body is given by:

$$(4) \quad P = P_0 \cos^2 \chi$$

where P_0 is the pressure at the subsolar point and where χ is the angle between the surface normal and the interplanetary solar wind velocity vector (Lees, 1964). Schild (1968) has reviewed the relation between the subsolar body pressure P_0 and the unshocked momentum flux ρv^2 . Mathematically, the pressure balance relation becomes an integro-differential equation. The body pressure of the solar wind depends upon the slope of the surface while the total field B includes the surface current field, a field evaluated by integrating over the surface currents on the boundary of the magnetosphere. Since the location of the surface depends upon the shape of the surface and upon the total magnetic field B , which in turn depends upon the shape of the surface, etc., a self-consistent solution is required. Several techniques are available to solve this problem.

multipole and having considerable geomagnetic relevance, has been of sufficient complexity to preclude the investigation of higher order multipoles. Beard (1964) has reviewed the various approximation methods used to solve for the surface between a three-dimensional dipole and a diamagnetic plasma.

The self-consistent field method. The magnetic field B at any point is the sum of the internal field and the surface current fields. The internal field includes the dipole field and the quiet-day ring current field. The surface current field is the field produced by the sheet current J flowing on the surface of the magnetosphere. The field produced by these surface currents is given by:

$$(5) \quad \bar{B}_{\text{surface}}(r) = \int \left[(\bar{J} \times \hat{r}') / r'^2 \right] dA$$

where the integral is over the entire surface, where $\hat{r}' = \bar{r} - \bar{r}_{\text{source}}$, and where \bar{J} is the surface current at \bar{r}_{source} . Consider the field at a point a inside the boundary, but infinitesimally close to point P which lies on the surface. The field at point a produced by the surface current at point P will be identical to that produced by an infinite-plane current sheet having the same current density everywhere as that flowing at point P .

This portion of the surface current can be separated out and its field designated as the planor field.

$$(6) \quad \bar{B}_{\text{planor}}^{\text{inside}}(r) = \hat{n}_s \times \bar{J}$$

where \hat{n}_s is the outward normal to the surface. The field due to the remainder of the surface current is designated as the curvature field (Mead, 1964) and is defined by:

$$(7) \quad \bar{B}_{\text{curvature}}(r) = \int_{r' > 0} \left[(\bar{J} \times \hat{r}') / r'^2 \right] dA$$

The restriction of $r' > 0$ illustrates the removal of the planor field produced by the currents that are infinitesimally close to the observation point. Not only has the apparent singularity in the integrand been removed, but the primary component of the surface current field has been calculated analytically.

At the point a just inside the surface, the total field is

$$(8) \quad \bar{B}(a) = \bar{B}_{\text{internal}} + \bar{B}_{\text{curvature}} + \bar{B}_{\text{planor}}$$

Now consider the field at point b infinitesimally close to point a but across the boundary from it. The internal field and the curvature field are unchanged by this infinitesimal change in the observation point. The planor

field, however, reverses sign so that the total field at b is given by:

$$(9) \quad \bar{B}(b) = (\bar{B}_{\text{internal}} + \bar{B}_{\text{curvature}}) - \bar{B}_{\text{planor}}$$

If the total field outside the magnetopause $B(b)$ produced by currents within the magnetopause is zero, then the planor field can be eliminated from Equation (8) so that:

$$(10) \quad \bar{B}(a) = 2(\bar{B}_{\text{internal}} + \bar{B}_{\text{curvature}})$$

The surface current in Equation (7) may be expressed in terms of the total geomagnetic field. From Maxwell's equations, $\oint \bar{B} \cdot d\bar{\ell} = \mu_0 \int \bar{J} \cdot d\bar{s}$ so that for an infinitesimal area $|\bar{B}_{\text{tang}}^{\text{out}}| - |\bar{B}_{\text{tang}}^{\text{inside}}| = \mu_0 |\bar{J}|$ where \bar{J} is the sheet current per unit length. Since the magnetic field outside the magnetosphere, produced by the currents within the magnetosphere, is zero, $|\mu_0 \bar{J}|$ equals $|\bar{B}_{\text{total}}^{\text{inside}}|$. It can be shown that the surface current necessary to confine the geomagnetic field within the magnetopause is given by:

$$(11) \quad \mu_0 \bar{J} = (\bar{B}_{\text{total}}^{\text{inside}} \times \hat{n}_s)$$

Equation (11) can be used to eliminate the surface current from Equation (8) so that:

$$(12) \quad \bar{B}_{\text{curvature}} = \int_{r' > 0} \left\{ \left[(\bar{B}_{\text{total}}^{\text{inside}} \times \hat{n}_s) \times \hat{r}' \right] / r'^2 \right\} dA$$

second-order surface, etc. On the fourth iteration, the ratio of the total field to the dipole field was less than one percent at approximately 1.5 and 2.0 times the subsolar radius away from the earth outside the magnetosphere.

Moment technique. Midgley and Davis (1962, 1963) introduced the moment technique and applied it to both a streaming plasma and an isotropic plasma incident on a dipole field. The moment technique consists of replacing the usual boundary conditions with two equivalent conditions:

$$(14) \quad \left. \begin{array}{l} B_N = 0 \\ (B_{\text{tang}})^2 / 2\mu_0 = P_N \end{array} \right\} \text{replaced by} \left\{ \begin{array}{l} B_{\text{total}}^{\text{outside}} = 0 \\ j^2 = 2\mu_0 P \end{array} \right.$$

This iteration process involved the variation of 46 free parameters to achieve convergence and, necessarily, involved constant manual smoothing to prevent wandering. The ratios of the net field to the original dipole field outside the boundary are typically ten per cent at about 1.5 times the subsolar distance.

Free surface solution. Slutz (1962) utilized a method developed by Treffitz (1916) for finding a surface free to move in seeking equilibrium between pressures on its two sides. Slutz presented solutions for an isotropic

plasma and also for a streaming plasma with a small constant static pressure incident upon a dipole field.

(iii) Discussion and comparison of the methods for calculating magnetospheric boundaries.

One would expect that the shape of the first-order approximation surface would be inaccurate where local surface currents are small, or where the radius of curvature becomes small. In each case, the curvature field contributes significantly to the total geomagnetic field.

The first-order iteration is fairly accurate when applied to the line dipole. Perhaps this is due to the fact that with the exception of the distant tail region the radius of curvature is largest in the polar regions where the surface current is the smallest. And for the same reason, the first-order approximation is quite inaccurate in treating the isotropic plasma pressure problem because the radius of curvature is smallest where the surface currents are largest, the polar region. Yet due to the symmetry of the problem, the multipole method of Midgley and Davis (1962) becomes much more tractable.

In the case of a three-dimensional dipole, all the problems inherent in the first-order approximation can be overcome by higher-order approximations. According to

Beard (1964), however, the prime difficulty of the use of the iterative method lies in computing the surface correction field accurately with minimal machine time. There are two related difficulties. One is the singularity occurring in the integrand of the curvature field expression at $r' = 0$; and the other is the convergence of planes of equal longitude at the polar axis giving badly nonrectilinear areal segments in the numerical integration. These specific problems and other details of Mead's approach to the higher-order approximation are discussed in Section IV.

III. INTERNAL PRESSURES.

A. The Quiet-Day Ring Current.

(i) Plasma Energy Densities and Currents.

Plasmas having sufficient energy density to contribute significantly to the quiet-day ring current have been measured by Davis and Williamson (1963) on Explorer 12 and by Frank (1967b) on OGO-3. Figure 5 illustrates the equatorial distribution of the energy densities for these particles as deduced by Hoffman and Bracken (1965) and by Frank respectively. Hoffman and Bracken noted that, owing to a recalibration of the detectors, the Davis and Williamson fluxes and, therefore, their energy densities, should be increased by 25%. However, Davis and Williamson (1966) observed that the flux has a variation of 25% and that particles below 300 kev have decreased by 25% between 1961 and 1965. Therefore, the energy densities deduced by Hoffman and Bracken have been utilized as originally presented. Frank's data was taken at a geomagnetic latitude of $22^{\circ} \pm 2^{\circ}$. The sun-earth-satellite angle increased from 75° at $L = 5$ to about 110° at $L = 11$. The angle between the directional flux detector axis and the Jensen and Cain magnetic field lines decreased from 79° to 65° over the same interval. Figure 6 illustrates the observed proton spectra at $L = 6$.

The analysis of the ring currents produced by plasmas in the dipole field is simplified when the equatorial energy density is fit to the form $NE = (N_0 E) \exp(-(g_1(L-r_0))^2)$ where i equals 1 for $L \leq r_0$ and i equals 2 for $L \geq r_0$. (See Akasofu and Chapman, 1967 and references therein.) A flux distribution of the form $f(B, \phi) \propto \sin^\alpha \phi B^{-\alpha/2}$, where ϕ is the pitch angle, has proven to be both convenient and realistic in fitting particle distribution. Thus, in this model the five parameters, $N_0 E$, r_0 , α , g_1 , and g_2 , completely specify the ring current and its associated field.

Hoffman and Bracken determined that the values $N_0 E = 138 \text{ kev/cm}^3$, $r_0 = 3.5 R_E$, $\alpha = 2.5$, $g_1 = (1.0 R_E)^{-1}$, $g_2 = (1.25 R_E)^{-1}$ provided a best fit to the plasmas above 100 kev. They also found that in this energy range α decreased with decreasing energy and with increasing distance. Frank's data has been fit by the parameters $r_0 = 7 R_E$ and $g_1 = g_2 = (2 R_E)^{-1}$. The equatorial energy density may be obtained from that measured along the same field line at higher latitudes if the form of the pitch angle distribution is known. Detailed pitch angle information is not yet available, but it is likely that α lies between 0 and 2. For $\alpha = 0$, the energy density is constant along any field line, while for $\alpha = 2$, the equatorial

energy density is 3.4 times that at 22° latitude for a dipole field. It has been assumed somewhat arbitrarily that $N_0 E = 25 \text{ kev/cm}^3$ and $\alpha = 2$. Since this choice reflects the minimum equatorial energy ($\alpha = 0$) and limits the particle distribution to low latitudes ($\alpha = 2$), future data may enhance the total energy of the quiet-day ring current. Figure 5 also illustrates the values of these functions versus L.

In their detailed analysis of the Davis and Williamson proton currents, Hoffman and Bracken used an inaccurate current expression based on Akasofu and Chapman (1961). Kavanagh (1967) has shown that the azimuthal drift and diamagnetic currents in a dipole field are given by:

$$j_{\text{drift}}(r, \theta) = \frac{N(r, \theta) E}{BR_c} \frac{(\alpha + 4)}{(\alpha + 3)}$$

$$j_{\text{diamagnetism}} = \frac{(\alpha + 2)}{(\alpha + 3)} \left[\frac{E}{B} \right] \left\{ \frac{-2N(r, \theta)}{R_c} - \frac{r}{h_1} \frac{\partial N(r, \theta)}{\partial r} + \frac{2}{h_1 \tan \theta} \frac{\partial N(r, \theta)}{\partial \theta} \right\}$$

so that:

$$j = \left[\frac{E}{B} \right] \left\{ \frac{-\alpha}{(\alpha + 3)} \frac{N}{R_c} + \left(\frac{\alpha + 2}{\alpha + 3} \right) \left[\frac{-r}{h_1} \frac{\partial N}{\partial r} + \frac{2}{h_1 \tan \theta} \frac{\partial N}{\partial \theta} \right] \right\}$$

The radius of curvature R_c and the coordinate transformation h_1 are given by:

$$R_c = \left[\frac{r}{3 \sin \theta} \right] \left[\frac{(1 + 3 \cos^2 \theta)^{3/2}}{(1 + \cos^2 \theta)} \right] \approx LR_E/3$$

$$h_1 = \left[\frac{r(1 + 3 \cos^2 \theta)^{1/2}}{\sin \theta} \right] \approx LR_E$$

Kavanagh has also prepared a computer program which calculates the ring current field based on these equations. This calculation assumes that all particles are confined to the region bounded by the earth's surface and the dipole field line with $L = 10$. Kavanagh's program has been used in computing the following ring current field.

(ii) Properties of the Ring Current Field.

The fields due to these ring currents and their sums, hereafter designated as the total quiet-day ring current, are illustrated in Tables 1 - 6. The equatorial ring current fields are shown in Figure 7. The total of the pure dipole field and the ring current field in the equatorial plane is shown in Figure 8. It is interesting to note that this first-order calculation may be rather self-consistent in the sense that the gradient of the total field never changes sign.

The magnetic moment of these ring currents has been determined by calculating the ring current field at large distances ($50 - 130 R_E$). The magnetic moment of the higher energy ring current ($E \geq 97$ kev) is $.04 M_E$,

while that of the low energy ring current ($E \leq 50$ kev) is $.22 M_E$. This 26% increase in the earth's magnetic moment could have considerable effect on cosmic ray observations except for the nearness of the outer ring current belt to the magnetospheric boundary. The total energy of these distributions has been calculated by integrating

$$dE = (N_0 E) \exp \left[- (g_i (r \sin^{-2} \theta - r_0))^2 \right] \sin^{3\alpha} \theta (1 - 3 \cos^2 \theta)^{-\alpha/4} d\tau.$$

where $d\tau = R_E^3 r^2 dr \sin \theta d\theta d\phi$ in increments of $.5 R_E$ and 5° . The energy of the higher energy ($E \geq 97$ kev) portion of the ring current is 5.3×10^{21} ergs and that of the lower energy component ($E \leq 50$ kev) is 7.4×10^{21} ergs. To lowest order (Skopke, 1966) these energies produce fields of 14% and 19.5% respectively near the earth. These values are 3% to 5% less than the values obtained by integrating over the currents caused by the individual particles. It is expected that this difference would be reduced by using a more general relation than Skopke's in which the ring current field energy is not neglected.

(iii) Comparison with Observations.

This quiet-day ring current is consistent with both spacecraft and ground-based observations. Mead and Cahill (1967) compared magnetometer data from Explorer 12 with

the distorted field model of Mead (1964). They found that the measured distortions seemed to match quite well with the predictions of the Mead model with two exceptions. First, along the flanks of the magnetosphere there was a significant twisting of the field lines out of the magnetic meridians and somewhat less compression than predicted. The inclusion of a neutral-sheet tail field might explain this. Secondly, the effects of local quiet-time plasma were seen in the region from 3 to 6 R_E where the depression due to the quiet-day ring current was quite significant.

Of the seven passes considered, only two are within 30° of the subsolar point and have an average DST for the pass of less than 10 gamma. The data for one of these passes is illustrated in Figure 9. In this case, the deviation from Mead's model is about -40% at $L = 3.5$, zero between $L = 7$ and 9, and $+10\%$ at $L = 10$. The ring current field illustrated in Figure 3 agrees rather well with these observed deviations from Mead's model of the geomagnetic field. The 25% increase in the surface current field due to the effect of the quiet-day ring current, a 4 to 7% increase, will not significantly alter these differences between the predicted and observed fields.

The predicted external field at the earth's surface is in good agreement with surface observations (Cain, 1966).

The net external field at the earth's surface is the vector sum of the quiet-day ring current field and the magnetospheric surface-current field. The total quiet-day ring current field is about 41γ at the earth's surface and is directed southward. The magnetospheric surface currents are greater by 25% than the value determined by Mead (1964) to contain the addition to the earth's dipole moment. (See Tables 10 and 11.) However, if the subsolar distance is about $11 R_E$, the surface current field at the earth is about 26γ (Table 11) and directed northward. The sum of these fields is about 15γ and is directed southward. The neutral sheet field is directed southward and should increase this figure by about 5γ . Cain (1966) determined the existence of a statistically significant external field of 26.41γ based on an analysis of geomagnetic field data. The component of this field parallel to the dipole axis is 20.8γ and is directed southward. This result agrees quite well with the predicted net external field in both direction and in magnitude.

(iv) Analysis of Premises.

This analysis of the quiet-day ring current field is based upon two premises: the geomagnetic field may be described as being dipolar, and electric fields are

negligible. Although better models of the geomagnetic field are available, and the currents produced by plasmas drifting in a nondipolar magnetic field are known, the main effects of the distortion may be quantitatively analyzed as follows. The equatorial geomagnetic field may be expressed by $B_g = B_0 r^{-3} + B_1 + B_2 r \cos \phi$ where $B_0 = .31$ gauss, $B_1 = 25\%$ and $B_2 = 21\%$ (Mead, 1964). The symmetric term B_1 enhances the dipole field, thus decreasing the dipole field ring current by the ratio $B_{\text{dipole}} / (B_{\text{dipole}} + B_1)$. This amounts to a 4% decrease at $3.5 R_E$ and to a 22% decrease at $7 R_E$. This uniform field B_1 also increases the radius of curvature, further decreasing the current produced in comparison with the dipole field analysis. The noon-midnight asymmetry B_2 tends to cancel this on the night side, while enhancing the effect on the day side. However, no compensation for these effects has been made in light of the conservative evaluation of the equatorial energy density distribution of the outermost portion of the ring current field.

The effect of electric fields upon the low energy particles depends critically upon the electric field model, the shielding effect of the plasmopause, and the polarization field produced by the resultant motion of the particles in the electric and magnetic fields. Ignoring

the polarization field and the plasmapause and assuming the electric field is uniform with an intensity of 1 mv/meter directed across the magnetosphere from dawn to dusk, the gradient drift is balanced by the $\bar{E} \times \bar{B}$ drift at $7 R_E$ for particles with energy below 15 kev. Since at least half the energy density of the outer proton belt is carried by protons above 30 kev (Figure 6), the electric field may be considered as a perturbation, albeit a very large perturbation. In summary, it does not seem reasonable to evaluate the quiet-day ring current and its field in any greater detail (Hoffman and Bracken, 1967) until the ring-current energy-density distribution is known for various local times and the electric field configuration and magnitude are defined more adequately.

Table 1

Values of the theta-component of the magnetic field in gammas produced by a ring current band of charged particles described by the parameters: $N_0 E = 25 \text{ kev/cm}^2$, $R_0 = 7.0 R_E$, $g_1 = g_2 = (2R_E)^{-1}$, $\alpha = 2.0$. Negative values denote opposed in sense to geomagnetic field. By symmetry the theta component is zero at 90° latitude.

Geocentric distance, R_E	Latitude								
	80°	70°	60°	50°	40°	30°	20°	10°	0°
1.0	-3.7	-7.2	-10.5	-13.4	-15.9	-18.0	-19.4	-20.3	-20.6
1.4	-3.7	-7.3	-10.6	-13.5	-16.0	-18.0	-19.4	-20.2	-20.5
1.8	-3.7	-7.3	-10.7	-13.7	-16.1	-18.0	-19.3	-20.1	-20.3
2.2	-3.7	-7.3	-10.8	-13.9	-16.4	-18.2	-19.3	-19.9	-20.1
2.6	-3.6	-7.3	-10.9	-14.3	-16.8	-18.3	-19.3	-19.7	-19.9
3.0	-3.5	-7.1	-10.9	-14.8	-17.4	-18.5	-19.3	-19.5	-19.6
3.4	-3.2	-6.7	-10.5	-15.0	-18.0	-18.8	-19.5	-19.4	-19.4
3.8	-2.9	-6.1	-9.8	-14.5	-18.0	-19.4	-20.1	-19.4	-19.3
4.2	-2.6	-5.5	-8.9	-13.2	-17.5	-20.6	-21.3	-19.6	-19.5
4.6	-2.3	-4.8	-7.8	-11.5	-16.8	-22.3	-23.0	-20.3	-20.4
5.0	-2.0	-4.2	-6.9	-10.1	-16.1	-24.3	-25.0	-21.7	-22.1
5.4	-1.7	-3.6	-5.9	-9.1	-15.4	-25.4	-26.5	-23.9	-24.6
5.8	-1.4	-3.1	-5.1	-8.1	-14.0	-24.8	-26.9	-26.6	-27.5
6.2	-1.2	-2.5	-4.2	-6.8	-11.9	-21.8	-25.6	-29.2	-30.0
6.6	-1.0	-2.1	-3.5	-5.5	-9.3	-16.9	-22.8	-30.9	-31.2
7.0	-0.8	-1.7	-2.8	-4.3	-6.7	-11.1	-18.7	-30.7	-30.4
7.4	-0.6	-1.3	-2.1	-3.2	-4.4	-5.6	-14.1	-28.0	-27.2
7.8	-0.5	-1.0	-1.6	-2.2	-2.5	-1.6	-9.6	-22.8	-21.9
8.2	-0.4	-0.8	-1.2	-1.5	-1.2	0.6	-5.6	-15.7	-15.2
8.6	-0.3	-0.6	-0.8	-0.9	-0.3	1.5	-2.3	-8.0	-8.2
9.0	-0.2	-0.4	-0.5	-0.4	0.3	1.8	0.4	-0.7	-1.9
9.4	-0.1	-0.3	-0.3	-0.1	0.7	2.0	2.4	4.8	2.9
9.8	-0.1	-0.1	-0.1	0.2	0.9	2.2	3.7	8.0	6.1
10.2	0.0	-0.1	0.1	0.4	1.1	2.3	4.4	9.0	7.6
10.6	0.0	0.0	0.2	0.5	1.2	2.4	4.6	8.7	8.0
11.0	0.0	0.1	0.2	0.6	1.3	2.4	4.5	7.9	7.7
11.4	0.0	0.1	0.3	0.7	1.3	2.4	4.3	7.0	7.1
11.8	0.1	0.2	0.4	0.7	1.3	2.3	4.0	6.2	6.4
12.2	0.1	0.2	0.4	0.7	1.3	2.2	3.7	5.4	5.8
12.6	0.1	0.2	0.4	0.7	1.3	2.1	3.4	4.8	5.2
13.0	0.1	0.2	0.4	0.7	1.2	2.0	3.1	4.3	4.6

Table 2

Values of the radial-component of the magnetic field in gammas produced by a ring current band of charged particles described by the parameters: $N_0 E = 25 \text{ kev/cm}^2$, $R_0 = 7.0 R_E$, $g_1 = g_2 = (2 R_E)^{-1}$, $\alpha = 2.0$. Negative values denote opposed in sense to geomagnetic field. By symmetry the radial component is zero at 0° latitude.

Geocentric distance, R_E	Latitude								
	90°	80°	70°	60°	50°	40°	30°	20°	10°
1.0	23.3	20.6	19.6	18.0	15.9	13.3	10.3	7.0	3.5
1.4	22.8	20.7	19.7	18.0	15.9	13.2	10.2	6.9	3.5
1.8	22.5	20.8	19.9	18.1	15.9	13.2	10.1	6.8	3.4
2.2	22.3	20.9	20.0	18.3	15.9	13.1	9.9	6.6	3.3
2.6	22.1	20.9	20.1	18.6	16.1	13.1	9.6	6.4	3.1
3.0	21.7	20.8	20.2	19.0	16.6	12.9	9.3	6.1	2.9
3.4	21.2	20.4	20.1	19.4	17.6	12.5	8.9	5.8	2.6
3.8	20.5	19.9	19.9	19.7	18.7	12.3	8.7	5.5	2.2
4.2	19.7	19.2	19.4	19.7	19.5	12.8	8.9	4.9	1.6
4.6	18.7	18.4	18.7	19.3	19.6	14.2	9.8	4.1	1.0
5.0	17.7	17.5	17.9	18.7	19.3	16.4	11.6	2.9	0.4
5.4	16.7	16.5	17.0	17.9	18.9	18.5	14.0	1.8	0.1
5.8	15.7	15.5	16.1	17.1	18.6	20.2	16.7	1.2	0.4
6.2	14.7	14.5	15.2	16.3	18.1	21.2	19.2	1.6	1.3
6.6	13.7	13.6	14.2	15.4	17.4	21.4	20.8	3.3	2.9
7.0	12.7	12.6	13.2	14.4	16.5	20.7	21.3	6.1	4.9
7.4	11.8	11.7	12.3	13.4	15.5	19.4	20.6	9.5	6.9
7.8	11.0	10.9	11.4	12.5	14.3	17.7	19.0	12.7	8.5
8.2	10.2	10.1	10.6	11.5	13.2	15.9	17.1	14.9	9.6
8.6	9.4	9.4	9.8	10.6	12.0	14.2	15.3	15.8	10.0
9.0	8.7	8.7	9.1	9.8	11.0	12.7	13.7	15.5	9.6
9.4	8.1	8.0	8.4	9.0	10.0	11.3	12.3	14.4	8.8
9.8	7.5	7.4	7.7	8.3	9.1	10.1	11.0	12.7	7.7
10.2	7.0	6.9	7.1	7.6	8.3	9.1	9.8	11.0	6.5
10.6	6.5	6.4	6.6	7.0	7.5	8.2	8.7	9.4	5.5
11.0	6.0	5.9	6.1	6.4	6.9	7.4	7.8	8.0	4.7
11.4	5.6	5.5	5.7	5.9	6.3	6.7	6.9	6.8	4.0
11.8	5.2	5.1	5.2	5.5	5.8	6.0	6.2	5.8	3.4
12.2	4.8	4.8	4.9	5.1	5.3	5.5	5.5	5.0	2.9
12.6	4.5	4.4	4.5	4.7	4.8	5.0	4.9	4.4	2.5
13.0	4.2	4.1	4.2	4.3	4.4	4.5	4.4	3.8	2.2

Table 3

Values of the theta-component of the magnetic field in gammas produced by a ring current band of charged particles described by the parameters: $N_0 E = 138 \text{ kev/cm}^3$, $R_0 = 3.5 R_E$, $g_1 = (1 R_E)^{-1}$, $g_2 = (1.2 R_E)^{-1}$, $\alpha = 2.5$. Negative values denote opposed in sense to geomagnetic field. By symmetry the theta component is zero at 90° latitude.

Geocentric distance, R_E	Latitude								
	80°	70°	60°	50°	40°	30°	20°	10°	0°
1.0	-3.6	-7.2	-10.5	-13.6	-16.1	-18.1	-19.5	-20.3	-20.6
1.4	-3.5	-7.0	-10.5	-13.8	-16.5	-18.3	-19.5	-20.1	-20.3
1.8	-3.1	-6.4	-9.9	-13.9	-17.0	-18.9	-19.9	-19.9	-20.0
2.2	-2.6	-5.5	-8.7	-12.7	-16.9	-20.4	-21.4	-20.3	-20.4
2.6	-2.1	-4.4	-7.2	-10.7	-15.9	-22.5	-23.9	-22.3	-22.9
3.0	-1.6	-3.4	-5.6	-8.6	-13.8	-22.0	-25.0	-26.2	-26.9
3.4	-1.2	-2.5	-4.1	-6.4	-10.5	-17.6	-22.8	-26.8	-29.3
3.8	-0.8	-1.8	-2.9	-4.4	-6.8	-10.9	-17.5	-27.0	-27.1
4.2	-0.6	-1.2	-1.9	-2.7	-3.7	-5.0	-11.0	-20.2	-20.1
4.6	-0.4	-0.8	-1.1	-1.5	-1.6	-1.3	-5.0	-10.6	-10.9
5.0	-0.2	-0.4	-0.6	-0.7	-0.3	0.6	-0.6	-1.9	-2.6
5.4	-0.1	-0.2	-0.2	-0.1	0.4	1.5	2.1	3.8	2.9
5.8	0.0	-0.1	0.0	0.2	0.8	1.9	3.4	6.2	5.6
6.2	0.0	0.1	0.2	0.5	1.0	2.0	3.7	6.5	6.2
6.6	0.0	0.1	0.3	0.6	1.1	2.0	3.6	5.8	5.8
7.0	0.1	0.2	0.3	0.6	1.1	1.9	3.2	4.9	5.1
7.4	0.1	0.2	0.4	0.6	1.1	1.8	2.9	4.0	4.3
7.8	0.1	0.2	0.4	0.6	1.0	1.6	2.5	3.3	3.6
8.2	0.1	0.2	0.4	0.6	1.0	1.5	2.2	2.8	3.0
8.6	0.1	0.2	0.4	0.6	0.9	1.3	1.9	2.4	2.5
9.0	0.1	0.2	0.4	0.6	0.8	1.2	1.6	2.0	2.1
9.4	0.1	0.2	0.3	0.5	0.8	1.1	1.4	1.7	1.8
9.8	0.1	0.2	0.3	0.5	0.7	1.0	1.3	1.5	1.6
10.2	0.1	0.2	0.3	0.5	0.6	0.8	1.1	1.3	1.4
10.6	0.1	0.2	0.3	0.4	0.6	0.8	1.0	1.2	1.2
11.0	0.1	0.2	0.3	0.4	0.5	0.7	0.9	1.0	1.1
11.4	0.1	0.2	0.2	0.4	0.5	0.6	0.8	0.9	0.9
11.8	0.1	0.1	0.2	0.3	0.5	0.6	0.7	0.8	0.8
12.2	0.1	0.1	0.2	0.3	0.4	0.5	0.6	0.7	0.6
12.6	0.1	0.1	0.2	0.3	0.4	0.5	0.6	0.7	0.7
13.0	0.1	0.1	0.2	0.3	0.4	0.4	0.5	0.6	0.6

Table 4

Values of the radial-component of the magnetic field in gammas produced by a ring current band of charged particles described by the parameters: $N_0 E = 138 \text{ kev/cm}^3$, $R_0 = 3.5 R_E$, $g_1 = (1 R_E)^{-1}$, $g_2 = (1.2 R_E)^{-1}$, $\alpha = 2.5$. Negative values denote opposed in sense to geomagnetic field. By symmetry the radial component is zero at 0° latitude.

Geocentric distance, R_E	Latitude								
	90°	80°	70°	60°	50°	40°	30°	20°	10°
1.0	22.2	20.6	19.7	18.1	16.0	13.3	10.2	6.9	3.5
1.4	21.6	20.4	19.7	18.4	16.3	13.3	10.0	6.7	3.3
1.8	20.6	19.8	19.5	18.8	17.2	13.3	9.7	6.2	2.9
2.2	19.3	18.7	18.8	18.8	18.2	14.1	10.2	5.4	2.1
2.6	17.6	17.3	17.6	18.1	18.5	16.3	12.3	4.2	1.4
3.0	15.9	15.6	16.1	17.0	18.1	18.6	15.6	3.8	1.8
3.4	14.1	13.9	14.5	15.5	17.2	19.7	18.4	5.7	3.7
3.8	12.4	12.3	12.9	13.9	15.7	18.9	19.3	9.4	6.4
4.2	10.9	10.8	11.3	12.3	14.0	16.9	18.1	13.0	8.5
4.6	9.5	9.5	9.9	10.7	12.1	14.5	15.9	14.7	9.4
5.0	8.3	8.3	8.6	9.3	10.4	12.1	13.4	14.3	8.9
5.4	7.3	7.2	7.5	8.0	8.9	10.0	11.1	12.4	7.6
5.8	6.4	6.3	6.5	7.0	7.6	8.4	9.1	10.0	6.1
6.2	5.6	5.5	5.7	6.0	6.5	7.0	7.5	7.8	4.7
6.6	4.9	4.9	5.0	5.2	5.5	5.9	6.1	6.0	3.6
7.0	4.4	4.3	4.4	4.5	4.8	4.9	5.0	4.7	2.8
7.4	3.9	3.8	3.9	4.0	4.1	4.2	4.2	3.7	2.2
7.8	3.4	3.4	3.4	3.5	3.6	3.6	3.5	3.0	1.7
8.2	3.1	3.0	3.0	3.1	3.1	3.1	2.9	2.4	1.4
8.6	2.7	2.7	2.7	2.7	2.7	2.7	2.5	2.0	1.1
9.0	2.4	2.4	2.4	2.4	2.4	2.3	2.1	1.7	0.9
9.4	2.2	2.1	2.1	2.1	2.1	2.0	1.8	1.4	0.8
9.8	2.0	1.9	1.9	1.9	1.9	1.8	1.6	1.2	0.7
10.2	1.8	1.7	1.7	1.7	1.7	1.6	1.4	1.1	0.6
10.6	1.6	1.6	1.6	1.5	1.5	1.4	1.2	0.9	0.5
11.0	1.5	1.4	1.4	1.4	1.3	1.2	1.1	0.8	0.4
11.4	1.4	1.3	1.3	1.3	1.2	1.1	1.0	0.7	0.4
11.8	1.2	1.2	1.2	1.1	1.1	1.0	0.8	0.6	0.3
12.2	1.1	1.1	1.1	1.0	1.0	0.9	0.8	0.6	0.3
12.6	1.0	1.0	1.0	1.0	0.9	0.8	0.7	0.5	0.3
13.0	1.0	0.9	0.9	0.9	0.8	0.7	0.6	0.5	0.2

Table 5

Values of the theta-component of the magnetic field in gammas produced by the quiet-day ring current. These values represent the sum of the ring currents specified in the preceding tables. Negative values denote opposed in sense to geomagnetic field. By symmetry the theta component is zero at 90° latitude.

Geocentric distance, R_E	Latitude								
	80°	70°	60°	50°	40°	30°	20°	10°	0°
1.0	-7.3	-14.4	-21.0	-27.0	-32.0	-36.0	-38.9	-40.6	-41.1
1.4	-7.2	-14.3	-21.1	-27.4	-32.5	-36.3	-38.9	-40.3	-40.8
1.8	-6.8	-13.7	-20.6	-27.5	-33.2	-36.9	-39.2	-40.0	-40.3
2.2	-6.3	-12.8	-19.5	-26.6	-33.3	-38.6	-40.7	-40.2	-40.6
2.6	-5.7	-11.7	-18.1	-25.0	-32.7	-40.8	-43.1	-42.1	-42.8
3.0	-5.1	-10.5	-16.5	-23.4	-31.2	-40.5	-44.2	-45.7	-46.5
3.4	-4.4	-9.2	-14.7	-21.5	-28.4	-36.4	-42.2	-48.2	-48.7
3.8	-3.8	-7.9	-12.7	-19.0	-24.8	-30.4	-37.6	-46.4	-46.3
4.2	-3.2	-6.7	-10.7	-15.9	-21.3	-25.6	-32.3	-39.8	-39.6
4.6	-2.7	-5.6	-9.0	-13.0	-18.4	-23.6	-28.1	-31.0	-31.3
5.0	-2.2	-4.6	-7.5	-10.8	-16.5	-23.6	-25.6	-23.6	-24.7
5.4	-1.8	-3.8	-6.2	-9.2	-15.0	-23.9	-24.4	-20.1	-21.6
5.8	-1.5	-3.1	-5.1	-7.8	-13.2	-22.9	-23.5	-20.4	-21.9
6.2	-1.2	-2.5	-4.1	-6.4	-10.8	-19.8	-21.9	-22.7	-23.7
6.6	-1.0	-2.0	-3.2	-5.0	-8.2	-14.9	-19.2	-25.1	-25.4
7.0	-0.7	-1.5	-2.4	-3.6	-5.6	-9.2	-15.5	-25.8	-25.3
7.4	-0.6	-1.1	-1.8	-2.5	-3.3	-3.8	-11.5	-24.0	-22.9
7.8	-0.4	-0.8	-1.2	-1.6	-1.5	0.1	-7.1	-19.5	-18.3
8.2	-0.3	-0.6	-0.8	-0.9	-0.2	2.1	-3.4	-13.0	-12.2
8.6	-0.2	-0.4	-0.5	-0.3	0.6	2.8	-0.4	-5.6	-5.7
9.0	-0.1	-0.2	-0.2	0.1	1.1	3.0	2.0	1.3	0.2
9.4	-0.1	-0.1	0.1	0.4	1.4	3.1	3.8	6.5	4.8
9.8	0.0	0.1	0.2	0.7	1.6	3.1	4.9	9.5	7.6
10.2	0.0	0.1	0.4	0.8	1.7	3.2	5.5	10.3	9.0
10.6	0.1	0.2	0.4	0.9	1.8	3.2	5.6	9.9	9.2
11.0	0.1	0.2	0.5	1.0	1.8	3.1	5.4	8.9	8.8
11.4	0.1	0.3	0.5	1.0	1.8	3.0	5.1	7.9	8.1
11.8	0.1	0.3	0.6	1.0	1.8	2.9	4.7	7.0	7.3
12.2	0.1	0.3	0.6	1.0	1.7	2.8	4.4	6.1	6.5
12.6	0.2	0.3	0.6	1.0	1.7	2.6	4.0	5.4	5.8
13.0	0.2	0.3	0.6	1.0	1.6	2.5	3.7	4.9	5.2

Table 6

Values of the radial-component of the magnetic field in gammas produced by the quiet-day ring current. These values represent the sum of the ring currents specified in the preceding tables. Negative values denote opposed in sense to geomagnetic field. By symmetry the radial component is zero at 0° latitude.

Geocentric distance, R _E	Latitude								
	90°	80°	70°	60°	50°	40°	30°	20°	10°
1.0	45.5	41.2	39.3	36.1	31.8	26.6	20.5	13.9	7.0
1.4	44.3	41.1	39.4	36.4	32.1	26.5	20.2	13.6	6.8
1.8	43.1	40.7	39.4	36.9	33.0	26.4	19.8	13.0	6.3
2.2	41.6	39.7	38.8	37.1	34.1	27.2	20.1	12.0	5.4
2.6	39.7	38.2	37.7	36.7	34.6	29.3	21.9	10.5	4.6
3.0	37.6	36.4	36.3	36.0	34.7	31.5	24.9	9.9	4.7
3.4	35.3	34.4	34.6	35.0	34.8	32.2	27.3	11.5	6.3
3.8	32.9	32.2	32.8	33.6	34.4	31.2	28.0	14.9	8.5
4.2	30.6	30.0	30.7	32.0	33.5	29.7	27.0	17.9	10.1
4.6	28.3	27.8	28.6	30.0	31.8	28.7	25.7	18.8	10.3
5.0	26.1	25.7	26.5	28.0	29.7	28.4	24.9	17.2	9.3
5.4	24.0	23.7	24.5	26.0	27.7	28.6	25.1	14.2	7.7
5.8	22.1	21.8	22.6	24.1	26.1	28.5	25.8	11.2	6.4
6.2	20.3	20.1	20.9	22.3	24.6	28.2	26.6	9.4	6.0
6.6	18.6	18.4	19.2	20.6	23.0	27.2	26.9	9.3	6.5
7.0	17.1	16.9	17.6	19.0	21.3	25.6	26.3	10.8	7.6
7.4	15.7	15.5	16.2	17.4	19.6	23.6	24.8	13.2	9.0
7.8	14.4	14.2	14.8	16.0	17.9	21.3	22.5	15.6	10.3
8.2	13.2	13.1	13.6	14.6	16.3	19.0	20.0	17.3	11.0
8.6	12.2	12.0	12.5	13.3	14.7	16.9	17.8	17.8	11.1
9.0	11.2	11.0	11.4	12.2	13.4	15.0	15.8	17.2	10.6
9.4	10.3	10.2	10.5	11.1	12.1	13.3	14.1	15.8	9.6
9.8	9.5	9.4	9.7	10.2	11.0	11.9	12.6	13.9	8.4
10.2	8.8	8.6	8.9	9.3	10.0	10.7	11.2	12.0	7.1
10.6	8.1	8.0	8.2	8.5	9.0	9.6	10.0	10.3	6.0
11.0	7.5	7.4	7.5	7.8	8.2	8.6	8.8	8.8	5.1
11.4	6.9	6.8	7.0	7.2	7.5	7.8	7.9	7.5	4.4
11.8	6.4	6.3	6.4	6.6	6.8	7.0	7.0	6.4	3.8
12.2	6.0	5.8	5.9	6.1	6.3	6.4	6.3	5.6	3.2
12.6	5.5	5.4	5.5	5.6	5.7	5.8	5.6	4.9	2.8
13.0	5.2	5.0	5.1	5.2	5.3	5.3	5.0	4.3	2.5

B. The Neutral-Sheet Tail Field.

The currents which produce the geomagnetic tail flow across the neutral sheet and close on the surface of the magnetosphere. The most realistic model to simulate these currents would be that of two semi-infinite solenoids arranged to form a figure 8. A model which avoids the mathematical complexity of the cylindrical solenoids, yet includes at least a portion of the return current on the magnetopause, is shown in Figure 10. This semi-infinite, quadra-sheet model has two pair of current sheets placed back to back with a space R_t between the current sheets in each pair. The radius of the geomagnetic tail R_t is about $20 R_E$. A uniform current per unit length J_0 is completed through each pair of sheets which lie in planes of constant y with $x \leq 0$. It can be shown by combining the fields of the individual current sheets in a symmetric manner that the quadra-sheet field is given by:

$$B_y = -(\mu_0 J_0 / 2\pi) \ln \left\{ \frac{[\overline{x^2 + (y-R_t)^2}] [\overline{x^2 + (y+R_t)^2}]}{[x^2 + y^2]^2} \right\}^{\frac{1}{2}}$$

$$B_x = -(\mu_0 J_0 / 2\pi) \left\{ \text{atan} \left[-x / (y-R_t) \right] + \text{atan} \left[-x / (y+R_t) \right] \right. \\ \left. - 2 \text{atan}(-x/y) + (\pi/2) \left[S(y-R_t) + S(y+R_t) - 2S(y) \right] \right\}$$

where the center sheets are in the $y = 0$ plane, where

the edge of each of the sheets is located at $x = 0$, and where $S(A)$ signifies the sign of A in units of plus or minus one. As expected, the tail field near the center sheets reduces to $B_{\text{tail}} = \mu_0 J_0$ which is the relationship between a current sheet $2J_0$ and the uniform field $B = (\mu_0/2\pi)(2J_0)\pi$ on either side.

This quadra-sheet model is much more realistic than previous models of the tail field. The simplest model of the tail field was the field produced by an infinite current sheet (Taylor and Hones, 1965). A truncated current-sheet model, shown in Figure 11, has been utilized by Williams and Mead (1965). In this geometry $B_y = (\mu_0 J_0 / 2\pi) \ln(r_2/r_1)$ and $B_x = -(\mu_0 J_0 / 2\pi)\alpha$ where J_0 is the current per unit width, r_1 and r_2 are the distances to the inner and outer edges of the current sheet, and α is the angle between r_1 and r_2 . When applied to the geomagnetic field, this model is specified by three parameters: the distance to the inner edge of the current sheet; the width of the current sheet; and the tail current J_0 , or the tail field near the current sheet. Although more realistic than the infinite current-sheet model, both configurations required that the current return at infinity.

The most obvious difference between the quadra-sheet model and the single-sheet model of Williams and Mead is that the spacing between the sheets (the radius of the geomagnetic tail R_t) determines the tail field instead of the width of the truncated current sheet (the length of the geomagnetic tail L_t). The truncated current-sheet model gives the length of the geomagnetic tail an unrealistic influence on the tail field near the inner edge. To compare the two models, consider the tail field in the equatorial plane $y = 0$. For the quadra-sheet model $B_y(y = 0) = -(B_{tail}/2\pi) \ln \left[(x^2 + R_t^2)/x^2 \right]$. In the limit of $x^2 \ll R_t^2$, this normal field approaches $-(B_{tail}/\pi) \ln(R_t/|x|)$. In the truncated current-sheet model, $B_y(y = 0) = -(B_{tail}/2\pi) \ln(L_t/|x|)$ if $|x| < L_t$. The two fields are equal if L_t equals $R_t^2/|x|$ for $|x| < R_t$. This difference becomes significant for $|x| \geq 10 R_E$ since $R_t \approx 20 R_E$ and tail lengths as high as $200 R_E$ have been utilized (Roederer, 1967).

The difference between the models is even greater at the subsolar point of the magnetosphere. Here the field produced by the tail currents is $\sim 0.11 B_{tail}$ for the quadra-sheet model, assuming that $x = R_t = 20 R_E$. If the tail field is less than 30% , the subsolar field which opposes the geomagnetic field is less than 3% and is

negligible in comparison with the quiet-day ring current field. In the Williams-Mead model, the tail field at the subsolar point is $-0.73 B_{\text{tail}}$, assuming $L_t = 200 R_E$. Under the same conditions, the subsolar tail field would be 22% and would completely cancel the quiet-day ring current field.

IV. COMPUTATIONAL DETAILS

The programs utilized in this analysis are based upon those formulated by Mead (1964). Copies of the original programs, along with personal instruction in their use, have been generously given by Dr. Mead. Although substantial changes have been made within the decision-making sections of the program, the basic format has been retained. The entire process is best described in three distinct, sequential stages. Stage I involves the calculation of a self-consistent boundary surface. Stage II fits the surface current field to a series of spherical harmonic coefficients. In Stage III the configuration of the field lines is determined.

The specific programs utilized in each stage and a brief description of each are presented in the order in which they are utilized.

Stage I. Calculation of a Self-Consistent Boundary Surface.

Call SINCOS: This sets up a matrix of sine and cosine values for angles at 5° intervals. The curvature fields are set equal to zero for the first surface.

Call SUR:

SUR: Specifies the angles theta and phi; then calls MAZE to solve for the equilibrium radius.

MAZE: Manipulates the radius until the surface is in equilibrium at this point.

ZEROC: Determines the pressure difference at each point which MAZE considers.

RINGC1: Gives the ring current field at any point.

NORMAL: Determines the surface derivatives using a six-point fit after SUR has completely solved for a new solution.

* (Optional operations may be called here.)

Call FLD:

FLD: First specifies the surface locations (R, θ, ϕ) where the curvature field will be computed; then calls FLD1.

FLD1: Sums the contribution of each element of surface area as given by FIELD.

FIELD: Computes the field due to surface currents at a given element of area as observed at the point specified by FLD. The evaluation of the surface current requires a knowledge of the ring current field.

CONTRL: Maximizes the accuracy and minimizes the time involved in summing by varying the size of the current carrying area considered at a given time.

FLD: Then interpolates to find the values of the curvature field at each point on the surface.

* (Optional operations may be called here.)

This operation (call SUR, call FLD) is continued using the new curvature fields until a self-consistent solution is achieved.

The asterisks designate points at which optional operations may be called. These include: WRITE TAPE, Call PRINT, Call BZERO, and Call CURENT. PRINT prints out values of the surface, the surface derivatives, the curvature fields, and the surface currents by calling PR. BZERO evaluates the magnitude and direction of the total field to see how tangential it is to the surface. CURENT evaluates the magnitude and direction of the surface currents.

Stage II. Calculation of Surface Current Field.

Once a surface is determined to be self-consistent, the surface current field is fit by a spherical expansion. First INPUT calls upon FLD1B, FIELD, and RINGC1 to calculate the surface current field at selected points within the magnetosphere. These vector fields are serialized and transformed to a dipole coordinate system. DANLSB

determines the expansion coefficients which would give the best fit to the surface current field.

Stage III. Determination of Field Lines.

- DDIP: Tracks the coordinates of the field line beginning at any predetermined point.
- MAGNET: Generates the surface current field, utilizing the coefficients calculated by DANLSB.
- RINGC: Generates the ring current field in dipole coordinates.
- UMPLOT: The University of Michigan plotting routine which plots the path of each field line.

A. Detailed Explanation of Computer Programs.

The following section gives a detailed explanation of each of the above subroutines.

Stage I. Calculation of a Self-Consistent Boundary Surface.

SUR determines how many elements the surface will be divided into. The two-dimensional dipole was handled in 1° intervals. The three-dimensional dipole was handled in elements 5° square. The coordinate system is defined with the Z axis point toward the sun and the Y axis

parallel to the geomagnetic axis as shown in Figure 1 of Mead and Beard (1964). SUR then calls out the respective θ, ϕ coordinates and makes a rough guess at a radial distance in the vicinity of the solution. This guess is based on the radius of the neighboring points and the local derivatives of the surface. For example, one trial radius is given by $R(\phi, \theta) = R(\phi - 5^\circ, \theta) + \left[\partial R(\phi - 5^\circ, \theta) / \partial \phi \right] \times H5D$ where H5D is 5° in radians. A second trial point is given by $R(\theta, \phi) = R(\phi, \theta - 5^\circ) + \left[\partial R(\phi, \theta - 5^\circ) / \partial \theta \right] \times H5D$. The smaller of these two quantities was used as the starting point for MAZE. Normally, this choice is less than, yet within five per cent of, the equilibrium radius.

MAZE is the decision-making section of the operation and not coincidentally the largest subroutine consisting of 734 Fortran cards. MAZE identifies the equilibrium radius X_0 by a three-stage process. First MAZE increases the test radius by units of $.001(X_1^3)$ until either the external solar wind pressure becomes greater than the internal magnetic pressure, or the solar wind pressure begins decreasing. This search procedure usually locates the equilibrium radius within .1%. Secondly, MAZE proceeds in steps of $.0001(X_1^3)$ until the pressure difference changes sign. The equilibrium point is now bracketed within about .01%. The third phase consists in identifying

the equilibrium point within one part in 10^7 . This is done by using a second-order calculation on the two points which bracket the equilibrium point to determine the expected crossing point. This radius replaces the radius on the same side of the equilibrium point. A combination of first and second-order calculations is executed. The equilibrium point remains bracketed until the difference between the points is less than $10^{-7}X_1$. Seventy to ninety per cent of the points on the surface are handled in this manner without any problems. Such a case is illustrated in Figure 12. The difference in the internal and external pressures for a radius X is determined by ZEROC and denoted by $Y(X)$.

During the approach to a self-consistent solution, there is no guarantee that there is an equilibrium radius at each point on the surface as shown in Figure 12. Such contingencies were handled by a modified version of Mead's version of the MAZE subroutine which was entitled MAZEMD. The alternate criteria for success, utilized by Mead, was to find a local minimum in the pressure difference if a crossing point does not exist.

ZEROC computes the pressure difference at any point on the surface. This subroutine first calculates the surface derivatives based on previously calculated

adjacent points. From this the angle between the surface normal and the solar wind velocity vector is determined. Secondly, ZEROC calculates the solar wind body pressure. There are several versions of this program with different solar wind normalizations to balance the internal ring currents at $r_0 = 10 R_E$, and with different body pressure distributions depending on the model of the solar wind. Third, ZEROC calculates the internal magnetic pressure. The sum of the dipole field, the ring current field as given by RINGC1, and the curvature field is computed. The internal pressure, given by $(2B_{\text{total}})^2$ or $(2\hat{n} \times \bar{B}_{\text{total}})^2$ depending upon the model, is then calculated. Finally, the difference in the pressures given by ZEROC(X1) is calculated and transmitted to MAZE.

RINGC1 calculates the components of the assumed ring current field at any given point. Altogether, three versions of the subroutine were utilized. The first assumed the ring current field was absent and thus output zeros. The second version, utilized in the line dipole problem, calculated the field for two parallel wire currents. The third version utilized the total quiet-day ring current calculated in Section III-A. RINGC1 interpolated between points where the ring current was calculated accurately as given in Tables 5

and 6. Beyond $13 R_E$ RINGC1 assumed the ring-current field fell off as R^{-3} .

NORMAL recalculates all the surface derivatives using a five-point fit to determine the derivative at the center point. The formula was taken from Morgenau and Murphy (1956), page 456, equation 13.9. For a smooth surface the difference between the three-point derivative calculated by ZEROC and this five-point derivative is negligible. However, should a bump appear in the surface as the surface approaches equilibrium, a three-point derivative evaluated at the end point could present a false picture of the surface and mathematically affect the ability of the surface to seek out an equilibrium configuration. Such an event occurred rarely, however, so that NORMAL merely served as a check on how smooth the surface really was.

FLD first calls out the points where the curvature field is to be computed. The integration over an entire surface to obtain the field at a single point takes about one minute on an IBM 7040. Following MEAD the curvature field was calculated at the subsolar point and at 10° intervals in θ beyond $\theta = 40^\circ$ and at 15° intervals in ϕ . The curvature fields were transformed to an X,Y,Z coordinate system; and a four-point interpolation

procedure utilizing all the symmetries inherent in the problem was applied. The final field was output in X,Y,Z coordinates, then transformed to R, θ , ϕ coordinates, and then output.

FLD1 calculates the curvature field at a point R(ϕ_0, θ_0) by summing the field due to a surface current at R(ϕ, θ). First, FLD calls CONTRL which decides how to group the surface elements to increase accuracy and decrease the time involved. FLD then calls out the ϕ, θ current-source locations; calculates the total field at this point, as well as the spherical angles between the radius vector to the current element; and the radius vector to the observation element. FLD calls FIELD to determine the quantity, $\bar{J} \times \hat{r}'/r'^2$, based on this set of conditions. FLD, utilizing the symmetry of the problem, rotates the source point by 180° in ϕ , reflects across the meridian, and finally rotates again by 180° , thus determining the contribution of four symmetrically located elements. The area of each point is also calculated so that the elements $((\bar{J} \times \hat{r}')/r'^2) dS$ may be summed. FLD1 ignores the contribution from the closest area element to the observation point. After integrating over the entire surface in blocks of 5° square or larger, CONTRL now commands FLD to recalculate the contribution of the

closest elements to the observation point. FLD first subtracts the contributions of the adjacent elements, as computed on a 5° square basis, then recalculates their contribution on a 1° square basis. This operation is most important when contributions of adjacent elements do not cancel because of a rapid change in the quantity $\bar{J} \times \hat{r}'/r'^2$. Such changes are most evident near the neutral point where the current changes direction and the surface changes shape rapidly.

CONTRL decides how the surface will be divided up for summing the contributions to the curvature field. To increase speed distant elements, especially those in the tail where \bar{J} is small, are grouped together and summed as a unit. To improve accuracy, elements adjacent to the observation point are subdivided into 1° areas.

FIELD calculates the vector quantity $\bar{J} \times \hat{r}'/r'^2$ as measured in the coordinate system of the observer. \bar{J} is given by $\hat{n} \times \bar{B}_{total}$ in the local coordinate system ϕ', θ' . \bar{J} is then transformed to the observer coordinate system ϕ_0, θ_0 and crossed with $\hat{r}' = \bar{r}' - \bar{r}_0 / |\bar{r}' - \bar{r}_0|$, then divided by $|\hat{r}'|^2$. The vector components of $\bar{J} \times \hat{r}'/r'^2$ are then transmitted to FLD1 for summing.

BZERO evaluates the relation of the total field and the surface normal at each point on the surface. First,

the ratio $|\hat{n} \times \bar{B}| / |\bar{B}|$ is calculated and then printed. This provides a measure of how well the iterative method is proceeding. Secondly, the ratio of the surface-current field to the theoretical surface-current field necessary to make the total field tangential to the surface is calculated. Since only the ratio of the absolute values was output, this quantity was of limited value. Finally, the magnitude of the total field was calculated. This indicates to what extent the neutral point is a point of zero field.

CURRENT calculates the components of $\bar{J} = \bar{B} \times \hat{n}_s$ at each point on the surface and calls PRINT to output their values.

INPUT calls out selected points inside the magnetopause; takes the value of the surface-current field at this point as calculated by FLD1B, FIELD, AND RINGC1; serializes this data; then transforms this vector field into the dipole coordinate system. The surface field \bar{B}_{sur} at points on the inside of the magnetopause is given by $\bar{B}_{sur} = \bar{B}_{total} - (\bar{B}_{internal})$. The internal field $\bar{B}_{internal}$ is the sum of the dipole field and the ring-current field. The total field \bar{B}_{total} is given by $2(\bar{B}_{internal} + \bar{B}_{curvature})$. (See Section II, Equation 10.) Actually \bar{B}_{sur} was defined by $\bar{B}_{sur} = \bar{B}_{total}^{tangential} - \bar{B}_{internal}$

where $\bar{B}_{\text{total}}^{\text{tangential}} = \bar{B}_{\text{total}} - \hat{n}(\hat{n} \cdot \bar{B}_{\text{total}})$. Since the fields due to surface currents are largest at the magnetopause, the inclusion of points on the surface is essential to achieve an accurate description of the field. In the three-dimensional problem, 746 points were fitted. 360 were on the magnetopause, 380 were distributed on concentric spheres of 1, 3, 5, 7, and 9 R_E , while the remaining were at 12, 15, 20, 25, 30, and 35 R_E in the antisolar direction. Figure 13 illustrates the fitting points in the equatorial plane and any other plane inclined at multiples of 15° to the equatorial plane yet passing through the subsolar axis.

DANLSB utilizes the fact that in a region where $\nabla \times \bar{B} = 0$, $\bar{B} = \nabla \bar{\Phi}$, and since $\nabla \cdot \bar{B} = 0$, this means $\bar{\Phi}$ satisfies Laplace's equation $\nabla^2 \bar{\Phi} = 0$. In polar coordinates $\bar{\Phi}$ is given by:

$$a \sum_{n=1}^{\infty} \sum_{m=0}^n (g_n^m \cos(m\phi) + h_n^m \sin(m\phi)) P_n^m(\cos \theta) (r/a)^n$$

where θ is the colatitude and ϕ is the local time measured from the noon meridian. Obviously, the ring current field does not satisfy $\nabla \times \bar{B} = 0$ within the magnetosphere. Only the field produced by currents on the surface of the magnetosphere can be evaluated in this manner. Following

Mead, the Schmidt normalization is utilized. This normalization is discussed in the Appendix and in Chapman and Bartels (1962), chapter 17, section 17.3 and 17.4. The ordinary associated Legendre polynomials $P_{n,m}$ have the normalization $\int_{-1}^{+1} P_{nm} P_{n',m'} d\mu = \delta_{nn'} \delta_{mm'} \left[\frac{2}{(2n+1)} \right] \left[\frac{(n+m)!}{(n-m)!} \right]$. The Schmidt normalized polynomials P_n^m are related to the Legendre polynomials P_{nm} by $P_n^m = \sqrt{2} \frac{[(n-m)!]}{[\delta_m (n+m)!]} P_{nm}$ where $\delta_m = 1$, except if $m = 0$, whereupon $\delta_m = 2$. Since the dipole axis is assumed perpendicular to the solar wind, the magnetosphere and the geomagnetic fields have two planes of symmetry, the equator and the noon-midnight meridian. Since all current sources are symmetric about the equator yet antisymmetric about the noon-midnight meridian, B_θ is symmetric about both symmetry planes. B_r and B_ϕ are antisymmetric about the equatorial plane, while B_ϕ is also antisymmetric about the noon-meridian plane. As indicated by Mead, these requirements are equivalent to setting three-quarters of the coefficients equal to zero. All the h_n^m coefficients vanish and only the g_n^m coefficients for which $(n+m)$ is odd remain.

Because of these two planes of symmetry, the equator and the noon-midnight meridian, SUR solves for one quadrant of the total surface, and INPUT selects only points within this quadrant. The symmetry of the

problem is handled by XMOD which sets g_n^m equal to zero unless $(n + m)$ is odd.

DANLSB solves for g_n^m by performing a least-squares fit to one of the components of the magnetic field. The data card indicates which component is to be fit, the maximum number of terms which will be used to fit the field, and a specification of which points DANLSB will attempt to fit. After solving for the coefficients, DANLSB returns to each fitting point, calculates, and outputs the vector components of B along with the values which DANLSB was given to fit. The quantity $\sum_{i=1}^N (B_i - B_i(\text{fit}))^2$ is calculated for each component of B and output as an error criteria along with the average value of that component of the input field.

B. Comparison with Mead's Work.

As mentioned previously, copies of the original programs and some personal instruction in their utilization were generously given by Dr. Mead. The general structure of the operation and the basic format of the analysis have been retained. A number of changes designed to increase the accuracy while decreasing the time have been made, however. Specifically, an entirely new decision-making subroutine (MAZE) was formulated; and a new equilibrium criteria, $|\bar{B}_{\text{total}}|^2/2\mu_0 = P$, was utilized (ZEROC). Integration over the surface currents was handled in variable-sized areas designed to increase accuracy while decreasing the time involved (CONTRL). An improved interpolation method of calculating the surface currents was formulated (FLD). An additional 473 points were considered in computing the surface current field expansion coefficients (INPUT). 360 of these were located at the magnetopause where the surface current fields are the largest.

Mead and Beard (1964) used $\hat{n} \times \bar{B}$ in the pressure balance equation $P = |\hat{n} \times \bar{B}|^2/2\mu_0$. This identification was useful in giving a realistic zeroth-order surface and was accurate in giving a self-consistent solution where $|\bar{B}| = |\hat{n} \times \bar{B}|$. At the same time, it introduces

the possibility of multiple solutions for the equilibrium radius. This was most frequently encountered in the noon meridian just above the neutral point for problems involving a transverse pressure in the solar wind. In such a case \bar{B} and \hat{n} were nearly parallel; and although n was nearly perpendicular to the solar wind, the quantity $|\hat{n} \times \bar{B}|$ could be made small enough to satisfy the pressure balance. This condition was easily identified by BZERO's indication of $|\hat{n} \times \bar{B} / \bar{B}|$ much less than .1 over an extended region. This situation was remedied by changing the pressure balance equation to $\bar{B}^2 / 2\mu_0 = P$. In fact, the final self-consistent surface was completely calculated on this basis. Furthermore, if BZERO indicated that MAZE had found an extraneous solution to the condition $|\hat{n} \times \bar{B}|^2 / 2\mu_0 = P$ on any surface, that section of the surface was redone using $\bar{B}^2 / 2\mu_0 = P$.

There is no guarantee that there is an equilibrium radius in existence for each point on the surface during each iteration. In such cases, Mead allowed his version of MAZE to search for local minimums in the pressure difference $(|\hat{n} \times \bar{B}|^2 / 2\mu_0) = P$. However, the use of $|\hat{n} \times \bar{B}|$ also introduced local minimums into the pressure difference function which could satisfy Mead's criteria for an acceptable equilibrium radius even when a true

equilibrium radius existed. To remedy this problem, an entirely new version of MAZE was formulated. The equilibrium radius was identified by a three-stage process. First, the radius was increased in steps of .1% until the external pressure became greater than the internal pressure, or the external pressure began decreasing. Secondly, MAZE proceeded in steps of about .01% until the pressure difference changed sign. This bracketed the equilibrium radius. The third phase located the equilibrium radius within one part in 10^7 by a combination of first and second-order calculations. If no equilibrium point existed, Mead's criteria for locating local minimums in the pressure difference was then utilized.

Mead integrated over the surface currents in areas of 5° in theta and phi. This was extremely detailed for distant regions and very gross for areas adjacent to the observation point. As a result, 10% of the squares contributed 50% of the total value. In fact, the closest eight points, out of a total of 3,200, contributed 10% of the total and most of the error. To improve the accuracy and decrease the time, a new subroutine CONTRL was formulated. This program divides the surface into various-sized areas. Adjacent areas are handled in 1° squares,

and distant areas are handled in squares as large as $15^\circ \times 30^\circ$.

The curvature field was calculated at 10° intervals in theta and 15° intervals in phi. Mead found the field at intermediate points by using a three-point interpolation. Near the subsolar point, Mead assumed that components of the curvature fields were quadratic between 0° and 40° in theta. This assumption seemed to be quite unjustified. For example, the theta dependence of the curvature fields in the noon-meridian plane may be solved for exactly in the case of a dipole field confined to a sphere.

$$\left[B_{\text{curvature}} / (B_0 r_0^{-3}) \right] = \sin \theta \hat{r} + \frac{1}{4} \cos \theta \hat{\theta}$$

The method used here was based on the hypothesis that near the subsolar point the surface current field was much like that due to an image dipole. Thus, the entire surface-current field (not just the curvature field) was transformed to an X,Y,Z coordinate system and interpolated using the symmetries inherent in the problem.

In choosing the surface-current fields to a spherical harmonic expansion, no points beyond $7 R_E$ on the day side were considered by Mead. Such a restriction is both inaccurate and unnecessary. The surface-current fields

are completely specified at each point on the surface. The surface-current field is given by $\bar{B}_{sur} = \bar{B}_{total} - \bar{B}_{internal}$ where $\bar{B}_{total} = 2(\bar{B}_{internal} + \bar{B}_{curvature})$ (See Equation 10) and where the internal field is the sum of the dipole field and the ring-current field. Actually the surface field was defined using the only tangential portion of the total field, i.e. $\bar{B}_{surface} = \bar{B}_{total}^{tangential} - \bar{B}_{internal}$ where $\bar{B}_{total}^{tangential} = \bar{B}_{total} - \hat{n}(\hat{n} \cdot \bar{B}_{total})$. Since \hat{n} and \bar{B} were nearly perpendicular for a self-consistent surface, this correction was insignificant.

Thus, the number of points considered was increased from the 273 points used by Mead (1964) to 746 points. 360 of these additional points were distributed on the surface every 5° in theta and every 10° in phi. 21 points were added at 20, 25, 30, and 35 R_E on the night side, mainly for the closed tail problem.

Several errors found in Mead's programs were corrected. However, Dr. Mead indicated that the programs I received might be programs which were subsequently altered before the final calculation was made. These errors included the interchange of the derivatives of R with respect to theta and phi in Mead's version of MAZE, an error in transforming coordinate systems in INPUT for points on the dipole axis, and a sign error in DDIP in generating $\sin(m\phi)$.

V. THE GEOMAGNETIC FIELD CONFIGURATION.

The effects of the quiet-day ring current and the tail field upon the configuration of the geomagnetic field are presented. The four parameters of the model are calibrated against observations of fields and particles, and the predictions of the model are discussed.

A. Effects of Quiet-Day Ring Current.

The effect of the quiet-day ring current upon the coordinates of the magnetospheric surfaces, the geomagnetic expansion coefficients, and the various geomagnetic field configurations are presented in the following sections.

(i) Surface Coordinates.

The coordinates for the various magnetospheric surfaces are listed in Tables 7 and 8. The surfaces represent the self-consistent solutions to the respective problems. The criteria for a solution to be self-consistent are:

- (1) The surface and surface-current fields changed by less than 1% in two successive iterations
- (2) The geomagnetic field is 95% tangential to the

magnetospheric surface, or else is less than 10% that at the subsolar point.

The "or" provision of the second criteria applies in the vicinity of the neutral points where $(\hat{n} \times \hat{B})$ may only be .2, but the total field is less than 6%. Generally, a self-consistent solution was achieved in four to six iterations (at about 90 minutes each on an IBM 7040).

The coordinates of the magnetopause between a zero-temperature field-free solar wind and a dipole magnetic field are illustrated in Table 7. For a definition of r_0 see Section V-C. The coordinates near the neutral point are given in five-degree intervals for greater detail. These coordinates are within a percent of those listed by Mead and Beard (1964). In general, the equatorial trace ($\phi = 0^\circ$) has a subsolar value ($\theta = 0^\circ$) of $10.73 R_E$, a dawn-dusk meridian radius of $14.64 R_E$, and a maximum cylindrical radius of $19.6 R_E$ (at $\theta = 165^\circ$) assuming r_0 is equal to $10 R_E$. The neutral point is located at a radius of about $9.7 R_E$ near 75° latitude in the noon-meridian plane. The cylindrical radius of the tail in the midnight-meridian plane is 2% less than that in the equatorial plane.

The coordinates of the magnetopause between a zero-temperature field-free solar wind and a dipole field con-

taining the quiet-day ring-current field are listed in Table 8. In the equatorial plane the subsolar radius is $10.94 R_E$, the dawn-dusk meridian radius is $14.46 R_E$, and the tail has a maximum cylindrical radius of $19.4 R_E$ assuming r_0 is $10 R_E$. The neutral point is at $9.5 R_E$ at 75° latitude in the noon meridian plane. The cylindrical radius of the tail in the midnight meridian is about $1\frac{1}{2}\%$ smaller than that in the equatorial plane.

As mentioned previously, if the ring-current field were that of a pure dipole, the surface would be identical to that calculated in the absence of the ring-current field, assuming the subsolar radii were suitably normalized. The non-dipolar aspect of the quiet-day ring current thus increases the subsolar radius by about 2%. In the equatorial plane, the non-dipolar aspect of the ring current leaves the dawn-dusk radius unchanged and decreases the tail radius by about a percent. Other than the 2% increase in the subsolar point, these changes in the equatorial trace are statistically insignificant since the surface accuracy is not asserted to be better than 1%. The other change occurs in the noon-meridian plane. The indentation near the neutral point is enhanced by the non-dipolar aspect of the ring-current field. The neutral point latitude decreases slightly (See Figure 20)

while the radius of the neutral point is decreased by 2%.

The 2% increase in the subsolar radius and the 2% decrease in the radius of the neutral point are consistent with the nature of the non-dipolar aspect of the quiet-day ring-current field. As mentioned previously, the non-dipolar aspect adds to the dipolar ring-current field in the equatorial plane and opposes it in the polar regions. At $10 R_E$ the equatorial enhancement of the dipole aspect is 7%, while the cancellation of the dipole aspect along the polar axis is about 9%. Since the dipole moment of the quiet-day ring-current field is 26% that of the earth, relatively speaking, these non-dipolar effects perturb the dipole field by less than $\pm 2\%$. As such, the quiet-day ring-current field should and does have a very minor effect on the magnetospheric configuration.

(ii) Geomagnetic Field Expansion Coefficients.

The coefficients for the various geomagnetic fields are listed in Tables 10 and 11. Mead's expansion coefficients for a zero-temperature, field-free solar wind incident upon a dipole field are listed in Table 9. The boundary distance r_p^0 is the position of the self-consistent

solution for r_0 equals $10 R_E$. All coefficients are based on $\phi = 0^\circ$ along the subsolar axis. To convert to $\phi = 0^\circ$ at midnight, multiply all coefficients by $(-1)^m$. The coefficients in Table 10 are obtained for the same conditions as those in Table 9; but they are based on 704 points, 360 of which were on the magnetopause and are normalized to $r_b^0 = 10.73 R_E$ instead of $r_b^0 = 10 R_E$. Coefficients through $n_{\max} = 6$ and $n_{\max} = 10$ are presented. As expected, the higher-order coefficients fall off rapidly, but they add detail to the description of the geomagnetic field near the neutral points and in the tail region. The coefficients in the spherical harmonic expansion for a zero-temperature field-free solar wind incident upon a dipole field containing a quiet-day ring current are listed in Tables 11a and 11b. Those in Table 11b are valid only in the noon-midnight meridian plane. Since the moment of the quiet-day ring current is 26% that of the earth, if the ring current were a perfect dipole these coefficients should be 26% larger than those calculated in the absence of the ring-current field (ignoring the difference in the subsolar distance). For example, the leading coefficient $g_{10} = -26.8\%$ for the fit to B_θ in Table 11a should be 1.26 times the leading coefficient $g_{10} = -21\%$ in Table 10; whereas, 1.26 times

-21% is 26.4%. If the plasma-free coefficients were increased by 26%, any difference between these new coefficients and those listed in Table 10 would be caused by the non-dipolar aspects of the quiet-day ring current. The difference is more clearly seen in the actual geomagnetic field configuration discussed in the following section.

(iii) Geomagnetic Field Configuration.

The configuration of the geomagnetic field produced by the interaction of a supersonically streaming plasma with a plasma-free dipole field is illustrated in Figures 14 and 15 (Mead, 1964). The solar wind pressure P has been normalized so that at a distance r_0

$$P = (2B_0 r_0^{-3})^2 / 2\mu_0$$

where r_0 has been chosen as $10 R_E$. This pressure balance ignores the contribution of the curvature field so that r_0 will not be the subsolar distance in the self-consistent calculation. In the self-consistent solution, the curvature field pushes the subsolar point outward to a subsolar distance r_b^0 of about $10.7 R_E$. The neutral-point field line intersects the earth at 83° latitude in the noon-meridian plane. Above this latitude,

the field lines are swept back over the polar caps into the tail. The effect of the field produced by the surface currents is to enhance the geomagnetic field everywhere in the equatorial plane. This is necessary since the dipole flux is now confined to a smaller area by the streaming plasma. This does not mean that the equatorial crossing radius of a field line (defined by the latitude at which it intersects the earth) will be less than it would be in a pure dipole field. This would be true if the surface-current field were not asymmetric and tended to drag field lines toward the night side. Thus on the noon meridian, the 82° field line with $L = 51.6$ in a dipole field is now confined to $10.66 R_E$. On the midnight meridian, the 68° field line with $L = 7.1$ now crosses the equator at $6.67 R_E$.

The projection of the high latitude field lines onto the equatorial plane is shown in Figure 15. At low latitudes they are nearly dipolar and would resemble spokes with a length $L = \sin^{-2}\Lambda$ where Λ is the latitude at which they intersect the earth. At high latitudes they are drawn along the flanks of the magnetosphere and back into the tail. The surface of the magnetosphere consists entirely of field lines which are immediately adjacent to the field lines which intersect

the neutral points in the noon-meridian plane. This is illustrated by the behavior of the field lines at 82° latitude as a function of local times. The closer the field lines get to local noon (in terms of the local time at which they intersect the earth), the closer their intersection with the equatorial plane (denoted by the solid dot at the end of the field line) approaches the surface of the magnetosphere. Field lines above 82° latitude are pulled extremely far back into the tail as can be seen in the noon-midnight meridian (Figure 14).

Dessler and Juday (1965) predicted that the quiet-day ring current would lower the latitude at which the neutral-point field lines would intersect the earth. The results of this calculation, including the quiet-day ring-current field described previously, are shown in Figures 16 and 17. The solar wind has been renormalized so that at r_0 :

$$P = \left[2(B_0 r_0^{-3} + B_{RC}(r_0)) \right]^2 / 2\mu_0$$

for $r_0 = 10 R_E$ where B_{RC} is the ring-current field. This normalization was chosen so that the subsolar distance r_b^0 in the self-consistent solution would be close to the average position of the magnetosphere. Unlike the coefficients for the plasma-free magneto-

sphere, these coefficients cannot be rescaled unless the ring current is also rescaled.

As in the case of the plasma-free magnetosphere, the curvature field will enhance the subsolar field pushing the subsolar point outward. If the ring-current field merely enhanced the earth's dipole field by some constant amount, the boundary shape would be identical to that calculated by Mead. The normalization used would scale the two solutions so that they would agree in size. Since the magnetopause is quite close to the outer portion of the quiet-day ring-current field, the non-dipolar components of this ring current are somewhat significant. As noted previously, the non-dipolar aspect of the ring current enhances the equatorial field and depresses the polar field from what one would expect for an infinitesimally small dipole of the same magnetic moment. This non-dipolar aspect explains why the subsolar point is out further in this solution than in the plasma-free solution. Figures 18 and 19 illustrate the equatorial contours of constant surface latitude and constant magnetic field strength.

The relative effect of the quiet-day ring current can be seen in Figures 20 and 21. In the noon-midnight meridian plane, the ring-current field does push the field lines

outward. The 68° field line in the noon meridian which formerly crossed the equator at $6.3 R_E$ now crosses at $6.9 R_E$. Table 12 illustrates the effect of the ring current on the equatorial crossing radius of high latitude field lines in the noon-midnight meridian.

As Dessler and Juday suggested, the quiet-day ring current pushes field lines outward. However, as seen in Figure 21, the field lines moved around the flanks of the magnetosphere, leaving the surface latitude of the neutral-point field line unchanged.

The inherent stability of this latitude was further evidenced when the field configuration for a dipole field confined to a hemispherical-cylindrical magnetosphere was evaluated. The radius of this magnetosphere was given by $r(\theta) = r_0 + \sin \theta (r_1 - r_0)$ for $0^\circ \leq \theta \leq 90^\circ$ and $r = (r_1/\sin \theta)$ for $90^\circ \leq \theta \leq 180^\circ$. r_0 was set equal to $10.5 R_E$; and r_1 (the radius of the tail cylinder) was set equal to $14.5 R_E$. On the fourth iteration, the geomagnetic field was $\frac{1}{2} \gamma$ at the neutral points and was deemed self-consistent. The neutral points were located near 70° latitude in the noon-meridian plane. The surface latitude of the field line through the neutral points was between 84° and 85° . This result indicates the surface latitude of the neutral-point field line is extremely insensitive to the configuration of the magnetosphere.

Table 7

Coordinates of the surface in units of r_0 (15° intervals) $\phi = 0^\circ$ represents the equator, and $\phi = 90^\circ$ is the noon-midnight meridian. This surface is for a zero-temperature, field-free solar wind, incident upon a plasma-free dipole field.

θ	ϕ						
	0°	15°	30°	45°	60°	75°	90°
0°	1.073	1.073	1.073	1.073	1.073	1.073	1.073
15°	1.086	1.077	1.077	1.074	1.075	1.069	1.067
30°	1.131	1.089	1.090	1.079	1.086	1.057	1.048
45°	1.179	1.121	1.120	1.100	1.104	1.054	1.028
60°	1.238	1.183	1.175	1.147	1.129	1.054	1.018
75°	1.329	1.278	1.267	1.231	1.188	1.086	0.974
90°	1.464	1.418	1.410	1.377	1.330	1.251	1.168
105°	1.696	1.652	1.640	1.615	1.572	1.516	1.467
120°	2.064	2.019	2.012	1.994	1.959	1.915	1.878
135°	2.653	2.605	2.617	2.617	2.599	2.568	2.536
150°	3.868	3.083	3.839	3.859	3.852	3.826	3.789
165°	7.604	7.483	7.577	7.631	7.640	7.599	7.529

Table 7b

Coordinates of the surface near the neutral point (5° intervals)

θ	ϕ				
	70°	75°	80°	85°	90°
60°	1.080	1.054	1.037	1.027	1.018
65°	1.086	1.056	1.032	1.017	1.007
70°	1.100	1.064	1.032	1.007	0.990
75°	1.125	1.086	1.047	1.011	0.974
80°	1.164	1.125	1.085	1.048	1.008
85°	1.216	1.181	1.144	1.112	1.078
90°	1.281	1.251	1.220	1.193	1.168

Table 10

Coefficients in the spherical harmonic expansion for a zero-temperature, field-free solar wind, incident upon a plasma-free magnetic field. Coefficients are fit to 704 points.

The parameter r_p is the distance to the boundary along the earth-sun line expressed in earth radii. Fields are in gamma. r_b^0 is 10.73 R_E .

<u>n,m</u>	$g_n^m(r_b/r_b^0)^{n+2}$	
	Fit to radial component	Fit to theta component
1,0	-21.487843	-21.053521
2,1	- 9.326007	- 8.976395
3,0	- .579561	- .404159
3,2	- 1.531470	- 1.282123
4,1	- 1.104470	- 1.113075
4,3	- .219347	- .230552
5,0	.210934	.253640
5,2	- .260976	- .266085
5,4	- .050942	- .079707
6,1	.026667	.032328
6,3	- .022185	- .025729
6,5	- .005727	- .013956
1,0	-21.348110	-21.038754
2,1	- 9.579613	- 9.289246
3,0	- .545191	- .619692
3,2	- 1.700022	- 1.437448
4,1	- 1.566913	- 1.592725
4,3	- .100536	- .237748
5,0	.192029	.190434
5,2	- .655376	- .444735
5,4	.048851	.132389
6,1	- .207904	- .313866
6,3	- .185882	- .039468
6,5	.038412	.037911
7,0	.075957	.176971
7,2	- .189389	- .188657
7,4	- .068684	- .011230
7,6	.013753	.002213
8,1	.038292	.072258
8,3	- .062020	- .048188
8,5	- .025256	- .010480
8,7	.001697	.000485
9,0	- .002652	- .009453
9,2	.008768	.008817
9,4	.008574	.007004
9,6	- .004623	- .003357
9,8	- .000122	- .000570
10,1	- .000364	- .000842
10,3	.000683	.000384
10,5	- .000445	- .000510
10,7	- .000307	- .000401
10,9	- .000024	- .000130

Table 11

Coefficients in the spherical harmonic expansion for a zero-temperature, field-free solar wind, incident upon a dipole field containing a quiet-day ring current.

The parameter r_p is the distance to the boundary along the earth-sun line expressed in earth radii. Fields are in gamma. r_b^0 is 10.94 R_E .

<u>n,m</u>	<u>$g_n^m(r_b/r_b^0)^{n-2}$</u>	
	Fit to radial component	Fit to theta component
1,0	-26.888483	-25.907758
2,1	-11.594120	- 11.035709
3,0	- .701623	- .371503
3,2	- 1.919406	- 1.592643
4,1	- 1.260566	- 1.166543
4,3	- .161765	- .324590
5,0	.188645	.240891
5,2	- .332250	- .236627
5,4	- .009261	- .098926
6,1	.025179	.025047
6,3	- .030480	- .017864
6,5	.001137	- .012371
1,0	-26.731213	-25.866920
2,1	-11.827835	-11.553705
3,0	- .865551	- .567626
3,2	- 2.116083	- 1.911909
4,1	- 1.921612	- 1.880461
4,3	- .137709	- .416251
5,0	.016740	.293967
5,2	- .821723	- .627451
5,4	.018219	- .169079
6,1	- .442363	- .243079
6,3	- .271656	- .183044
6,5	.005026	- .013257
7,0	.221975	.151323
7,2	- .205558	- .130968
7,4	- .086764	- .080159
7,6	.004377	.008680
8,1	.081358	.053991
8,3	- .043830	- .026468
8,5	- .020861	- .025611
8,7	.003218	.000742
9,0	- .009752	- .005882
9,2	.008962	.005820
9,4	- .005360	- .002886
9,6	- .003059	- .004307
9,8	.000906	- .000524
10,1	- .000751	- .000446
10,3	.000431	.000239
10,5	- .000278	- .000158
10,7	- .000194	- .000289
10,9	.000094	- .000080

Table 11b

Coefficients in the spherical harmonic expansion for a zero-temperature, field-free solar wind, incident upon a dipole field containing a quiet-day ring current.

The parameter r_b is the distance to the boundary along the earth-sun line expressed in earth radii. Fields are in gamma. r_b^0 is 10.94 R_E .

<u>n,m</u>	<u>$g_n^m(r_b/r_b^0)^{n+2}$</u>	
	Fit to radial component	Fit to theta component
1,0	-25.320904	-25.298612
2,1	-15.472236	-17.215658
3,0	- 4.318971	- 2.460572
3,2	- 5.587556	- 6.883759
4,1	- 1.402703	.308482
4,3	1.565482	5.552068
5,0	1.354165	1.315497
5,2	1.050833	1.930261
5,4	1.454568	4.561508
6,1	.186943	.155706
6,3	.247527	.358800
6,5	.222583	.757133

These coefficients are valid only for the noon-midnight meridian planes.

Table 12

Effect of the quiet-day ring current field on the equatorial crossing radius of geomagnetic field lines in the noon-midnight meridian plane.

$r_b = 10.68$ for the plasma-free magnetosphere;
 $r_b = 10.96$ for the magnetosphere containing the plasmas.

Λ	L	<u>Neon Meridian</u>		<u>Midnight Meridian</u>	
		without ring current	with ring current	without ring current	with ring current
60°	4.00	3.90	4.06	3.97	4.12
64°	5.20	4.94	5.25	5.05	5.45
68°	7.13	6.30	6.90	6.67	7.88
72°	10.47	7.88	8.78	9.05	10.77
76°	17.09	9.36	10.01	12.39	13.91
78°	23.13		10.43	14.44	15.85
80°	33.16	10.40	10.73	16.67	17.98
82°	51.6	10.66	10.89	19.02	20.33
84°	91.5	(*)	(32.5)	21.28	22.81
86°	205.5	(*)	(32.12)	*	25.34
88°	821.	(*)	(31.27)	*	27.77
90°		(*)	(29.81)	*	29.81

() - crosses equator on night side

* - field line does not close.

B. Effect of the Tail-Current Field

The effect of the neutral-sheet current is to create a geomagnetic tail composed of field lines which are nearly parallel to the solar wind flow. (See Figure 38 and Ness, 1967 for a review.) This current, which flows across the neutral sheet and along the surface of the geomagnetic tail, is simulated by the quadra-sheet model illustrated in Figure 10. The field at the inner edge of this model is independent of the length of the tail provided the length of the tail L_t is much greater than the radius of the tail R_t . In these calculations, the tail was assumed to be infinitely long.

In joining this quadra-sheet model to the self-consistent solution of the geomagnetic field including the quiet-day ring current, two changes were made in the tail field described in Section III. First, a cutoff of a cyclotron radius was placed on the logarithmic singularity at the inner edge of the current sheet. Physically this means the inner edge of the neutral sheet cannot be located within a cyclotron radius. This cutoff did not significantly alter the flux which crossed the equator within a cyclotron radius r_c of the inner edge of the current sheet. This flux without the cutoff is proportional to $2r_c \left[\ln(r_c/R_t) + 1 \right]$

whereas the flux with the cutoff is $2r_c \ln(r_c/R_t)$. Since $r_c \ll R_t$, the radius of the geomagnetic tail, the flux is approximately the same. Even with this cutoff of 600 km (the cyclotron radius of a 1 keV proton in a 10 γ field) the equatorial geomagnetic field still dips slightly near the inner edge of the current sheet (Figure 37). The second change was that the field B_x parallel to the current sheet was multiplied by $\tanh(y/r_c)$ where r_c is the cyclotron radius of a 1 keV proton in a 10 γ field. This multiplicative factor is based on a self-consistent solution of an infinite neutral sheet (Hoh, 1966). Neither of these changes affected the geomagnetic configuration perceptibly because the total change in flux involved was so small.

The configuration of the geomagnetic field and associated parameters are illustrated for tail fields of 30 γ and 15 γ with the inner edge of the current sheet at $10 R_E$ and $12 R_E$ (Figures 22 through 36). The tail field parameters B_t and R_I will be described by the phrase "a 15 γ field beyond $12 R_E$ " for $B_t = 15\gamma$ and $R_I = 12 R_E$. The radius of the tail R_t was set equal to $20 R_E$ in all the calculations presented herein. Since this quantity appeared in the logarithm of the field perpendicular to the neutral sheet, this field is quite

independent of this parameter.

A typical set includes a side view of the noon-midnight meridian, a top view of the equatorial projection, the equatorial contours of constant polar latitude and the surface latitude of field lines which intersect the equatorial plane at $10 R_E$, as well as the surface latitude of those which close beyond $20 R_E$. The most obvious feature is the substantial effect of the tail field on the nightside configuration and the minor effect produced by a change in the location of the inner edge of the current sheet. Table 13 illustrates this dependence more clearly.

One way of expressing the relative effect of the tail field B_t and the location of the inner edge of the current sheet R_I is that the flux directed southward across the equator between 5 and $15 R_E$ on the nightside is directly proportional to the tail field but only weakly dependent upon the location of the inner edge of the current sheet, provided this edge at which the southward directed flux is strongest is located in the region of interest.

One other comparison of the various parameters is the radial dependence of the equatorial geomagnetic field. (See Table 14 and Figure 37.) Here again, the location of the inner edge of the current sheet has

very little effect; whereas, the tail field can almost double the difference between the geomagnetic field strength and the equatorial dipole field.

In the following section, this model will be calibrated based on observed data.

Table 13

Equatorial crossing radius or height above the neutral sheet of field lines in the mid-night meridian plane for various tail fields.

Λ	L	$B_{R_I}^t$	15 γ 12 R_E	15 γ 10 R_E	30 γ 12 R_E	30 γ 10 R_E
66 $^\circ$	6.		6.59	6.65	6.81	6.97
68 $^\circ$	7.12		8.36	8.56	9.02	10.74
69 $^\circ$	7.8		9.30	9.63	10.26	14.51
70 $^\circ$	8.5		10.19	10.94	(.65)	(.3)
71 $^\circ$	9.4		11.2	12.2	(1.6)	(1.1)
72 $^\circ$	10.5		13.4	13.94	(2.6)	(2.3)
74 $^\circ$	13.2		19.5	19.65	(4.4)	(4.2)
76 $^\circ$			(2.2)	(2.1)	(6.0)	(5.9)
78 $^\circ$			(5.)		(7.5)	
80 $^\circ$			(6.8)	(6.7)	(8.8)	(8.6)
82 $^\circ$			(8.0)	(8.0)		(9.7)
84 $^\circ$			(9.5)	(9.5)		(10.8)
86 $^\circ$			(11.)	(11.)		(11.8)
88 $^\circ$			(12.)	(12.)		(12.6)

Table 14

Equatorial geomagnetic field strength in gammas in the midnight meridian, including the quiet-day ring current field and various quadra-sheet tail fields

R	$B_t = 15\gamma$ $R_I = 10$	$B_t = 15\gamma$ $R_I = 12$	B w/o tail field	Dipole field	$B_t = 30\gamma$ $R_I = 10$	$B_t = 30\gamma$ $R_I = 12$
5	234	236	241	248	227	231
6	130	131	137	144	121	125
6.5	96	97	103	112	87	91
7	71	73	80	90	62	66
7.5	56	59	66	73		51
8	48	51	59	61		43
9	41	46	55	43	26	37
10	22	39	50	31	- 7	28
11	28	28	42	23	14	14
12	23	6	35	18	12	- 23
15	13	11	20	9		2

where B_t is the self-consistent geomagnetic field including the quiet-day ring current field.

B_t is the tail field strength.

R_I is the distance to the inner edge of the current sheet in earth radii.

C. Calibration of the Magnetospheric Model.

The magnetospheric model described in the preceding section has four adjustable parameters:

- R_{ss} the distance to the subsolar point of the magnetosphere
- R_t the radius of the geomagnetic tail
- B_t the magnitude of the magnetic field in the geomagnetic tail
- R_I the distance to the inner edge of the current sheet in the geomagnetic tail.

The distance to the subsolar point R_{ss} is normally between $10.5 R_E$ and $11 R_E$. (See Schild, 1968 for a review.) Although, it has been observed as close as $6.5 R_E$ (Freeman et al., 1968) during magnetically disturbed times. Mead (1964) has shown that the configuration of the geomagnetic field is quite insensitive to the value of R_{ss} . On this basis, a subsolar distance R_{ss} of $10.94 R_E$ has been used whenever the quiet-day ring-current field is included. (See Table 8.)

The radius of the geomagnetic tail R_t has been measured extensively (Gosling et al., 1967) and averages about 17 to $20 R_E$. Although the parameter R_t refers to the radius of the tail perpendicular to the neutral sheet, the tail is nearly cylindrical with a slight

bulge near the neutral sheet so that the equatorial measurements are applicable. Different values of R_t were tested; but since the configuration and magnitude of the geomagnetic field near the equatorial plane is extremely insensitive to this parameter, the tail radius R_t was set equal to $20 R_E$ in all calculations.

Early measurements indicated that the tail field B_t was between 15 and 30% (Ness, 1965). More recently, Behannon and Ness (1966) concluded that the median tail field between 10 and 30 R_E behind the earth was 16%. Based on observations out to 80 R_E , Explorer 33 observed a correlation between the tail field strength and the distance along the tail given by:

$$B_t = (15\% \pm 3.1\%) (25 R_E / -X_{SE})^{0.3 \pm 0.2}$$

where X_{SE} is the solar-ecliptic coordinate directed from the earth to the sun. (See Figure 23 of Behannon, 1968) This decrease between 10 and 80 R_E could be produced by a 2% component of the field crossing the neutral sheet, or by a 10% increase in the size of the tail. The median tail-field strength between 10 and 80 R_E is 10%. Furthermore, the hourly average tail field for $X_{SE} \leq -25 R_E$ is always below 18% for $K_p \leq 2$. On this basis, a tail field of 15% will be used in the following discussion.

The distance R_I to the inner edge of the current sheet in the geomagnetic tail is the most ill-defined parameter of the four. This situation is intrinsic in the nature of the model used to produce the geomagnetic field configuration. This model treats plasmas in two categories: either the magnetic field determines the plasma motion (See the section on the quiet-day ring current), or else the plasmas shape the geomagnetic field (See the section on the tail-current field). However, there is a section of the magnetosphere between 10 and 12 R_E on the nightside of the magnetosphere where the plasmas fall in neither category. These plasmas, moving in the highly distorted geomagnetic field will also tend to pull field lines into the tail region. Thus a direct measurement of R_I , the inner edge of the current sheet, is not available.

An alternative method of evaluating R_I is to see what value provides a best fit to other observations of plasmas and fields. These indirect means of determining R_I include:

- (1) The radial dependence of the equatorial geomagnetic field near midnight should agree with that predicted by the model.
- (2) The observed configuration of the geomagnetic

field near midnight should agree with that predicted by the model.

(3) The equatorial contours of constant magnetic field should agree with the contours of constant flux for high energy particles.

These means of calibration are examined in the following sections.

(1) The radial dependence of the equatorial geomagnetic field near the midnight meridian has been investigated by Heppner et al. (1967). The observed field strength is below the dipole field strength out to at least $12 R_E$. (See Figure 28 of the preceding reference.) A tail field of about 25 to 30 γ was observed on this pass between 14 and 16 R_E . Figure 37 illustrates the difference between the equatorial geomagnetic B_g and dipole B_d fields in the midnight meridian for various combinations of the parameters B_t and R_I . (See also Table 14.) For a given tail-field strength, the difference ($B_g - B_d$) is fairly insensitive to the distance R_I to the inner edge of the current sheet, ignoring the singularity at the inner edge of the current sheet. Furthermore, the configuration of the geomagnetic field is also insensitive to the value of R_I . (See Figures 29 and 33 for a 15 γ tail field.)

The inner edge of the current sheet should not be closer than the inner boundary of the plasma sheet. This distance, observed by Vasyliunas (1968), is between 10 and 12 R_E . Although the plasmas in this region may not be part of the neutral-sheet current, their effect on the magnetic field as measured by Heppner et al. (1967) is closely simulated by a current sheet with an inner edge at 12 R_E and a tail field of 15%.

(2) The configuration of the geomagnetic field near the midnight meridian has been investigated extensively by Ness and by Cahill (Frank, 1966). (See Ness, 1967 for a review.) Figures 38a and 38b illustrate the observed field topology. Cahill's (1966) observations near the midnight meridian indicate that the geomagnetic field is quite regular out to 10 R_E . A more quantitative way of evaluating the structure of the geomagnetic field is given by the radius of curvature of the field line across the axis of symmetry. In a dipole field, the radius of curvature at the equator is given by $(L/3)$. On the nightside of the geomagnetic field according to Cahill, this dipole dependence persists out to about 10 R_E . Beyond this point two things change. First the axis of symmetry shifts from the equator of the dipole field to the antisolar direction in accordance with Ness's

Table 15

R_{EQ}	R_{AS}	r at 30°	$L = (4/3)r(30^\circ)$	Λ
6	6	5.25	6.8	67°
8	8	7	9.25	70°
10	9.5	7.5	10	71.5°
11	11.1	8	10.6	72°
12.8	13.7	9	12	73.2°
14	17	9.5	12.6	73.5°
15.5	?	10	13.3	74°

On this basis, the field line with a surface latitude of 72° closes within $11 R_E$ of the earth; the 73° field line closes within $14 R_E$; and the 74° field line is apparently open beyond $20 R_E$. Since the L value of a 72° dipole field line is $10.5 R_E$, this argument implies that the field is roughly dipolar for field lines below 72° . Above 74° the tail field pulls field lines open beyond $20 R_E$. These results, while interesting, are not as conclusive as the direct observation of the regular nature of the geomagnetic field at $10 R_E$. This implies that the plasma sheet has very little effect on the nightside configuration within $11 R_E$. Although the 15° tilt of the solar wind to the equatorial plane may have some effect, the main source of error, if any, probably lies in the attempt to deduce the specific

path of a given field line from magnetometer measurements. Cahill's observations are consistent with the geomagnetic configuration predicted by this model using a 15% tail field for R_I at either 10 or 12 R_E . The difference between 10 and 12 R_E as the location of the inner edge of the current sheet is too subtle to evaluate.

(3) Iso-flux contours. The contours of constant flux for high-energy particles mirroring equatorially should agree with the contours of constant magnetic field strength. This relation is valid provided the particle energy is sufficiently high so that the fractional change in energy, in drifting through any electric fields, will be so small that the particles will track along contours of constant B while conserving their magnetic moment u . If the source and loss mechanisms have no radial or local time dependence, the number density and flux will also be constant along a contour of constant B.

The local time dependence of 1.6 MEV electrons was observed by Frank (1965) with Explorer 14. Beyond $L \geq 6$ a local time dependence was observed. Using the smallest value of the observed flux, the average iso-flux contour $J_0 \approx 10^2$ e/cm²-sec was at 10 R_E near local noon and beyond 7.5 R_E near local midnight. Had these contours

been correlated with the magnetic field strength, the effect of source and loss mechanisms could be evaluated.

This asymmetry is smaller than this model is capable of explaining. The geomagnetic field at the subsolar point is 76% for a subsolar distance of about 11 R_E . This corresponds to the equatorial dipole field at about 7.5 R_E . If the total geomagnetic field in the midnight meridian is less than that of the equatorial dipole field, the contour of constant B would have to be within 7.5 R_E . Even without any tail field, the quiet-day ring-current field is capable of canceling the field produced by the surface currents and maintaining the geomagnetic field strength below the dipole field strength at the equator. Furthermore, satellite observations of the equatorial geomagnetic field strength (See Section I) confirm that this field is less than the dipole field strength within at least 9 R_E (Heppner, 1967).

There are two explanations for this discrepancy:

(a) The particles Frank measured were not predominantly equatorially mirroring particles. Since the drift of these particles is not necessarily along contours of constant magnetic field strength in the distorted geomagnetic field (Roederer, 1967), their presence will affect the shape of the iso-flux contours in a manner

which depends upon their pitch angle distribution.

(b) Near the subsolar point, the drift velocity of the equatorially mirroring particles beyond $9 R_E$ is only one-eighth of the drift velocity for a particle of the same magnetic moment at the same point in a dipole field. On the nightside, the drift velocity at $7 R_E$ is at least twice as fast as the drift velocity in a dipole field. The dependence of source or loss mechanisms upon local time or radial distance has been neglected. If these effects exist, they will be enhanced by the dependence of the particle's drift velocity upon local time. Future measurements of the pitch angle distribution, the equatorial flux, and the local field should clarify the relationship between the iso-flux contours and the contours of constant magnetic field.

In summary, the calibration of the magnetospheric model against observations of the geomagnetic field indicates that the four variable parameters should be specified by:

$$R_{SS} \approx 11 R_E$$

$$R_t \approx 20 R_E$$

$$B_t \approx 15 \gamma$$

$$R_I \approx 12 R_E$$

The configuration of the geomagnetic field based on these parameters is shown in Figures 33 and 34.

D. Discussion.

A magnetospheric model has been constructed upon a self-consistent solution of the geomagnetic field configuration, including the quiet-day ring current to which a realistic tail field has been joined. This model has been calibrated and the resultant configuration is shown in Figures 33 and 34. This model predicts that the field lines which intersect the auroral oval are not open beyond $20 R_E$ but intersect the equatorial plane within 10 to $12 R_E$. First, the main argument to the contrary which is based on conservation of flux into the geomagnetic tail is analyzed and refuted. The conclusion that the poleward boundary of the auroral zone is identical with the contour of open field lines which extend into the geomagnetic tail is also disputed. Secondly, the equatorial projection of the auroral oval is shown to be coincident with the inner boundary of the plasma sheet observed by Vasyliunas (1968), Freeman and Maguire (1967), and by Frank (1967c).

Conservation of flux has been used to show that the auroral zone may be located on field lines which form the surface of the geomagnetic tail (Dessler and Michel, 1966; Dungey, 1967). The amount of flux in the geomagnetic tail is calculated by assuming a certain size and shape of the

tail and a particular tail field strength. The flux poleward of a given contour near the earth's surface is also calculated. This may be the flux poleward of the 35 kev background boundary. (See Figure 3.) If the field lines in these two regions are the same, the flux they enclose must necessarily be the same.

The strength of the tail field has been discussed in the calibration of the model in Section V-C. The tail field was observed to be between 10 and 18 γ at distances out to the moon with a median value of 16 γ between 10 and 30 R_E . (See Ness, 1967 for a review of magnetic observations.) The geomagnetic tail has an equatorial width of 36 to 40 R_E and is quasi-circular with a slight flattening near the midnight meridian (Gosling et al., 1967; Ness, 1967; Heppner, 1967).

It can be shown that the flux through a semicircle 40 R_E in diameter with a field strength of 20 γ is equal to the amount of flux contained poleward of 75° in either hemisphere (where the equatorial dipole field is .31 gauss). Meanwhile, a tail field of 15 γ , a tail width of 38 R_E , and an elliptical flattening of 4 R_E in radius in the midnight meridian contains the flux poleward of 79° . Previous arguments have utilized higher tail fields, larger tail sizes (Dungey, 1967),

and different shapes (Dessler, 1964) to enclose more flux than is calculated here.

The flux which passes through a contour such as the auroral oval is approximately equal to the flux poleward of its average polar angle. Until the tail flux is known more accurately, this approximation will be sufficient. The 35 kev background boundary (Figure 3) ranges from 71° at midnight to 78° at noon. The flux poleward of this contour is approximately equal to that poleward of 74° . This flux is slightly larger than the maximum tail flux calculated previously. The following table analyzes the approximate flux poleward of various contours.

Table 16

<u>Contours</u>	<u>Range</u>	<u>Average Latitude</u>	<u>Conditions</u>
Open field lines (Figures 28 and 36)	75-83° 70-83°	78° 76°	15% tail 30% tail
Poleward boundary of Feldstein's auroral oval and 35 kev back- ground boundary (Figure 3)	71-78°	74°	
Field lines which intersect equatorially beyond 10 R _E (Figures 28 and 36)	70-76° 68-76°	73° 72°	15% tail 30% tail
Equatorward edge of Feldstein's auroral oval (Figure 3)	65-75°	70°	

Based on the difference between these average latitudes and the 79° average latitude for the tail field lines, there is strong evidence that the poleward boundary of the auroral zone is not located on field lines which are open beyond 20 R_E. This difference provides conclusive evidence that the equatorward boundary of the auroral oval is not located on field lines which extend into the geomagnetic tail.

This conclusion explains why Akasofu (1966) had to use a tail field of 90% to explain the 68° latitude of the equatorward boundary of the midnight auroral zone in the absence of any storm-time ring current, based on the premise that the auroral zone was located on field lines which extended far into the geomagnetic tail.

This magnetospheric model also predicts the equatorial intersection of the field lines upon which the auroral oval is located. The auroral oval utilized here is defined as the region which has a greater than 70% probability of an aurora occurring overhead at that latitude and local time (Feldstein, 1966. See Figure 3) assuming that an aurora could be seen if it existed. The results of this mapping are shown in Figure 39 for a tail field of 15%. This auroral oval includes all types of magnetic conditions. Figure 4 illustrates that the center of the auroral zone moves equatorward as the magnetic activity increases, while the width of the auroral belt simultaneously increases. (See Feldstein and Starkov, 1967 for a review.) During magnetically quiet times, $Q \simeq 0$, the equatorial mapping of the auroral oval is a circular region located about $10 R_E$ from the earth (Figure 40). This equatorial mapping of the quiet-

time auroral oval corresponds very closely to the location of the inner edge of the plasma sheet observed by Vasyliunas (1968) during magnetically quiet times. (See Figure 47.) During polar substorms both Vasyliunas and Freeman and Maguire (1967) observed that the inner edge of the plasma sheet moved inward to about $6 R_E$ (See Figure 47) in agreement with the equatorial mapping of the equatorward edge of the auroral zone for $Q \approx 6$. Note that the outer contour of this mapping also agrees fairly closely with the equipotential contour derived by Taylor and Hones (1965) which is equipotential with the surface of the magnetosphere.

VI. FIELD-ALIGNED CURRENTS AND THE ALFVÉN LAYER.

A. Introduction.

In 1939 Alfvén noted that the convection of a plasma through an inhomogeneous magnetic field produced a charge separation along the boundary of a forbidden region. Alfvén's theory was based on two premises:

- (1) the magnetic field dominates the motion of the plasmas
- (2) an electric field exists which causes plasmas to be convected toward the earth's dipole field.

In applying this concept to the theory of magnetic storms and aurora, Alfvén assumed that the solar geomagnetic field dominated the motion of the solar plasmas and that the emission of the solar plasma (~ 100 MEV) was localized so that the resultant charge separation field would cause the convection of the solar plasma radially outward from the sun. On this basis Alfvén (1939, 1940, 1950) proposed his electric field theory of the aurora and concluded that "If we assume that these two regions of space charge neutralize each other by a discharge along the magnetic lines of force over the polar caps, we can account for the polar disturbances and the aurora."

(1950, p. 182) The auroral zone was, thereby, identified

as "the projection along the lines of force of the boundary of the forbidden region upon the earth." (1950, p. 182) Alfvén's concept of how the field-aligned current system would neutralize unbalanced charge is shown in Figure 41.

During the next twenty years observations of fields and particles were found to be either inconsistent with Alfvén's assumptions or else capable of alternative explanation. Magnetic disturbances were explained by assuming the source currents flowed entirely on the surface of a sphere (Chapman and Bartels, 1962). Thus, field-aligned currents, as originally proposed by Birkeland (1908), appeared to be irrelevant to the auroral-zone current systems. Satellite measurements of the solar wind and the nature of the magnetospheric boundary showed that the assumptions and conclusions made by Chapman and Ferraro (1931, 1932, 1933) were applicable and that some of Alfvén's (1939, p. 4) fundamental assumptions were invalid. Nevertheless, the basic concept that a charge separation would occur when a plasma is convected through an inhomogeneous magnetic field remained valid.

In 1961 Axford and Hines proposed the existence of a convection system in the outer magnetosphere (Figure 42) based upon a viscous-like interaction (Axford, 1964)

between the solar wind and the earth's magnetosphere. An alternative convection configuration whereby the equipotential contours within the magnetosphere join those in the unshocked solar wind has been proposed by Alfvén (1968). However, the Axford-Hines convection system is independent of the magnitude and orientation of the interplanetary magnetic field, whereas Alfvén's configuration is not. The existence of a new source of electric field stimulated work by Swedish scientists on other aspects of Alfvén's original work. As Alfvén had pointed out. "The space charge at the boundary is, on one hand, assumed to be so small as to not disturb the homogeneous electric field too seriously but, on the other hand, is supposed to be able to cause the discharge over the auroral region." (1939, p. 20) This would be possible only if the ionosphere were perfectly conducting. By assuming the ionosphere had an infinite resistivity, a self-consistent solution of the size of the forbidden region and the distribution of space charge was obtained by Karlson (1962, 1963); discussed by Helmer (1963); and extended to the case of a thermal plasma by Block (1966).

Meanwhile, Boström (1964) analyzed the configuration and magnitude of the electric field necessary to drive a

section of the auroral electrojet. When field-aligned currents were assumed to be limited and the field lines were not equipotentials, a longitudinal electric field was sufficient to drive the auroral electrojet as a Cowling current. If the field lines were assumed to be equipotential and field-aligned currents were allowed to flow, the driving electric field was required to be meridional (as proposed by Alfvén) driving the auroral electrojet as a Hall current. Boström proposed that a polar orbiting satellite be used to look for high altitude magnetic disturbances at auroral latitudes. The existence, or absence, of these disturbances and the associated field-aligned currents would be sufficient to determine which model of the magnetospheric electric field was correct.

In 1966 Zmuda, Martin and Heuring reported on the regular observation of transverse magnetic disturbances at 1100 km above the auroral zone with magnitudes of up to 380 γ . Based upon their high degree of localization, these fluctuations were interpreted as being produced by field-aligned currents (Cummings and Dessler, 1967). Meanwhile, the existence of a large scale electric field directed from dawn to dusk with a total potential difference of a few tens of keV was found to be consistent with, and

indeed necessary to explain, the average behavior of various high latitude disturbance phenomena (Brice, 1967). The theoretical justification for magnetospheric circulation inward from the tail was also accomplished (Dessler, 1968). Such an electric field would be expected to cause the plasma in the plasma sheet to drift toward the earth until it reached the boundary of Alfvén's forbidden region.

The inner edge of the plasma sheet extending into the tail has been observed by Vasyliunas (1968). During magnetically quiet times, the inner edge of the plasma sheet is circular with a radius of $10 R_E$ (Figure 47). Alfvén's original electric field theory provides a convenient explanation for both the field-aligned currents and the inner edge of the plasma sheet. However, in order to be valid, Alfvén's theory should meet several fundamental quantitative tests:

- (1) The location of the inner edge of the plasma sheet should coincide with the predicted size of the forbidden region using the observed values of the convection field and the distribution of plasma magnetic moments.
- (2) The auroral zone should be located on field lines which intersect the inner edge of the plasma sheet.

- (3) The magnitude of the field-aligned currents flowing onto the auroral zones should equal the current necessary to discharge or neutralize the unbalanced charge in the Alfvén layer.

The last two tests were first proposed and evaluated by Alfvén (1939, p. 22 and 33).

B. The Size of the Forbidden Region.

The size of the forbidden region is determined by the drift path of the charged particles. For equatorially mirroring particles the drift paths are specified by:

$$(14) \quad q\bar{\phi} + \mu B = \text{constant}$$

where q is the charge of the particle, $\bar{\phi}$ is the potential of the electric field, μ is the magnetic moment of the particle and B is the magnetic field strength. The equatorial drift-path equation (14) may be obtained from the drift velocity equation:

$$(15) \quad \bar{v}_D = \left\{ \left[-\bar{\nabla}(q\bar{\phi} + \mu B) + \bar{f}_i \right] \times \bar{B} \right\} / (qB^2)$$

by ignoring inertial forces \bar{f}_i . The magnetic moment μ is proportional to I_1/γ where I_1 , the first adiabatic invariant (Alfvén and Falthammer, 1963, p. 37) equals p_{\perp}^2/B and where γ is the relativistic factor $(1 - (v/c)^2)^{-1/2}$. Normally, the fractional change of γ along the drift path is so small that the magnetic moment is assumed to be a constant of the motion.

The innermost drift paths of electrons and protons with identical magnetic moments which are being convected equatorially through a dipole field from infinity by

a uniform electric field are shown in Figure 43 (after Alfvén, 1939). The charge separation field is neglected. The forbidden region describes the central region to which both protons and electrons convected in from infinity do not have access. The Álfvén layer will henceforth be used to describe the region of unbalanced charge. For equatorially mirroring particles, the number density along the drift path is proportional to the magnetic field strength (Alfvén, 1939) so that in Figure 43 there is no unbalanced charge at any point to which both electrons and protons have access. (Assuming the existence of a neutral plasma in a uniform magnetic field at infinity.) In this case the Álfvén layer is the region between the innermost drift paths to which either protons or electrons do not have access (the shaded regions in Figure 43). The size of the forbidden region in Figure 43 may be described in units of Álfvén's (1939) L where:

$$(16) \quad L = \left[\frac{\mu B_0}{qER_E} \right]^{1/4} = 5.3 R_E \left[\frac{\mu(100 \text{ ev}/\gamma)}{zE(\text{mv/m})} \right]^{1/4}$$

The radius of the point of zero drift velocity is given by $1.32 L$, while the minimum radius of the forbidden zone is $0.74 L$. These numbers are valid when the charge separation

field is ignorable (i.e., when the ionosphere is perfectly conducting).

If the ionosphere is not perfectly conducting, then the magnitude and configuration of the charge separation field and the distribution of magnetic moments in the plasma will influence the size of the forbidden region. Any charge separation field will oppose the driving convection field within the forbidden region and enhance it in the dawn-dusk meridian plane, thus decreasing the size of the forbidden region slightly. If the charge separation field completely cancels the driving convection field within the forbidden region, it will enhance the driving field at the point of zero drift velocity by a factor n where n is between one and three, decreasing the size of the forbidden region by less than 25%. However, if the plasma is thermalized with a temperature T , the size of the forbidden region will be larger than it would have been for a plasma with particles of a single magnetic moment $\mu = kT/B$ (Block, 1966). This is because the charge separation of the higher energy particles occurs at larger distances, thereby altering the equipotential contours and the paths of the lower energy particles. Specifically, Block found that if the

magnetic moments had a Maxwellian distribution and if the ionosphere were nonconducting, the boundary size would be determined by particles whose magnetic moments were 60 times the most probable magnetic moment. In this case the size of the forbidden region is given by:

$$(17) \quad L' = (20)^{\frac{1}{4}} L = 11.2 R_E \left[\frac{\mu_p (100 \text{ ev}/\delta)}{E_C (\text{mv/m})} \right]^{\frac{1}{4}}$$

assuming $n = 3$ where E_C is the magnitude of the driving electric field and μ_p is the most probable magnetic moment.

Since the ionosphere is neither a perfect conductor or a perfect insulator, the actual size of the forbidden region should be somewhere in between those defined by Equations 16 and 17. The most probable magnetic moment μ_p for plasma sheet particles is 25 ev/ δ based upon $E_0 = 500$ ev (Vasyliunas, 1968) and $B \approx 20\%$. The magnitude of the convection field is probably between .1 mv/m and .5 mv/m corresponding to potential drops of ~ 20 and ~ 100 kv respectively across the dawn-dusk meridian of the magnetosphere, taken as $30 R_E$ (Brice, 1967). Using these limits of the driving convection field, L is between 4.5 and 6.6 R_E , while L' is between 9.5 and 14 R_E .

The location of the inner edge of the plasma sheet has been observed by Vasyliunas (1968) (See Figure 47) in the dusk to midnight sector and by Freeman and Maguire (1967) in the midnight-dawn sector. Figure 44 illustrates the general shape of the inner edge of the plasma sheet based on these experimental observations and upon theoretical considerations (Taylor and Hones, 1965). Between 1700 and 2200 LT Vasyliunas noted that in the absence of bay activity the plasma sheet is between 10 and 12 R_E , whereas during bay activity the plasma sheet moved inward to as close as 5.5 to 6 R_E . Freeman observed the plasma sheet at 6.5 R_E only during magnetically disturbed times.

Thus, it appears that during magnetically quiet times, the location of the inner edge of the plasma sheet is in fair agreement with the theoretically predicted size of the forbidden region provided the charge separation field is not negligible. Although the actual geomagnetic configuration and the presence of a corotation electric field will modify the drift paths somewhat (Kavanagh et al., 1968), Alfvén's basic description of the size of the forbidden region remains essentially unchanged, assuming the effect of the charge separation field is ignorable. Thus, in order for the theory to agree with the observed location of the inner edge of the

plasma sheet, the charge-separation field must be significant. This is argued to be true in Section VI-D.

C. The Auroral Zones and the Alfvén Layer.

The configuration of the geomagnetic field has been evaluated in Section V. The shape of the magnetosphere is solved self-consistently in the presence of the quiet-day ring current while neglecting the existence of the neutral sheet currents. A realistic tail field, which simulates the flow of the tail currents along the surface of the magnetosphere, was utilized to deform the nightside geomagnetic field lines. The geomagnetic field configurations in the noon-midnight meridian and as projected onto the equatorial plane are shown in Figures 33 and 34 respectively. A tail field of 15γ with an inner edge at $12 R_E$ is utilized. This configuration compares quite well with nightside magnetic field measurements (Figure 38).

The model is not entirely self-consistent in that plasmas in the region of $\beta \approx 1$ are not included where $\beta = nKT/(B^2/2\mu_0)$. These plasmas are located between the inner edge of the plasma sheet (the Alfvén layer) and the neutral line. (See Figures 45 and 2.) The magnetic field produced by these plasmas will pull nightside field lines toward the plasma sheet and thus lower the latitude of the boundary of trapping. However, the effects of these plasmas have been used to calibrate

the magnetospheric model used here. On this basis, the configuration illustrated in Figures 33 and 34 is expected to accurately describe the geomagnetic field.

The most obvious feature of this model is that the field lines which intersect the auroral oval do not map onto either the neutral sheet or the surface of the magnetosphere but are buried deep within the magnetosphere. The equatorial mapping of the auroral oval (Figure 4) during magnetically quiet times is shown in Figure 40. The inner edge of the plasma sheet (Figure 47) appears to be coincident with the magnetic field lines that map onto the auroral oval (Figure 40). This relationship is illustrated in Figure 45.

D. The Field-Aligned Currents and the Alfvén Layer.

The field-aligned current necessary to neutralize the unbalanced charge in the Alfvén layer is proportional to the thickness of the layer. This thickness is examined theoretically and experimentally and is found to be consistent with the width of the auroral region of transverse magnetic disturbances. The current necessary to neutralize the unbalanced charge is evaluated and is found to be sufficient to produce the transverse magnetic disturbances observed by Zmuda et al. (1966) at auroral latitudes.

(i) The Thickness of the Alfvén Layer.

The Alfvén layer is taken to be the outer edge of the forbidden region where the convection of plasma produces an unbalanced charge. In Alfvén's model (Figure 43) the Alfvén layer had a maximum thickness of $0.6 L$. For plasma sheet particles with magnetic moments of about $25 \text{ ev}/\gamma$ and an electric field of 0.25 mv/m , the maximum thickness of the Alfvén layer would be about $4 R_E$ (Equation 16). Since the effects of any charge separation were ignored, this model would be valid only if the earth's ionosphere were a perfect conductor.

In the opposite case of a non-conducting ionosphere, the maximum charge separation field across the forbidden zone should be the order of the original convection field. The unbalanced sheet-charge required to produce a field of about a millivolt per meter is $\sim 6 \text{ e/cm}^2$. Unless neutralization currents are permitted, the thickness of the Alfvén layer must be correspondingly small. If both protons and electrons have a single magnetic moment, the thickness of the Alfvén layer is the order of $(v_{\text{ExB}}/v_{\text{T}})$ times the cyclotron radius of the particle involved, where v_{ExB} is the ExB drift velocity and v_{T} is the total speed of the particle (Helmer, 1963, Eq. 15). In a 20 γ magnetic field and a 1 mv/m electric field, this thickness $\delta r = mE/(qB^2)$ is 25 km for protons, 15 meters for electrons, and is independent of their energy and number density. However, if the plasma is thermalized, the thickness of the Alfvén layer is the order of a Debye length which is about 300 meters for $\hat{C}_0 \approx 1 \text{ kev}$ and $n_e \approx 1 \text{ cm}^{-3}$ (Block, 1966). In summary, the thickness of the Alfvén layer is theoretically expected to be between a kilometer and several earth radii depending entirely upon the conductivity of the ionosphere.

Experimental observations of the inner edge of the plasma sheet by Vasyliunas (1968) indicate that the Alfvén boundary is really a boundary in energy and not in number density (Figure 46). The energy dependence of particles in the Alfvén layer is examined in Section VI-E. One result of that evaluation which is necessary here is that the region of unbalanced charge is defined by the region over which the energy of the plasma changes significantly. This correspondence is caused by the nature of the particles which carry the neutralization currents to and from the Alfvén layer. Vasyliunas found that the electron energy density had a scale length of 0.4 to 0.6 R_E and decreased by an order of magnitude in about 1 R_E .

If the theory of Alfvén is correct, the width of the Alfvén layer should map onto the width of the region of transverse magnetic disturbances. The average width of the latter region is 3 to 4° latitude during magnetically quiet times and increases to between 4 and 6° for $K_p \geq 4$ (Zmuda et al., 1966). However, latitudinal widths as small as 24 km or $\frac{1}{4}$ ° latitude have been observed (Zmuda, personal communication). In a dipole field the latitudinal width $d\Lambda$ between two magnetic shells is related to their equatorial width dL by $dL = L \tan \Lambda d\Lambda$. For $L = 6$ this

reduces to $dL(R_E) = d\Lambda(^{\circ})/4$, while for $L = 10$, $dL(R_E) = d\Lambda(^{\circ})/2$. On this basis, the $1 R_E$ width of the Alfvén layer corresponds to auroral zone widths of 2 to 4 $^{\circ}$. These values are in general agreement with the width of the region of transverse magnetic disturbances. A more precise evaluation can be made using the geomagnetic field configuration illustrated in Figure 33. The 2 $^{\circ}$ separation between the 66 and 68 $^{\circ}$ field lines maps onto an equatorial separation of $2 R_E$ in the midnight meridian, as does the 2 $^{\circ}$ separation between 68 and 70 $^{\circ}$. In the noon meridian, the 4 $^{\circ}$ separation between the 72 and 76 $^{\circ}$ field lines also maps onto an equatorial separation of $1 R_E$. Although the correspondence of these widths is fairly good, it appears that the width of the Alfvén layer should be somewhat larger than that observed by Vasyliunas. It may be that Vasyliunas was experimentally unable to observe the full width of the Alfvén layer. Observations by Frank (1967c) indicate that the Alfvén layer may be at least $1.5 R_E$ thick.

The correspondence between the width of the Alfvén layer and the width of the zone of transverse magnetic disturbances is indicative of a fundamental relationship between the two. In Section (ii) the current necessary to neutralize the unbalanced charge in the Alfvén layer is

evaluated. In Section (iii) this current is found to be sufficient to produce the transverse magnetic disturbances observed by Zmuda et al. (1966).

(ii) The Field-Aligned Current.

As shown in the preceding section, a field-aligned current is necessary to neutralize the excess charge in an Alfvén layer which is more than a Debye length thick. This neutralization current is approximately equal to the rate at which the charge separation of the plasma sheet particles occurs. The rate of charge separation in the Alfvén layer is the product of the charge density, the drift velocity, and the area of the Alfvén layer. This area is on the order of the area between two dipole field lines $(LdL)R_E^2$. The drift velocity is the order of E_c/B where E_c is the magnitude of the driving convection field. The charge separation field and gradient drift should increase this drift velocity by less than a factor of six. On this basis, the total current I_N necessary to neutralize the unbalanced charge in the Alfvén layer is given by:

$$(18) \quad I_N = 2 \times 10^6 \text{ amps} \left[n_e (\#/cm^3) E_c (\text{mv/m}) (L/10)^4 dL \right]$$

Letting $E_c = 0.3 \times 10^{-3}$ volt/m and $dL = 1$, the total

current is about 5×10^5 amps for $n_e = 1 \text{ cm}^{-3}$ and $L = 10$, and is about 2×10^6 amps for $n_e = 10/\text{cm}^3$ and $L = 6$.

The magnitude and configuration of the neutralization current depends on the nature of the particles which carry the current, as well as on the location of the Alfvén layer. The subsequent motion of the charge neutralization particles may easily produce a second-order charge separation which will require an additional flow of neutralization current. If, for example, neutralization is carried out entirely by thermal ionospheric electrons and protons ($\mu \approx 0$), their subsequent motion will be along electric equipotentials. In the case of an infinitely conducting ionosphere, these thermal particles will create a second-order charge separation as they move outside the Alfvén layer. A subsequent neutralization by thermal particles will remove this charge separation.

(iii) Effects of Neutralization Currents.

If the field-aligned currents are driven by the charge separation in the Alfvén layer, the field produced by these currents should agree with the magnitude of the transverse magnetic disturbances observed by Zmuda et al. (1966). The neutralization-current field may be esti-

mated by confining the field-aligned currents onto two parallel sheets on adjacent L shells. This configuration is explained in the section on the energy dependence of particles in the Alfvén layer. (See Figure 49.) A neutralization current I_N of 10^6 amps will produce a current sheet of 77 ma/m for $\Lambda = 66^\circ$ using $J_s = I_N / (2\pi R_E \cos \Lambda)$. These currents would produce a field of 92.5% between the sheets using $B(\%) = 1.2 J(\text{ma/m})$. The maximum amplitude of the transverse magnetic disturbances observed by Zmuda et al. (1966) was 380% , and 68% of the amplitudes were below 150% . The most probable amplitude appeared to be between 50 and 100% in direct agreement with the predicted values. Since Zmuda observed transverse magnetic disturbances above 30% about 90% of the time, the actual configuration of the neutralization current system should be more nearly like two parallel sheets than the coaxial cable configuration utilized by Cummings and Dessler.

The power dissipated by ohmic losses is given by $P = I^2 \ell / (\sum_p W)$ where I is the current to be discharged, \sum_p is the height integrated Pederson conductivity. $\sum_p = \int_0^h \sigma_p dh$, where ℓ is the path length measured parallel to the current flow, and W is the width of the current sheet. The minimum power is dissipated in the parallel-

sheet geometry when the current flows meridionally across the zone of transverse magnetic disturbances and does so at every longitude. Taking the width as 4° or 500 km, the length as $2\pi R_E \cos(66^\circ)$ or 1.3×10^7 m and the current as 10^6 amps, the power dissipated is $(3 \times 10^{10} / \Sigma_p)$ watts. Σ_p is between 1 and 30 mho (Boström, 1967) so that the minimum power is between 10^9 and 3×10^{10} watts (10^{16} to 3×10^{17} ergs/sec). The higher conductivity is valid for the interior of an auroral arc 10 km wide; the lower conductivity is for the undisturbed ionosphere. Since the 4° width of region of transverse magnetic disturbances is much wider than 10 km, the lower conductivity should be applied. The minimum power dissipated by the field-aligned currents is comparable to the power dissipated in the aurora. Sharp and Johnson (1968) concluded that the average power precipitated by particles above 200 ev is about 2×10^{10} watts (about 0.07% of the solar wind energy incident upon the magnetosphere); but during magnetic storms, the maximum power dissipated was $\approx 6 \times 10^{10}$ watts/sec.

E. The Energy Dependence of Particles in the Alfvén Layer.

The most characteristic feature of the inner boundary of the plasma sheet is the downward shift in the particle energy with decreasing radial distance. Figure 46 illustrates the energy E_0 of the most probable flux, the electron density n_e , and the electron energy density U during a typical inner boundary crossing when no magnetic bays were present (Vasyliunas, 1968). These quantities were calculated by fitting an assumed functional form representing a broadly peaked thermal distribution with a power-law, high-energy tail to the measured currents in the four energy windows between 100 ev and 2 kev (40 ev on OGO-3). In the plasma sheet $n_e \approx .8 \text{ cm}^{-3}$, $E_0 \approx 500 \text{ ev}$, and $U_e \approx 1 \text{ kev/cm}^3$. As the satellite proceeds inward, the energy of the most probable flux rapidly decreases across the boundary dropping to $\approx 150 \text{ ev}$ while the number density increases slightly (from .8 to $\sim 1 \text{ e/cm}^3$). The energy density decreases approximately exponentially with decreasing distance, having a scale width of $.4 R_E$, and an order of magnitude decrease in $1 R_E$. Thus, the inner boundary is not a boundary in density but in average electron energy.

This peculiar energy dependence of particles in the Alfvén layer is not what one might expect. The density

and the energy of a convected plasma should each be proportional to the magnetic field strength ignoring inertial effects (Helmer, 1963). The energy density should slowly increase as the plasma is convected earthward. In a dipole field, the energy scale height $H = \mathcal{E} / |\partial\mathcal{E}/\partial r|$ would be $r/3$ along the path of a plasma being convected radially.

One possible explanation for this peculiar energy dependence is that the more energetic particles are excluded from the inner edge of the Alfvén layer. This is automatic in the case of a perfectly conducting ionosphere where the size of the forbidden region increases with energy (Equation 16). A more general form for the size of the forbidden region which fits all the limiting cases is

$$(19) \quad r_0 = (f\mu_p B_0 / qnE_c R_E)^{1/4} (\mu/\mu_p)^{1/m}$$

where μ_p is the most probable magnetic moment and where m , n , and f are functions of the charge separation field. The dependence of the size r_0 of the forbidden region on u is contained in the factor $(\mu/\mu_p)^{1/m}$. In the case of a perfectly conducting ionosphere, there is no charge separation field; and m equals 4 and $f = n = 1$. In the case of a nonconducting ionosphere, m approaches infinity.

The resultant charge separation field enhances the driving convection field by a factor n which is between one and three. The factor f indicates the dependence of the size of the forbidden region on the shape of the spectrum; and as m approaches ∞ , f approaches 60 (Block, 1966).

Since μ is $\mathcal{E}/B_0 r^{-3}$ in a dipole field, the energy dependence of the size of the forbidden region $\partial r_0/\partial \mathcal{E} = -r_0/(m\mathcal{E})$ can be used to give the energy dependence of the Alfvén layer thickness:

$$(20) \quad H = \mathcal{E} \left| \partial r_0 / \partial \mathcal{E} \right| = (r_0/m)$$

A scale height of $0.4 R_E$ at $r_0 = 10$ requires that $m \geq 25$. This value implies that the charge separation must have some effect if this explanation is valid. However, one result of this idea is that the number density of the convected particles should decrease toward the inner edge of the Alfvén layer. In fact, for a very flat number density distribution, the number density below a given energy is proportional to the energy so that the scale height of the number density is the same as that of the energy. The presence of plasma which is trapped on closed drift paths might possibly mask this effect. A second result of this idea

is that the energy dependence of the Alfvén layer should be independent of the local time and of the sign of the charge.

An alternative explanation of the energy dependence of particles in the Alfvén layer is that the field-aligned current is carried by low-energy particles. The configuration of the neutralization current depends on the distribution of charge in the Alfvén layer. If the convection field is directed from dawn to dusk, the current in Figure 3 would flow from the dusk side of the magnetosphere down to and across the polar caps and finally to the dawn side. If inertial effects are included, Helmer (1963) has shown that regions of net positive and negative charge will form on both the dawn and dusk sides of the magnetosphere when $\mu_i = \mu_e$ and $m_i = m_e$ (Figure 48). In this case, the field-aligned current may flow onto and across the auroral zone and then flow back onto the equatorial plane without crossing the polar cap in order to complete the discharge. The profile of the most probable energy for both protons and electrons is shown in Figure 49, along with the assumed configuration of the field-aligned current system. The particles carrying the current are assumed to be below 200 ev. The energy of the peak flux increases whenever

low-energy particles are removed and decreases whenever low-energy particles are added.

The radial dependence of energies in the Alfvén layer as predicted by this mechanism is also compatible with Vasyliunas's observation that the peak energy of electrons decreases inwardly on the dusk side of the magnetosphere. If this mechanism is effective, the energy dependence of particles in the Alfvén layer should have a dawn-dusk asymmetry as well as an asymmetry depending upon the charge of the particle being observed. (See Figure 49.)

F. Nature of Particles in Field-Aligned Currents.

It remains to be shown that the field-aligned currents must be carried by low energy particles. In order to do so, the minimum field-aligned neutralization current density and the associated particle flux are estimated. After investigating the distribution of flux both observationally and theoretically, it is concluded that only particles below 2 ev or around 80 to 100 ev have sufficient flux to carry the required current. This conclusion substantiates the assumption made in the previous section.

The minimum field-aligned current density can be estimated by distributing the 10^6 amp neutralization current over the zone of transverse magnetic disturbances. The current density for $\Lambda = 66^\circ$ and $d\Lambda = 4^\circ$ is .14 microamp/m²; and the maximum current for $d\Lambda = (\frac{1}{4})^\circ$ (Zmuda, personal communication) is 3 $\mu\text{A}/\text{m}^2$. A net flux of 6.25×10^8 e/cm²-sec is required to carry a current of 1 $\mu\text{A}/\text{m}^2$.

(i) Differential Flux Spectra.

Little is known about the flux distribution between thermal energies and 1 kev. Figure 50 illustrates observed auroral zone fluxes between 1 and 10 kev, and the expected flux for a Maxwellian distribution of electrons

having a density of 10^6 e/cm³ and a temperature of 3000° K (Ulwick, 1966). If the spectrum between 100 ev and thermal energies is above 10^8 e/cm²-sec-ster-ev, then fluxes at any of these energies would be sufficient to carry the required neutralization currents.

A relative maximum in the flux distribution is expected at about 80 to 100 ev. A relative maximum should exist because for sufficiently low energies the particles spend enough time at the mirror point to come to equilibrium with the thermal ionosphere. This occurs when the bounce time of a trapped electron is less than or equal to the time for equipartition of energy to occur between this trapped electron and the thermal electrons in the ionosphere. The bounce time of an electron in a dipole field is $(2.5 L/\sqrt{\mathcal{E}_e(\text{ev})})$ seconds. (See Johnson, 1965, p. 56.) The equipartition time among electrons of two energies is given by: (Spitzer, 1962, p. 135)

$$\tau_{\text{eq}} = \left[.177 \times 10^6 / (n_f \ln \Lambda) \right] \left[\mathcal{E}_e(\text{ev}) + \mathcal{E}_f(\text{ev}) \right]^{3/2} \text{ seconds.}$$

Equating these times using $\ln \Lambda = 14$ and ignoring the thermal energy in comparison with the expected energy of the maximum flux, this latter energy is given by:

$$\mathcal{E}_e(\tau_{\text{bounce}} = \tau_{\text{eq}}) = 90 \text{ ev} \sqrt{L/9} \sqrt{n_e/10^6 \text{ e/cm}^3}$$

The bounce and equipartition times are both .3 seconds for a 90 ev particle at $L = 9$ and $n_e = 10^6$ e/cm³.

A peak in the flux spectrum at about 80 ev has been observed by Westerlund (1968). Below this energy, the flux falls off rapidly (by an order of magnitude in less than 40 ev). The difference between this energy and the energy of the peak flux in the equatorial plane of ≈ 500 ev is produced by thermal interaction of the ionosphere on those particles. Westerlund also observed that the change in the peak energy per L shell was about 16 ev per L shell for L between 9 and 12 (Figure 51). This is in fair agreement with the predicted value of about 5 ev per L shell. The scale length for the peak energy $H = (\partial L / \partial \mathcal{E}_{pk}) \mathcal{E}_{pk}$ is $2L$ so this mechanism cannot produce a sharp boundary in the equatorial plane, especially among the equatorially mirroring particles since the equipartition time for electrons in the plasma sheet ($n_e \sim 1$ cm⁻³, $\mathcal{E}_e \approx 100$ ev) is 10^8 seconds based on Coulomb collisions (Spitzer, 1962). One would have to postulate an interaction time which was equal to the time necessary for the plasma to drift from open field lines inward to the inner edge of the plasma sheet.

(ii) Number density.

Although either thermal fluxes or 100 ev fluxes are capable of carrying the required neutralization current, their difference in speeds means that the density of thermal particles will have to be $\sqrt{100/.25} = 20$ times larger. If a current of $1 \mu\text{A}/\text{m}^2$, requiring a net flux of $6.25 \times 10^8 \text{ e}/\text{cm}^2\text{-sec}$, were carried entirely by ionospheric electrons and protons at their respective thermal speeds ($\hat{C}_e = \hat{C}_p = \frac{1}{2} \text{ ev}$ for $T = 3000^\circ \text{ K}$), number densities of $n_e = 20 \text{ e}/\text{cm}^3$ and $n_p = 900 \text{ p}/\text{cm}^3$ would be required. In the equatorial plane, the flux and the respective number densities are multiplied by ($B_{\text{eq}}/B_{\text{surface}} \approx .5L^{-3}$) assuming that the fluxes are entirely parallel to the magnetic field. At $L = 10$ the equatorial values are about three orders of magnitude below the auroral zone values. The flux at .25 ev is now $5 \times 10^5 \text{ e}/\text{cm}^2\text{-sec}$ and the number densities are $0.02 \text{ e}/\text{cm}^3$ and $1 \text{ p}/\text{cm}^3$ respectively.

Since the number density required for ionospheric protons to carry the required field-aligned current at their thermal velocity is approximately equal to the number density of protons in the plasma sheet, the current from the ionosphere to the plasma sheet must be carried by plasma sheet electrons, as well as by ionospheric

protons. Furthermore, the drift of electrons at speeds above the thermal velocity of the protons may produce limiting instabilities (Farley, 1963). If so, then both low-energy protons and electrons in the plasma sheet must carry some of the required field-aligned currents. Furthermore, if plasma-sheet electrons are carrying the current from the ionosphere, any precipitation of protons will increase the required fluxes and number densities. Although the required number densities for plasma sheet particles are 20 times less than that for ionospheric particles, unless the net-charge flux is greater than 5% of the total flux, the advantage of higher speed is negated.

In order for these 100 ev particles to carry a net current along the field line, the pitch angle distribution must be strongly peaked at either 0° or 90° above the auroral zone. For example, on the dusk side of the magnetosphere, the high-latitude current flow is away from the earth. The pitch angle distribution of 100 ev electrons should be strongly peaked along the field line in order to carry the current. This is consistent with Westerlund's (1968) observation. Note that this concept contains three observable asymmetries: a day-night asymmetry, a latitude asymmetry, and a charge asymmetry.

The addition of an electric field which is anti-parallel to the magnetic field in the Northern Hemisphere will increase the precipitation of low-energy trapped electrons, decrease the precipitation of low-energy trapped protons and leave the precipitation of higher energy protons and electrons unchanged. By using conservation of magnetic moment

$$\mu = \mathcal{E}_{eq} \sin^2 \alpha_{eq} / B_{eq} = (\mathcal{E}_{eq} \sin^2 \alpha_{eq} + (q\Delta\mathcal{A}_{||} + \mathcal{E}_{eq} \cos^2 \alpha_{eq})) / B_m$$

or using the magnetic mirroring criteria

$$\int_{B_{eq}}^{B_m} \mathbf{F} \cdot d\mathbf{l} = \mathcal{E}_{eq} \cos^2 \alpha_{eq} = q\Delta\mathcal{A}_{||} + \mu(B_m - B_{eq})$$

it can be shown that

$$B_m / B_{eq} = \sin^{-2} \alpha_{eq} (1 + q\Delta\mathcal{A}_{||} / \mathcal{E}_{eq})$$

where B_m is the value of the magnetic field at the mirror point, B_{eq} is the value of the magnetic field at the equator of the same field line, α_{eq} is the equatorial pitch angle, \mathcal{E}_{eq} is the total energy of the particle at the equator, and $\Delta\mathcal{A}_{||}$ is the potential difference along the field line between the equator and the mirror point. If $q\Delta\mathcal{A}_{||} \approx \mathcal{E}_{eq}$, then the mirror field is either halved or

doubled, a very significant change. If ϕ_{eq} is ≈ 800 ev in the plasma sheet, then changing the ratio of B_m/B_{eq} by 5 to 10% requires that $q\Delta\phi_{||}$ be about 100 ev. This value of $q\Delta\phi_{||}$ was also deduced by Boström (1964), based on a parallel conductivity of 2 mhos between 90 and 1000 km and a field-aligned sheet current of 2 amps/meter one kilometer thick ($J = 2 \text{ ma/m}^2$). The potential drop along the field line cannot be much more than a few hundred electron volts (Mende, 1968) unless the conductivity is reduced by some plasma instability (Swift, 1965).

G. Discussion.

The thickness of the Alfvén layer is quite significant theoretically. The fact that it is thicker than a kilometer means that neutralization currents must exist. The fact that it is thinner than several earth radii (Figure 46) indicates that the charge separation field does influence the drift motion of the plasma sheet particles. Two other factors indicate the existence of a charge separation field. First, the lack of an energy dependence in the size of the forbidden region ($m \gg 4$ in Equation 20) is a necessary condition. If the charge separation field were ignorable, the size of the forbidden region would have an energy scale height of $(L/4) \geq 1.5 R_E$, whereas Vasyliunas (1968) observes a scale height of $0.4 R_E$. Second, the predicted size of the forbidden region is much smaller than the distance to the inner edge of the plasma sheet unless a charge separation field exists. However, all three of these arguments are necessary but not sufficient conditions for the existence of a charge separation field. The field-aligned currents could mask these effects.

The argument that a strong pitch angle diffusion process will produce particle transport along field lines owing to the difference in the precipitation rate

for protons and electrons has been proposed (Vasyliunas, AGY, 1968) to explain the energy dependence of the inner edge of the plasma sheet. In this case, the inner edge of the plasma sheet is not the Alfvén layer but the zone where ionospheric electrons with thermal energies cool off the incoming plasma sheet particles. The basic difference between this concept and the Alfvén layer concept is that Vasyliunas relies upon maintaining a potential difference along field lines, whereas Alfvén's concept relies upon maintaining potential differences across field lines. Indeed, as pointed out in Section VI-F, the potential difference resulting from the precipitation of a net negative charge will push trapped electrons to mirror at smaller values of B_m while pulling trapped protons earthward to larger values of B_m . This necessarily produces a density gradient along the field lines near the mirror points. However, this polarization is accomplished without changing the equatorial pitch angles so that the existence of an equatorial pitch-angle diffusion process will not necessarily result in the precipitation of a net charge.

VII. CONCLUSION.

Many auroral theories implicitly assume that the geomagnetic field has a particular configuration. Specifically, the auroral zone was assumed to lie on field lines which went to the neutral points, the surface of the magnetosphere, or to the neutral sheet in the tail. In the first self-consistent calculation of the geomagnetic field (Mead and Beard, 1964; Mead, 1964) the surface latitude of the neutral-point field line was 83° (Figure 14). This latitude is 5 to 8° above the latitude of the dayside auroral oval (Figures 3 and 4) and is extremely insensitive to the size of the magnetosphere. Recognizing this discrepancy Dessler and Juday (1965) proposed that the field of the quiet-day ring current would lower the surface latitude of the neutral-point field line to the latitude of the dayside auroral oval.

The quiet-day ring current has been deduced from the motion of observed plasmas. (See Section III-A) These plasmas (Figure 5) are assumed to be symmetric about the earth and moving in a dipolar magnetic field. Electric field drifts have been ignored since at the median energy of the low-energy protons, ~ 25 kev, the gradient drift

dominates any $E \times B$ drifts. The equatorial field of the quiet-day ring current (Figure 7) produces a 41% decrease at the earth's surface and a maximum decrease of 58% at $3.5 R_E$. The ring-current field changes sign at $9 R_E$ and enhances the dipole field by 8 to 10% between 10 and $11.5 R_E$. The sum of the dipole field and quiet-day ring-current field is shown in Figure 8.

The field of the quiet-day ring current is consistent with satellite observations (Mead and Cahill, 1967). (See Figure 9.) The net external field caused by the ring current and magnetopause currents is shown to be consistent with the external field statistically derived from ground based observations (Cain, 1966). The quiet-day ring current has a total magnetic moment of $.26 M_E$. Between 10 and $12 R_E$, the ring-current field enhances the equatorial dipole field by 25 to 35% while along the polar axis, the dipole field is enhanced by 15 to 17% over the same radial region. Using this field, an evaluation of the pressure balance between the solar wind and the geomagnetic field has shown that the proton number density of the quiet-day solar wind is greater than 5 p/cm^3 and averages between 8 and 10 p/cm^3 (Schild, 1968). This conclusion is in direct disagreement with experimental

observations using curved plate analyzers but is consistent with Faraday cup observations.

Using Mead's computer programs, with some basic alterations (Section IV), the shape of the magnetosphere and the configuration of the geomagnetic field have been calculated (Section V-A). The dipolar aspect of the ring current is responsible for a 26% increase in the earth's magnetic moment and in the magnetospheric surface-current field. The increase of the earth's magnetic moment by the dipolar aspect is not expected to change the surface latitude of the neutral-point field line since this latitude is insensitive to changes in the scale of the magnetosphere (Mead, 1964) (or equivalently to an increase in the earth's magnetic moment). The non-dipolar aspect of the ring current alters the dipolar aspect by less than 10% at $10 R_E$, a $\pm 2\%$ change in the dipole field. The absence of a change in the magnetospheric configuration produced by the quiet-day ring current (Figures 20 and 21) is consistent with a $\pm 2\%$ perturbation. The magnetospheric plasmas increase the equatorial crossing radius of a given field line (defined by a fixed latitude at the earth's surface) by up to 12% in the noon-meridian plane, i.e., a $1 R_E$ increase at $8 R_E$. However, the

surface latitude of the neutral-point field lines is insensitive to the presence of a quiet-day ring current.

A realistic model of the tail currents has been proposed and evaluated (Section II-B). This quadrasheet model (Figure 10) simulates the confinement of the tail currents to the surface of the magnetosphere. This magnetospheric model has four adjustable parameters which have been calibrated against observational data (Section V-C). This model is quite independent of three of the parameters: the subsolar extent of the magnetosphere R_{SS} , the radius of the geomagnetic tail R_t , and the distance to the inner edge of the tail currents R_I . The first two of these parameters R_{SS} and R_t have been extensively observed and are well known. Although the third parameter R_I has not been directly observed, it was adjusted to simulate the effect of the plasmas on the nightside of the magnetosphere. The model is fairly sensitive to the fourth parameter, the tail field B_t . However, the strength of the tail field has been extensively observed, and the median value of the field near $30 R_E$ has been utilized. On this basis, the model has been calibrated to $R_{SS} = 10.94 R_E$, $R_t = 20 R_E$, $R_I = 12 R_E$, and $B_t = 15\%$. The resultant geomagnetic configuration is illustrated in Figures 33 - 36.

This model predicts that the auroral oval does not map onto either the surface of the magnetosphere or onto the neutral sheet. During magnetically quiet times, the field lines which intersect the auroral oval (Figure 4) intersect the equatorial plane along the boundary of a quasi-circular region with a radius of about $10 R_E$ (Figure 40). The plasma sheet extending into the geomagnetic tail (Bame et al., 1967) has been observed by Vasyliunas (1968) and Freeman et al. (1967) to have a sharp inner edge. The inner edge of this plasma sheet (Figure 47) appears to be coincident with magnetic field lines that map onto the auroral oval.

It has been proposed that an Alfvén layer will form in the magnetosphere (Freeman, 1968). The Alfvén layer is the region of net charge on the boundary of the forbidden region that tends to develop when the tail plasma is convected into the earth's dipole field (Dessler, personal communication). It is argued that the Alfvén layer accounts for the location and magnitude of the field-aligned currents (that produce the transverse magnetic disturbances observed by satellites at auroral latitudes), as well as the location and energy dependence of the inner edge of the plasma sheet. The thickness of the Alfvén layer is shown to correspond to the width of the

zone of transverse magnetic disturbances. The field-aligned current necessary to neutralize the Alfvén layer is calculated to be about 10^6 amps, which is sufficient to produce transverse magnetic disturbances of about a 100%. The location of the Alfvén layer is shown to be consistent with the size of the forbidden region for a convection field of 1 to 2 kv/ R_E . The energy dependence of particles through the Alfvén layer is found to be caused by the thermal particles which carry a portion of the field-aligned neutralization current. The low energy cutoff in the auroral flux spectrum observed by Westerlund is explained as the result of Coulomb collisions with the ionosphere.

The capability to explain both the magnitude and location of the transverse magnetic disturbances provides strong evidence that the inner edge of the plasma sheet does map onto the auroral oval as predicted by this model of the magnetosphere.

APPENDIX

The Schmidt Normalized Polynomials

The relation between the ordinary Associated Legendre polynomials $P_{n,m}$; the Laplace-Gauss functions $P^{n,m}$; and the Schmidt normalized Legendre polynomials P_n^m has been discussed by Chapman and Bartels (1962). The following references to page and formula numbers refer to the above reference.

The ordinary Associated Legendre polynomials are defined by: $P_{n,n} = (2n)! \sin^n(\theta) / (2^n n!)$, $P_{0,0} = 1$ (p. 610, eq. 10). By using the recursion relation: $(2n+1) \cos \theta P_{n,m} + (n-m+1) P_{n+1,m} + (n+m) P_{n-1,m}$ (p. 623, eq. 51aa), one can solve for $P_{n,m}$ where:

$$P_{n,m} = \left[\frac{2n-1}{n-m} \right] \cos \theta P_{n-1,m} - \left[\frac{n+m-1}{n-m} \right] P_{n-2,m} \quad \text{for } m < n$$

$$P_{n,n} = (2n-1) \sin \theta P_{n-1,n-1} \quad \text{for } m=n$$

The Schmidt normalized polynomials P_n^m are related to the Associated Legendre polynomials $P_{n,m}$ by

$$P_n^m = \sqrt{2(n-m)! / \delta_m (n+m)!} P_{n,m}$$

(p. 611, eq. 19 and 20) where δ_m is 1 unless m equals 0, whereupon $\delta_0 = 2$.

The Schmidt coefficients, defined by

$$\text{Schmidt}(n,m) = P_n^m / P_{n,m}$$

are developed by using $\text{Schmidt}(0,0) = 1$, and

$$\text{Schmidt}(n,0) = \text{Schmidt}(n-1,0)$$

$$\frac{\text{Schmidt}(n,m)}{\text{Schmidt}(n,m-1)} = \sqrt{\frac{(\partial_{m-1} / \partial_m)}{(n-m+1)(n+m)}}$$

Several auxiliary functions were introduced in DANLSB to speed computation: $\text{CONST1}(n,m) = (2n-1)/(n+m)$; $\text{CONST2}(n,m) = -(n+m-1)/(n-m)$; $\text{CONST3}(n) = (2n-1)$; and $\text{DELTA} = \partial_{m-1} / \partial_m$. Fortran indices, NP and MP, were utilized where $\text{NP} = n+1$ and $\text{MP} = m+1$.

In order to fit the surface-current field near the neutral points, an angular resolution of 5° is desirable. This requires high-order coefficients. For example, P_7^0 requires 15° in theta to go from 1 to 0, yet is independent of phi. At the other extreme P_7^7 requires 90° in theta to go from 1 to 0, yet requires only about 13° in phi for the same excursion. For this reason, the surface current fields have been fit through the tenth order in n.

Acknowledgments

It is a pleasure to acknowledge the guidance provided by Dr. A.J. Dessler. This guidance has been invaluable in determining what constitutes creative research. The discussions with Drs. L.D. Kavanagh, J.L. Burch, L.H. Westerlund and with R. E. LaQuey have been very instructive. I am deeply grateful to my wife Sandy for plotting the data, for typing this thesis and for providing encouragement and support. I would also like to thank Rita Cary and the graphics section of the Space Science Department for drawing the figures.

This work was supported in part by the U. S. Air Force Cambridge Research Laboratories under contract AF19(628)-3858.

REFERENCES

- Akasofu, S.-I., The auroral oval, the auroral substorm and their relations with the internal structure of the magnetosphere, Planet. Space Sci., 14, 587-595, 1966.
- Akasofu, S.-I., and S. Chapman, The ring current, geomagnetic disturbance, and the Van Allen radiation belts, J. Geophys. Res., 66, 1321-1350, 1961.
- Akasofu, S.-I., and S. Chapman, Corrections to papers concerning magnetic effects of model ring currents, J. Geophys. Res., 72, 445-446, 1967.
- Alfvén, H., Cosmical Electrodynamics, Oxford Press, London, 1950.
- Alfvén, H., and C. G. Falthammer, Cosmic Electrodynamics, 2nd ed., Oxford Press, London, 1963.
- Alfvén, H., Theory of magnetic storms and of the aurorae, I., Kunql. Svenska Vetenskapsakademiens Handlingar, Stockholm, III, 18 (3), 1939.
- Alfvén, H., Theory of magnetic storms and of the aurorae, II and III, Kunql. Svenska Vetenskapsakademiens Handlingar, Stockholm, III, 18 (9), 1940.
- Alfvén, H., Some properties of magnetospheric neutral surfaces, Dept. of Space Science, Rice Univ., Houston, Texas, March 1968. Submitted for publication in the J. Geophys. Res., 1968.
- Annals of the International Geophysical Year, vol. 20, Pergamon Press, N. Y., 1962.
- Axford, W. I., The interaction between the solar wind and the earth's magnetosphere, J. Geophys. Res., 67, 3791-3796, 1962.
- Axford, W. I., Viscous interaction between the solar wind and the earth's magnetosphere, Planet. Space Sci., 12, 45-54, 1964.

- Axford, W. I., and C. O. Hines, Unifying theory of high latitude geophysical phenomena and geomagnetic storms, Canadian J. of Phys., 39, 1433-1464, 1961.
- Axford, W. I., H. E. Petschek, and G. L. Siscoe, Tail of the magnetosphere, J. of Geophys. Res., 70, 1231-1236, 1965.
- Bame, S. J., J. R. Asbridge, H. E. Felthouser, E. W. Hones, and I. B. Strong, Characteristics of the plasma sheet in the earth's magnetotail, J. Geophys. Res., 72, 113-129, 1967.
- Bates, H. F., Latitude of the dayside aurora, J. Geophys. Res., 71, 3629-3633, 1966.
- Beard, D. B., The solar wind geomagnetic field boundary, Reviews of Geophys., 2, 335-365, 1964.
- Beard, D. B., and E. B. Jenkins, The magnetic effects of magnetosphere surface currents, J. Geophys. Res., 67, 3361-3367, 1962.
- Behannon, K. W., Mapping of the earth's bow shock and magnetic tail by Explorer 33, J. Geophys. Res., 73, 907-930, 1968.
- Behannon, K. W., and N. F. Ness, Magnetic storms in the earth's magnetic tail, J. Geophys. Res., 71, 2327-2351, 1966.
- Birkeland, Kr., The Norwegian Aurora Polaris Expedition, 1902-3. Vol. 1, On the Cause of Magnetic Storms and the Origin of Terrestrial Magnetism, First Section, H. Aschehoug and Co., Christiania, 1908.
- Block, L. R., On the distribution of electric fields in the magnetosphere, J. Geophys. Res., 71, 855-864, 1966.
- Boström, R., A model of the auroral electrojets, J. Geophys. Res., 69, 4983-4999, 1964.
- Boström, R., Auroral electric fields, in Aurora and Airglow, ed. by Billy M. McCormac, pp. 293-303, Reinhold Publishing Corporation, 1967.

- Brice, N. M., Bulk motion of the magnetosphere, J. Geophys. Res., 72, 5193-5211, 1967.
- Cain, J. C., Models of the earth's magnetic field, in Radiation Trapped in the Earth's Magnetic Field, ed. by Billy M. McCormac, pp. 7-25, D. Reidel Publishing Company, Dordrecht-Holland, 1966.
- Cahill, L. J., Jr., Inflation of the magnetosphere near 8 earth radii in the dark hemisphere, Space Res., 6, 662-678, 1966.
- Chapman, S., and J. Bartels, Geomagnetism, Corrected edition, Oxford Press, N. Y., 1962.
- Chapman, S., and V. C. Ferraro, A new theory of magnetic storms, Terrestrial Magnetism Atmospheric Electricity, 36, 77-97, 171-186, 1931; 37, 147-156, 421-429, 1932; 38, 79-96, 1933.
- Cummings, W. D., and A. J. Dessler, Field-aligned currents in the magnetosphere, J. Geophys. Res., 72, 1007-1013, 1967.
- Davis, L. R., and J. M. Williamson, Low energy trapped protons, Space Res., 3, 365-375, 1963.
- Davis, L. R., and J. M. Williamson, Outer zone protons, in Radiation Trapped in the Earth's Magnetic Field, ed. by Billy M. McCormac, pp. 215-230, D. Reidel Publishing Company, Dordrecht-Holland, 1966.
- Dessler, A. J., Further comments on stability of interface between solar wind and geomagnetic field, J. Geophys. Res., 67, 4892-4894, 1962.
- Dessler, A. J., Length of magnetospheric tail, J. Geophys. Res., 69, 3913-3918, 1964.
- Dessler, A. J., Magnetic merging in the magnetospheric tail, J. Geophys. Res., 73, 209-214, 1968.
- Dessler, A. J., and R. D. Juday, Configuration of auroral radiation in space, Planet. Space Sci., 13, 63-72, 1965.

- Dessler, A. J., and F. C. Michel, Magnetospheric models, in Radiation Trapped in the Earth's Magnetic Field, ed. by Billy M. McCormac, pp. 447-456, D. Reidel Publishing Company, Dordrecht-Holland, 1966.
- Dungey, J. W., Interplanetary magnetic field and the auroral zones, Physical Rev. Letters, 6, 47-48, 1961.
- Dungey, J. W., The theory of the quiet magnetosphere, in Solar-Terrestrial Physics, ed. by J. W. King and W. S. Newman, pp. 91-106, Academic Press, N. Y., 1967.
- Farley, D. T., A plasma instability resulting in field-aligned irregularities in the ionosphere, J. Geophys. Res., 68, 6083-6097, 1963.
- Feldstein, Y. I., Peculiarities in the auroral distribution and magnetic disturbances distribution in high latitudes caused by the asymmetrical form of the magnetosphere, Planet. Space Sci., 14, 121-130, 1966.
- Feldstein, Y. I., and G. V. Starkov, Dynamics of auroral belt and polar geomagnetic disturbances, Planet. Space Sci., 15, 209-229, 1967.
- Ferraro, V. C. A., On the theory of the first phase of a geomagnetic storm; a new illustrative calculation based on an idealised (plane not cylindrical) model field distribution, J. Geophys. Res., 57, 15-49, 1952.
- Frank, L. A., On the local-time dependence of outer radiation zone electron ($E > 1.6$ Mev) intensities near the magnetic equator, J. Geophys. Res., 70, 4131-4138, 1965.
- Frank, L. A., Observations of magnetospheric boundary phenomena, in Radiation Trapped in the Earth's Magnetic Field, ed. by Billy M. McCormac, pp. 422-446, D. Reidel Publishing Company, Dordrecht-Holland, 1966.
- Frank, L. A., Initial observations of low-energy electrons in the earth's magnetosphere with OGO-3, J. Geophys. Res., 72, 185-195, 1967a.

- Frank, L. A., Several observations of low-energy protons and electrons in the earth's magnetosphere with OGO-3, J. Geophys. Res., 72, 1905-1916, 1967b.
- Frank, L. A., Recent observations of low-energy charged particles in the earth's magnetosphere, Dept. of Physics and Astronomy, Univ. of Iowa, Iowa City, Iowa, July 1967c (Unpublished).
- Freeman, J. W., Jr., The morphology of the electron distribution in the outer radiation zone and near the magnetospheric boundary as observed by Explorer 12, J. Geophys. Res., 69, 1691-1723, 1964.
- Freeman, J. W., Jr., A source for field-aligned currents at auroral latitudes, Dept. of Space Science, Rice Univ., Houston, Texas, March 13, 1968 (Unpublished).
- Freeman, J. W., Jr., and J. J. Maguire, Gross local-time particle asymmetries at the synchronous orbit altitude, J. Geophys. Res., 72, 5257-5264, 1967.
- Freeman, J. W., Jr., J. J. Maguire, and C. Warren, Anomalous particle fluxes at the synchronous orbit -- January 14, 1967. Submitted for publication in the J. Geophys. Res., 1968.
- Freeman, J. W., J. A. Van Allen, and L. J. Cahill, Explorer 12 observations of the magnetospheric boundary and the associated solar plasma on September 13, 1961, J. Geophys. Res., 68, 2121-2130, 1963.
- Gosling, J. R., J. R. Asbridge, S. J. Bame, and I. B. Strong, Vela 2 measurements of the magnetopause and bow shock position, J. Geophys. Res., 72, 101-112, 1967.
- Helmer, J. C., Theory of forbidden zones in the flow of a magnetized plasma, Phys. Fluids, 6, 723-728, 1963.
- Heppner, J. P., M. Suguira, T. L. Skillman, B. G. Ledley, and M. Campbell, OGO-A magnetic field observations, J. Geophys. Res., 72, 5417-5471, 1967.

- Hewson-Browne, R. C., and D. W. Windle, Chapman-Ferraro hollows for a system of line currents enveloped by a stratified corpuscular flux, J. Atmospheric and Terrestrial Phys., 28, 847-860, 1966.
- Hoffman, R. A., and P. A. Bracken, Magnetic effects of the quiet time proton belt, J. Geophys. Res., 70, 3541-3556, 1965.
- Hoffman, R. A., and P. A. Bracken, Higher-order ring currents and particle energy storage in the magnetosphere, J. Geophys. Res., 72, 6039-6049, 1967.
- Hoh, F. C., The tail of the magnetosphere and particle acceleration, in Radiation Trapped in the Earth's Magnetic Field, ed. by Billy M. McCormac, D. Reidel Publishing Company, Dordrecht-Holland, 1966.
- Hurley, J., Interaction of a streaming plasma with the magnetic field of a line current, Phys. of Fluids, 4, 109-111, 1961a.
- Hurley, J., Interaction of a streaming plasma with the magnetic field of a two-dimensional dipole, Phys. of Fluids, 4, 854-859, 1961b.
- Johnson, F. S., The gross character of the geomagnetic field in the solar wind, J. Geophys. Res., 65, 3049-3051, 1960.
- Johnson, F. S., ed., Satellite Environment Handbook, 2nd ed., Stanford Univ. Press, Stanford, Calif., 1965.
- Karlson, E. T., Streaming of a plasma through a magnetic dipole field, Phys. Fluids, 6, 708-722, 1963.
- Kavanagh, L. D., Jr., Predicted and observed displacements and energy changes of charged particles after distention of the magnetosphere by a symmetric ring current, Ph. D. thesis, Rice Univ., Houston, Texas, 1967.
- Kavanagh, L. D., Jr., J. W. Freeman, Jr., and A. J. Chen, Plasma flow in the magnetosphere, Dept. of Space Science, Rice Univ., Houston, Texas, 1968. Submitted for publication in the J. Geophys. Res., 1968.

- Kellogg, P. J., Flow of plasma around the earth, J. Geophys. Res., 67, 3805-3811, 1962.
- Lazarus, A. J., G. L. Siscoe, and N. F. Ness, Plasma and magnetic field observations during the magnetosphere passage of Pioneer 7, J. Geophys. Res., 73, 2399-2409, 1968.
- Lees, L., Interaction between the solar plasma wind and the geomagnetic cavity, Am. Inst. of Aeronautics and Astronautics, 2, 1576-1582, 1964.
- Lerche, I., Validity of the hydromagnetic approach in discussing instability of the magnetospheric boundary, J. Geophys. Res., 71, 2365-2371, 1966.
- Lerche, I., On the boundary layer between a warm, streaming plasma and a confined magnetic field, J. Geophys. Res., 72, 5295-5310, 1967.
- McCormac, B., ed., Radiation Trapped in the Earth's Magnetic Field, D. Reidel Publishing Company, Dordrecht-Holland, 1966.
- McDiarmid, I. B., and J. R. Burrow, Local time asymmetries in the high latitude boundary of the outer radiation zone for different electron energies, Division of Pure Physics, National Research Council of Canada, Ontario, Canada, 1967 (Unpublished).
- Mead, G. D., Deformation of the geomagnetic field by the solar wind, J. Geophys. Res., 69, 1181-1195, 1964.
- Mead, G. D., and D. B. Beard, Shape of the geomagnetic field solar wind boundary, J. Geophys. Res., 69, 1169-1179, 1964.
- Mead, G. D., and L. J. Cahill, Jr., Explorer 12 measurements of the distortion of the geomagnetic field by the solar wind, J. Geophys. Res., 72, 2737-2748, 1967.
- Mende, I. B., Experimental investigation of electric fields parallel to the magnetic field in the auroral ionosphere, J. Geophys. Res., 73, 991-997, 1968.
- Midgley, J., and L. Davis, Jr., Computation of the bounding surface of a dipole field in a plasma by a moment technique, J. Geophys. Res., 67, 499-504, 1962.

- Midgley, J., and L. Davis, Jr., Calculation by a moment technique of the perturbation of the geomagnetic field by the solar wind, J. Geophys. Res., 68, 5111-5123, 1963.
- Morgenau, H., and G. M. Murphy, Mathematics of Physics and Chemistry, D. Van Nostrand Company, Princeton, N.J., 1956.
- Ness, N. F., The earth's magnetic tail, J. Geophys. Res., 70, 2989-3005, 1965.
- Ness, N. F., Observations of the interaction of the solar wind with the geomagnetic field during quiet conditions, in Solar-Terrestrial Physics, ed. by J. W. King, and W. S. Newman, pp. 59-89, Academic Press, N. Y., 1967.
- Parker, E. N., Confinement of a magnetic field by a beam of ions, J. Geophys. Res., 72, 2315-2322, 1967.
- Roederer, J. G., On the adiabatic motion of energetic particles in a model magnetosphere, J. Geophys. Res., 72, 981-992, 1967.
- Rosenbluth, M., Infinite conductivity theory of the pinch, LASL Rep. LA-1850 (1954).
- Sckopke, N., A general relation between the energy of trapped particles and the disturbance field near the earth, J. Geophys. Res., 71, 3125-3130, 1966.
- Schild, M. A., Pressure balance between solar wind and magnetosphere, Dept. of Space Science, Rice Univ., Houston, Texas, March 1968. To be submitted for publication in the J. Geophys. Res., 1968.
- Sen, K., Stability of the magnetospheric boundary, Planet. Space Sci., 13, 131-141, 1965.
- Sharp, R. D., and R. G. Johnson, Some average properties of auroral electron precipitation as determined from satellite observations, J. Geophys. Res., 73, 969-990, 1968.
- Siscoe, G. L., and V. Formisano, A calibration of the magnetosphere, Paper presented at the 49th Annual meeting of the AGU, Washington, D. C., 1968.

- Slutz, R. J., The shape of the geomagnetic field boundary under uniform external pressure, J. Geophys. Res., 67, 505-513, 1962.
- Speiser, T. W., Auroral particles accelerated in the geomagnetic tail, in Aurora and Airglow, ed. by Billy M. McCormac, pp. 491-498, Reinhold Publishing Corporation, N. Y., 1967.
- Spitzer, L., Jr., Physics of Fully Ionized Gases, 2nd rev. ed., Interscience Publishers, N. Y., 1962.
- Spreiter, J. R., and A. Y. Alksne, On the effect of a ring current on the terminal shape of the geomagnetic field, J. Geophys. Res., 67, 2193-2205, 1962.
- Spreiter, J. R., and B. R. Briggs, Theoretical determination of the form of the boundary of the solar corpuscular stream produced by interaction with the magnetic dipole field of the earth, J. Geophys. Res., 67, 37-51, 1962.
- Störmer, C., The corpuscular theory of aurora borealis, in The Book of the Opening of Rice Institute, vol. 3, pp. 981-1035, de Vinne Press, N. Y., 1912.
- Swift, D. W., A mechanism for energizing electrons in the magnetosphere, J. Geophys. Res., 70, 3061-3073, 1965.
- Taylor, H. E., and E. W. Hones, Jr., Adiabatic motion of auroral particles in a model of the electric and magnetic fields surrounding the earth, J. Geophys. Res., 70, 3605-3628, 1965.
- Treffitz, E., Über die Kontraktion kreisförmiger Flüssigkeitsstrahlen, Z. Math. Phys., 69, 34, 1916.
- Vasyliunas, V. M., Mathematical model of plasma motions in the magnetosphere, Paper presented at the 49th Annual Meeting of the AGU, Washington, D. C., 1968.
- Vasyliunas, V. M., A survey of low energy electrons in the evening sector of the magnetosphere with OGO-1 and OGO-3, J. Geophys. Res., 73, 2839-2884, 1968.
- Weibel, E. S., On the confinement of a plasma by magnetostatic fields, Phys. Fluids, 2, 52-56, 1959.

- Westerlund, L. H., Rocket Bourne observation of the auroral energy spectra and their pitch-angle distribution, Ph.D. thesis, Rice Univ., Houston, Texas, 1968.
- Williams, D. J., and G. D. Mead, Nightside magnetosphere configuration as obtained from trapped electrons at 1100 kilometers, J. Geophys. Res., 70, 3017-3029, 1965.
- Zhigulev, V. N., On the phenomenon of magnetic detachment of the flow of a conducting medium, Soviet Phys. Doklady, 4, 514-516, 1959 (DAN 126, 521, 1959).
- Zhigulev, V. N., and E. A. Romishevskii, Concerning the interaction of currents flowing in a conducting medium with the earth's magnetic field, Soviet Phys. Doklady, 4, 859-862, 1959 (DAN 127, 1001, 1959).
- Zmuda, A. J., J. H. Martin, and F. T. Heuring, Transverse magnetic disturbances at 1100 kilometers in the auroral region, J. Geophys. Res., 71, 5033-5045, 1966.

FIGURE CAPTIONS

- Figure 1a. Magnetospheric model in which merging is negligible (See Dessler and Michel, 1966).
- Figure 1b. Magnetospheric model by Axford et al., (1965)
The neutral sheet is not really neutral but has a weak perpendicular field and a thickness much greater than an ion cyclotron radius.
- Figure 2. Geomagnetic configuration (Dessler, 1968)
similar to that of Axford et al. but having the neutral line located about $20 R_E$ behind the earth.
- Figure 3. Comparison of various high latitude boundaries versus local time (McDiarmid and Burrows, 1967).
- Figure 4. Location of the auroral oval versus Q , an auroral zone magnetic index (after Feldstein and Starkov, 1967).
- Figure 5. Radial distribution of plasma energy densities.
The parameters and functional forms used to fit these distributions are also shown.
- Figure 6. Proton differential flux spectrum at $L = 6$ (Frank, 1967b).
- Figure 7. Equatorial field of quiet-day ring current versus radial distance.
- Figure 8. Sum of ring-current field and dipole field versus equatorial distance.

- Figure 9. Comparison of the observed equatorial geomagnetic field near the subsolar axis with Mead's predicted geomagnetic field. Note the similarity between the difference and the quiet-day ring current field in Figure 7.
- Figure 10. The configuration of a realistic tail current. This quadra-sheet model simulates the flow of the tail currents along the surface of the magnetopause and across the neutral sheet.
- Figure 11. Truncated current-sheet model of the tail current which closes at infinity (Williams and Mead, 1965).
- Figure 12. Location of the magnetospheric boundary during the first three iterations with the quiet-day ring current field. The noon-midnight meridian cross section is shown above the midline, the equatorial trace is shown below the midline.
- Figure 13. Location of points where the spherical expansion coefficients were fit to the geomagnetic field.
- Figure 14. Mead's magnetospheric configuration in the noon-midnight meridian plane.
- Figure 15. Mead's magnetospheric configuration projected onto the equatorial plane.

- Figure 16. Geomagnetic configuration including the quiet-day ring current field in the noon-midnight meridian plane.
- Figure 17. Geomagnetic configuration including the quiet-day ring current field projected onto the equatorial plane.
- Figure 18. Equatorial intersection of lines of constant polar latitude.
- Figure 19. Equatorial contours of constant magnetic field strength.
- Figure 20. Comparison of the geomagnetic configuration including the quiet-day ring current field with Mead's magnetospheric configuration in the noon-midnight meridian plane.
- Figure 21. Comparison of the geomagnetic configuration including the quiet-day ring current field with Mead's magnetospheric configuration in the equatorial plane.
- Figure 22. Geomagnetic field configuration with a 30% tail field beyond $10 R_E$, in the noon-midnight meridian. (The quiet-day ring current field is included in all subsequent geomagnetic fields).
- Figure 23. Equatorial projection of geomagnetic field using a 30% tail field beyond $10 R_E$.

- Figure 24. Equatorial contour for lines of constant polar latitude using a 30% tail field beyond $10 R_E$.
- Figure 25. Polar intersection of field lines which are open beyond $20 R_E$, and of field lines which intersect the equator at $10 R_E$ using a 30% tail field beyond $10 R_E$.
- Figure 26. Geomagnetic field configuration in the noon-midnight meridian plane using a 30% tail field beyond $12 R_E$.
- Figure 27. Equatorial projection of the geomagnetic field using a 30% tail field beyond $12 R_E$.
- Figure 28. Polar intersection of field lines which are open beyond $20 R_E$, and of field lines which intersect the equatorial plane at $10 R_E$ using a tail field of 30% beyond $12 R_E$.
- Figure 29. Geomagnetic configuration in the noon-midnight meridian plane using a 15% tail field beyond $10 R_E$.
- Figure 30. Equatorial projection of the geomagnetic field using a 15% tail field beyond $10 R_E$.
- Figure 31. Equatorial contours of constant magnetic field using a tail field of 15% beyond $10 R_E$.

- Figure 32. Polar intersection of field lines which are open beyond $20 R_E$, and of field lines which intersect the equatorial plane at $10 R_E$ using a tail field of 15% beyond $10 R_E$.
- Figure 33. Geomagnetic configuration in the noon-midnight meridian plane using a 15% tail field beyond $12 R_E$.
- Figure 34. Equatorial projection of the geomagnetic field using a 15% tail field beyond $12 R_E$.
- Figure 35. Equatorial contours of constant polar latitude using a tail field of 15% beyond $12 R_E$.
- Figure 36. Polar intersection of field lines which are open beyond $20 R_E$, and of field lines which intersect the equatorial plane at $10 R_E$ using a tail field of 15% beyond $12 R_E$.
- Figure 37. Predicted equatorial geomagnetic field strength versus distance in the midnight meridian plane relative to the dipole field strength for various tail fields.
- Figure 38. Geomagnetic field configurations deduced from magnetic field measurements (See Frank, 1966).
- Figure 39. Equatorial mapping of ~~Frank~~ Waldstein's auroral oval (Figure 3) using a 15% tail field beyond $12 R_E$.

- Figure 40. Equatorial mapping the of the quiet-time ($Q \sim 0$) auroral oval (See Figure 4) using a tail field of 15% beyond $12 R_E$.
- Figure 41. Alfvén's concept of how the field-aligned current would discharge across the auroral zone (After Alfvén, 1939).
- Figure 42. Magnetospheric convection system proposed by Axford and Hines (1961), illustrating the formation of a forbidden region.
- Figure 43. Forbidden region for protons and electrons having the same magnetic moments, moving in a uniform electric field and a dipole magnetic field, neglecting the effect of charge separation.
- Figure 44. Expected flow of plasma sheet particles around the forbidden region in the equatorial plane.
- Figure 45. Configuration of the plasma sheet and the Alfvén layer in a meridian plane.
- Figure 46. The energy E_0 of the most probable flux, the number density N and the electron energy density U of electrons in the plasma sheet as a function of radial distance (Vasyliunas, 1968). The energy density U is given by $NE_0 \left[\frac{1.5\alpha}{(\alpha - 1.5)} \right]$ where α is the power-law exponent of the high energy tail.

- Figure 47. The location of the inner edge of the plasma sheet during both quiet and storm times (Vasyliunas, 1968).
- Figure 48. The charge-separation configuration deduced by Helmer, (1964) including inertial effects. In this case a net charge can form outside the forbidden regions.
- Figure 49. The predicted radial dependence of the peak energy for both protons and electrons on the dawn and dusk sides of the magnetosphere, neglecting corotation.
- Figure 50. The differential flux spectrum between .01ev and 10 kev. The thermal distribution is Maxwellian with a total electron density of 10^6 e/cm³ and a temperature of about 3000°K or ½ev.
- Figure 51. Differential flux spectra observed by Westerlund (1968) near local midnight. The rocket moves from L = 7 to L = 12 as time increases.

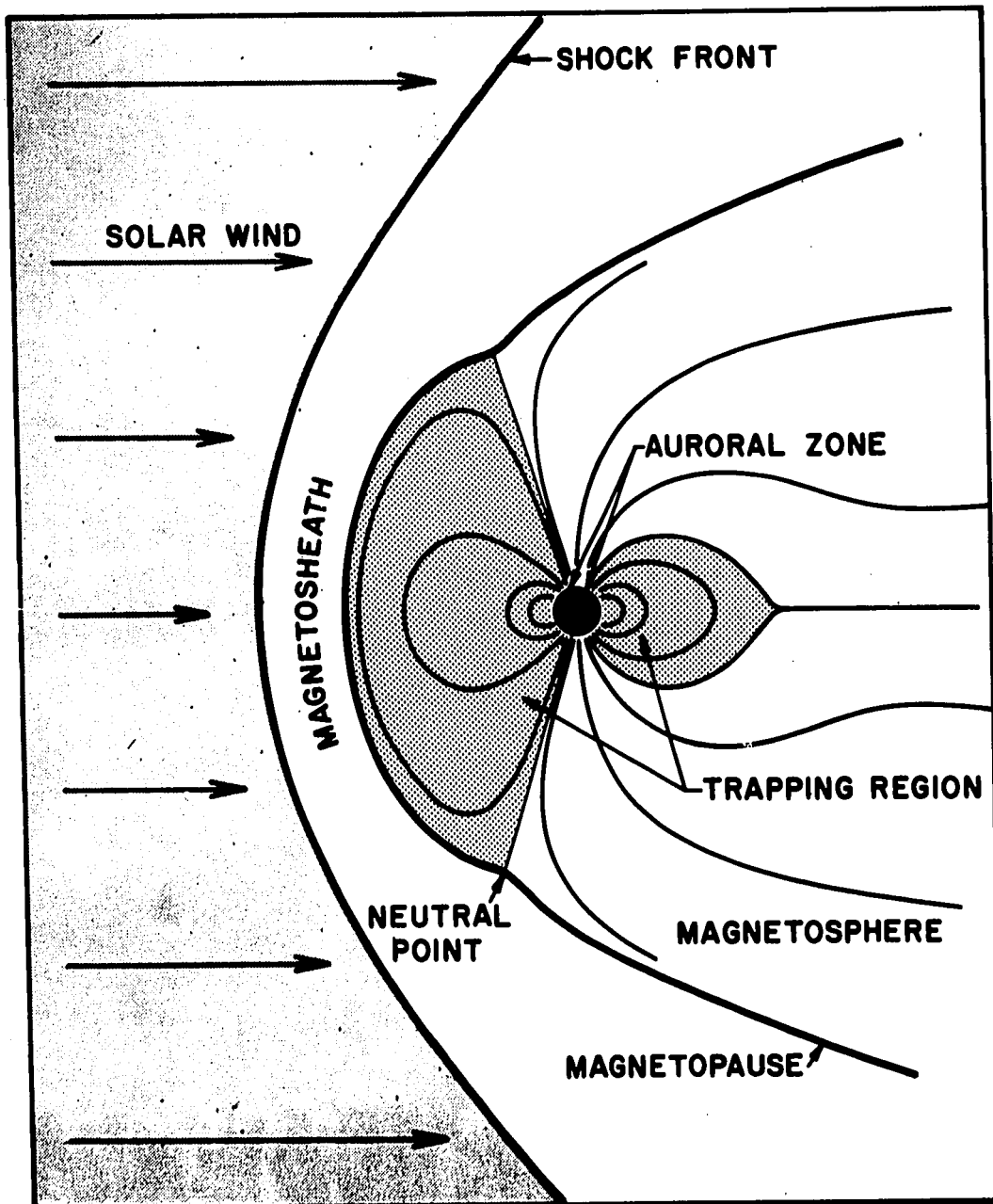


FIGURE 1a

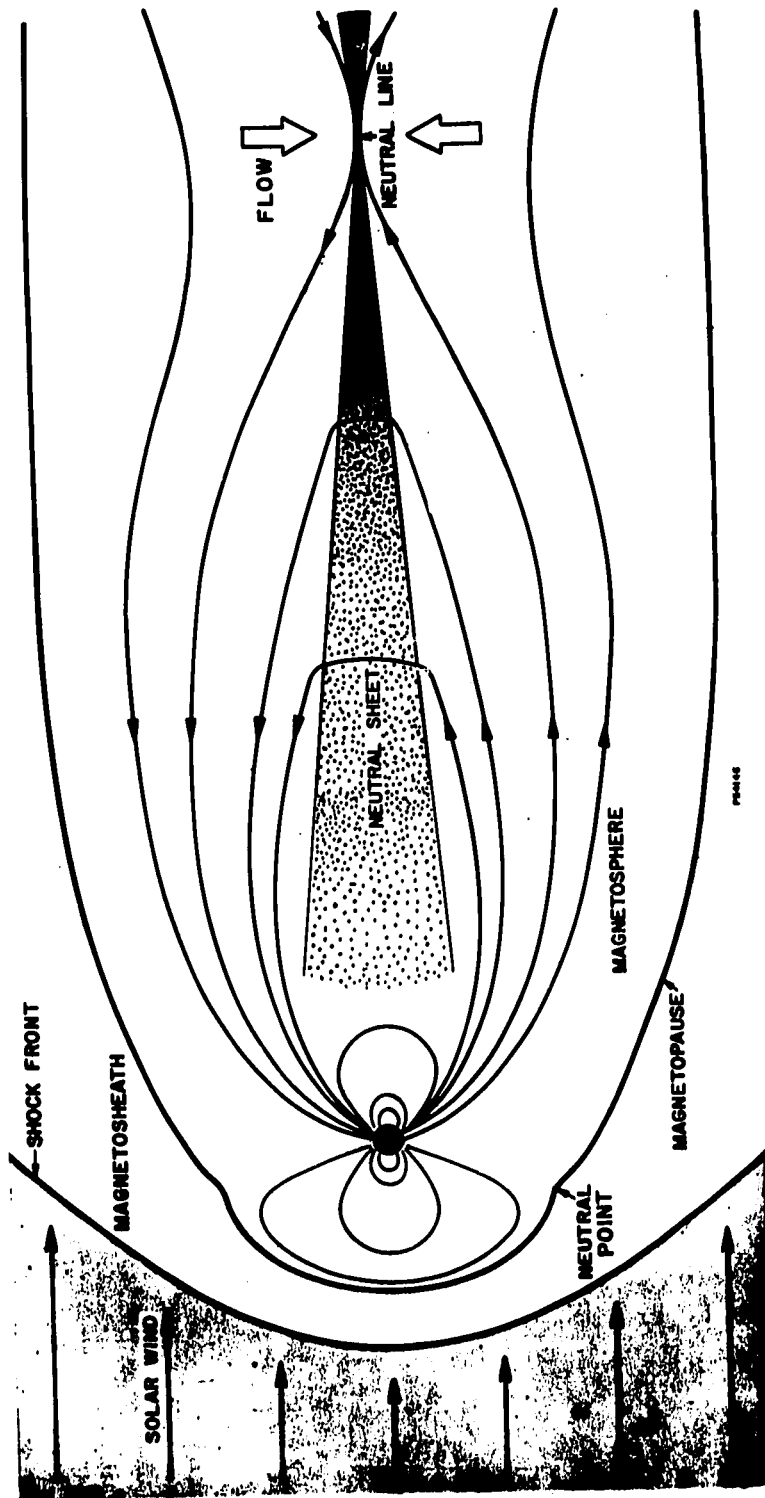
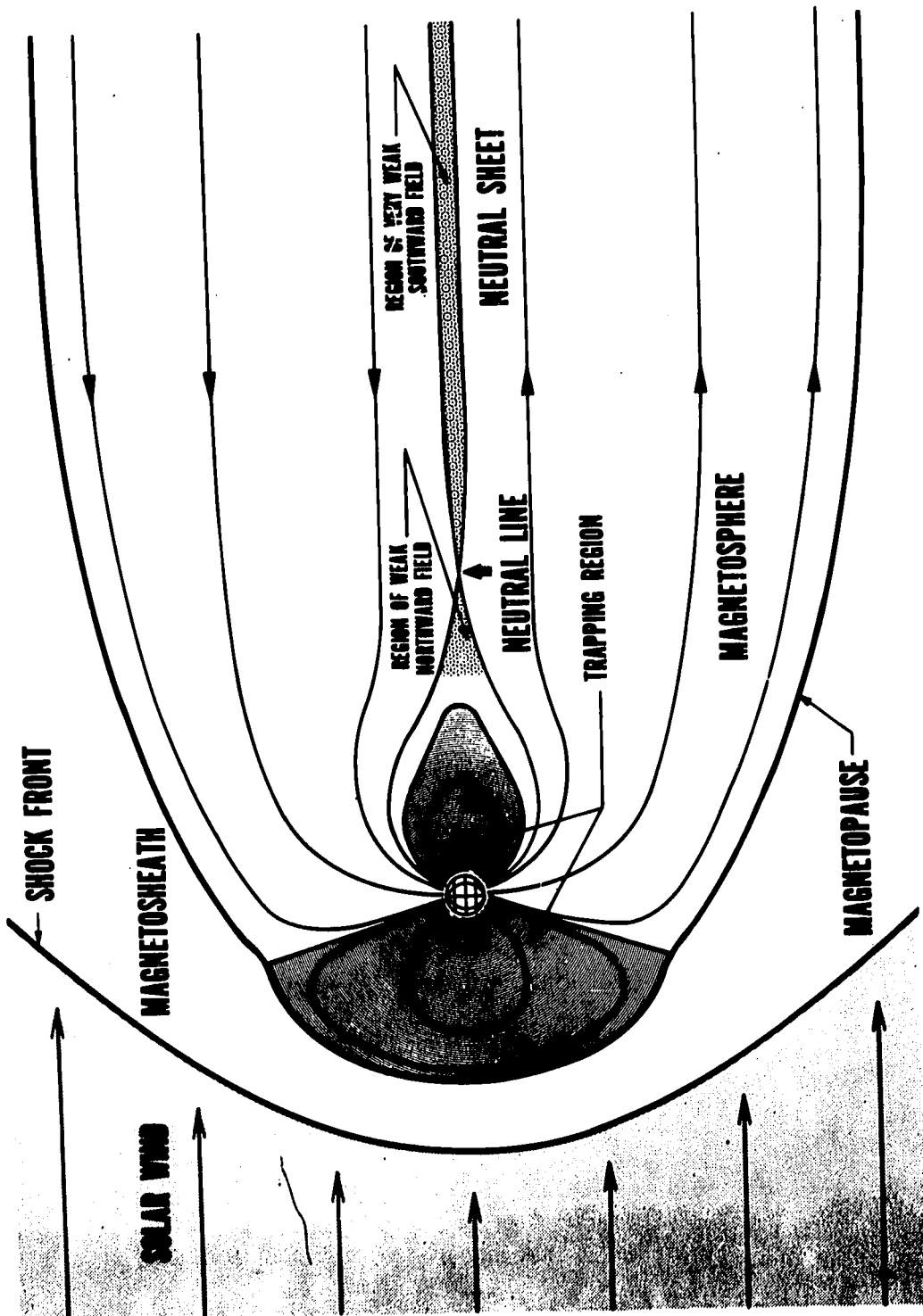


FIGURE 1b



201608

FIGURE 2

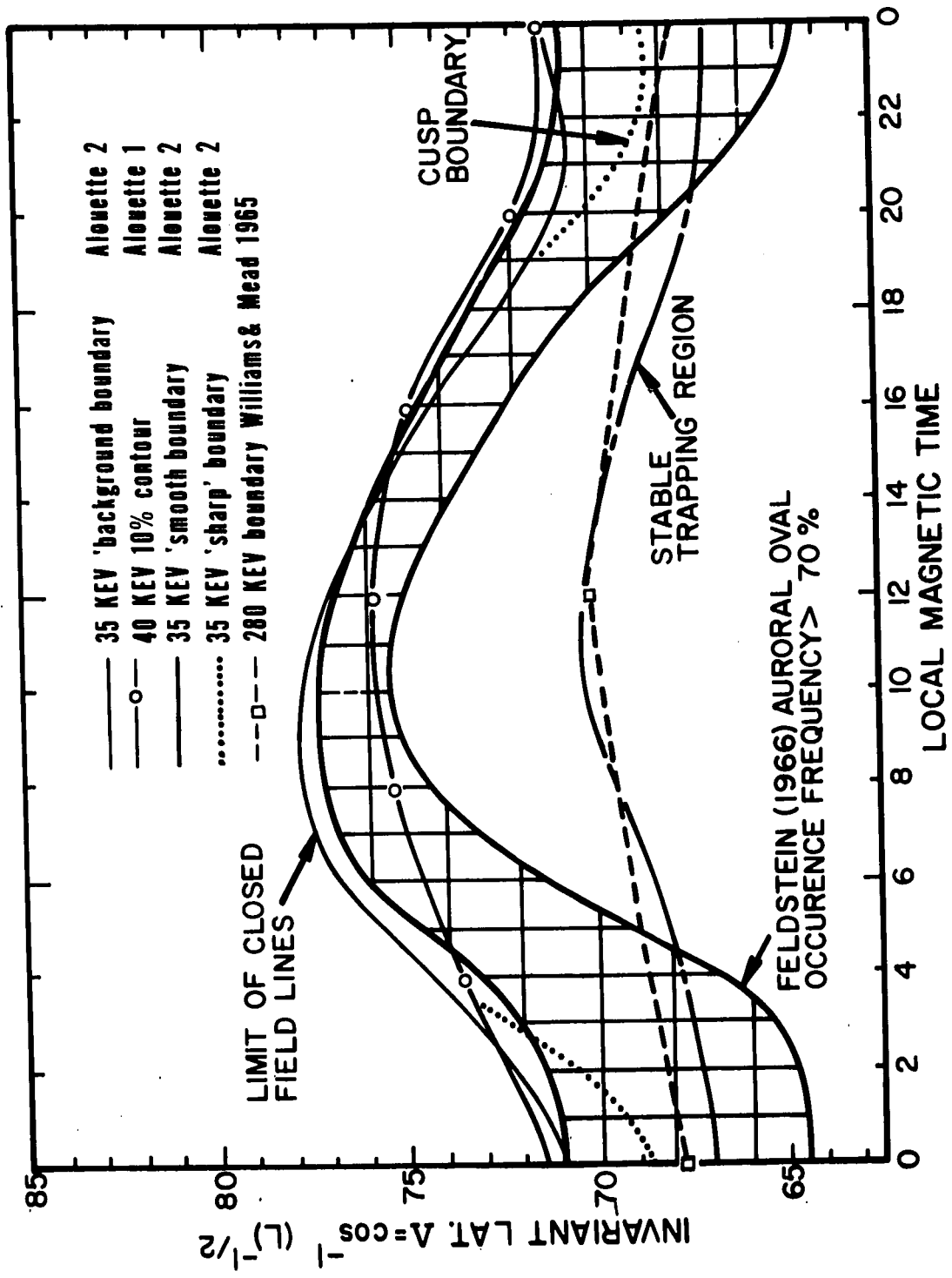


FIGURE 3

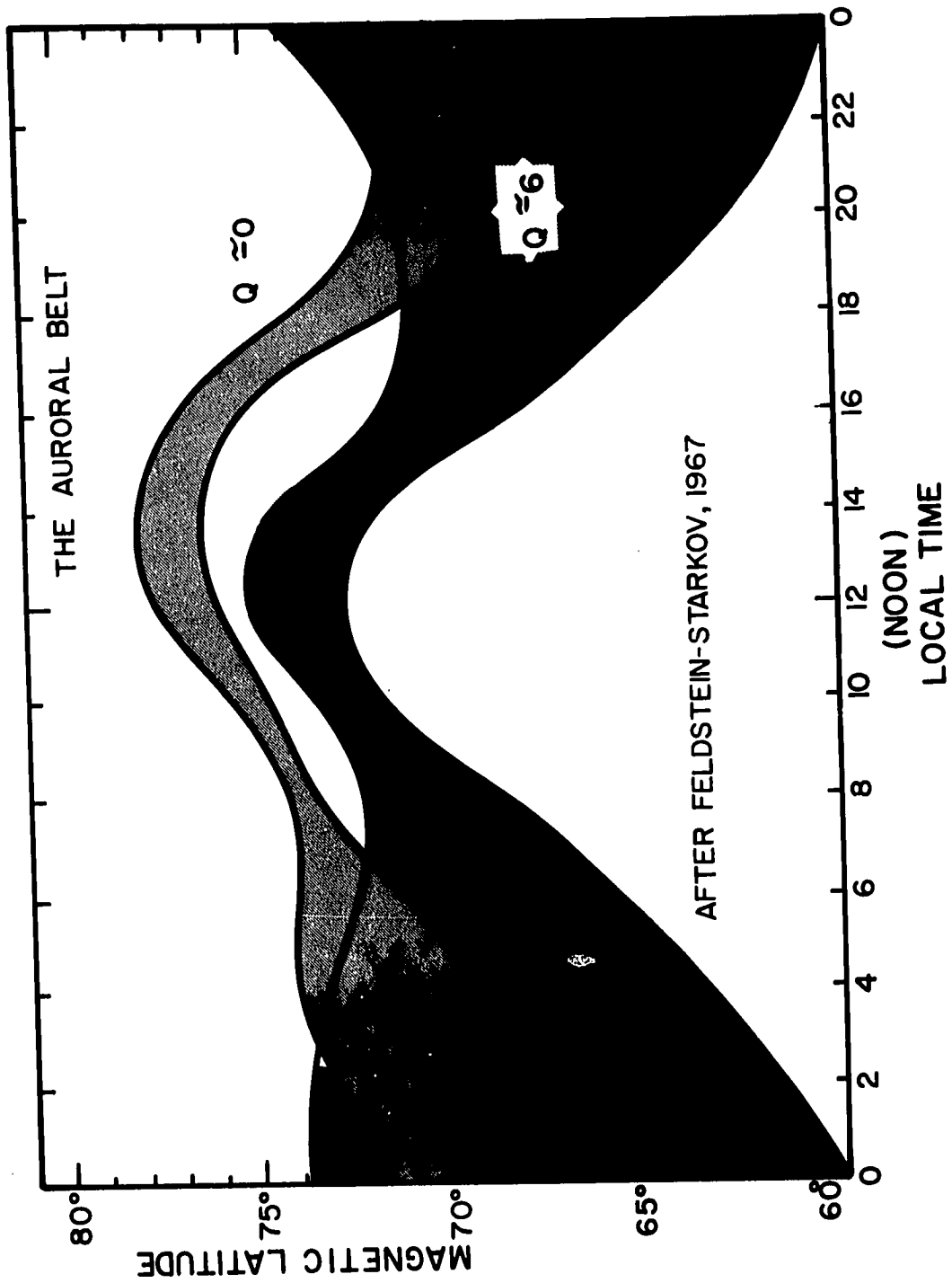


FIGURE 4

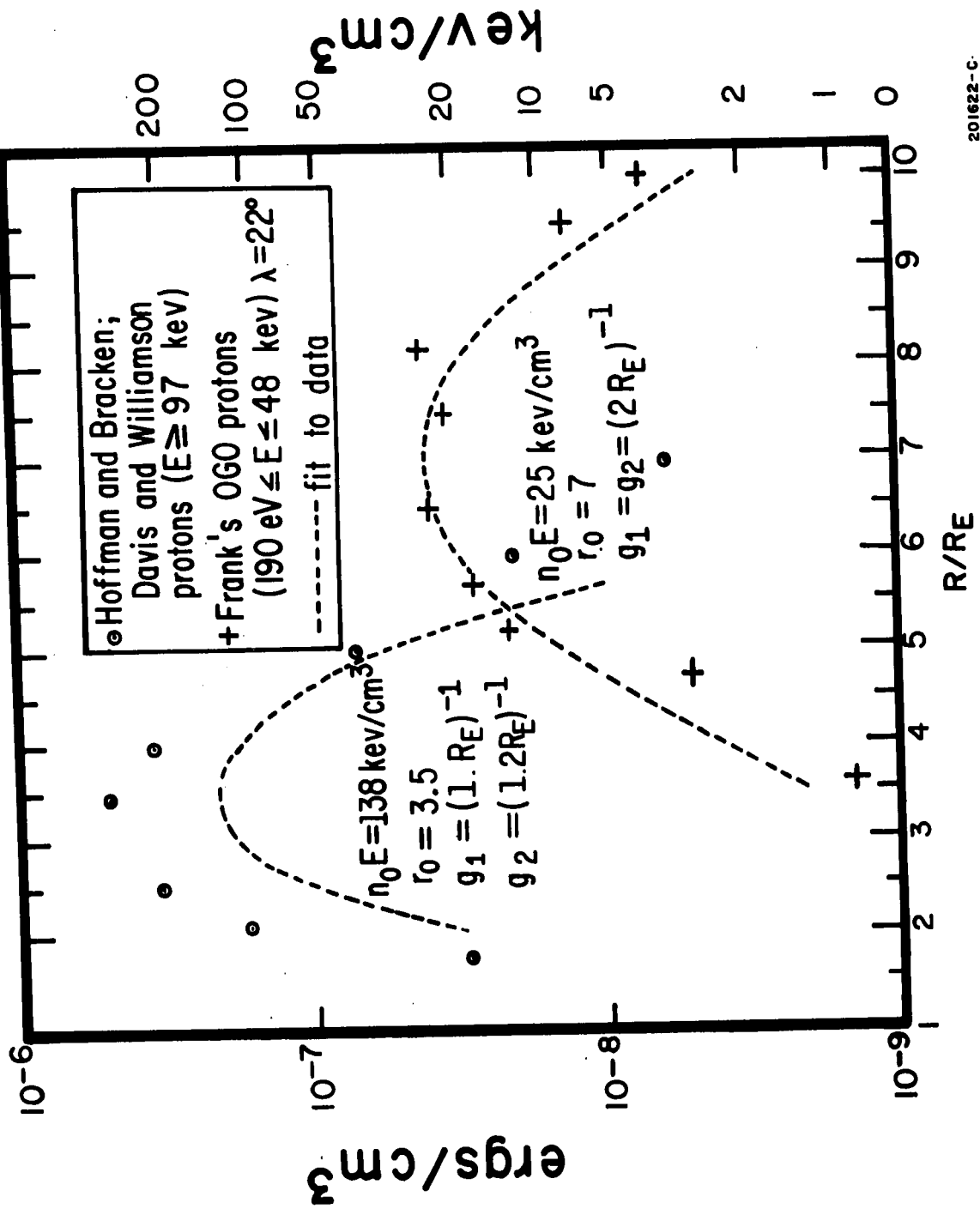


FIGURE 5

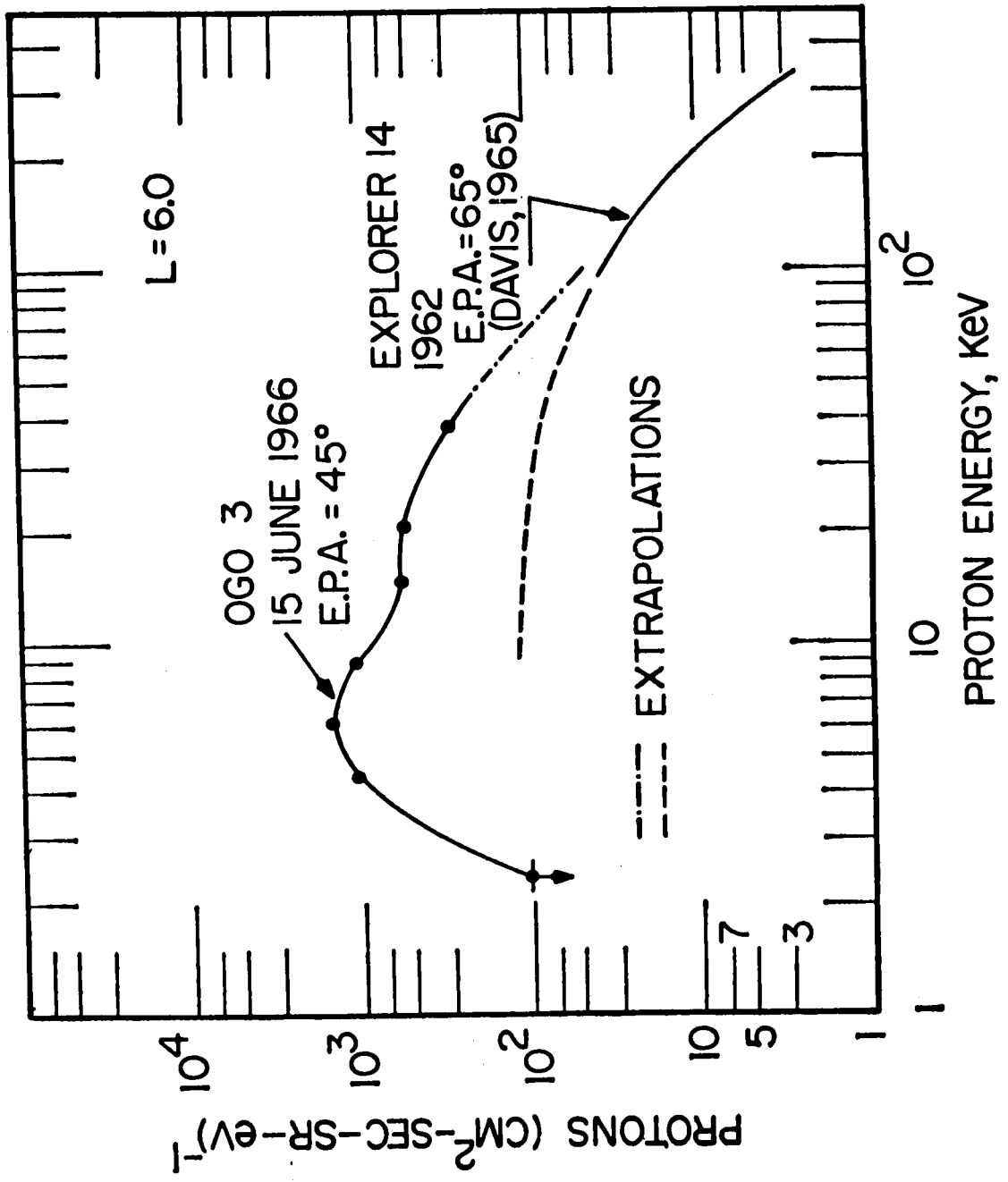


FIGURE 6

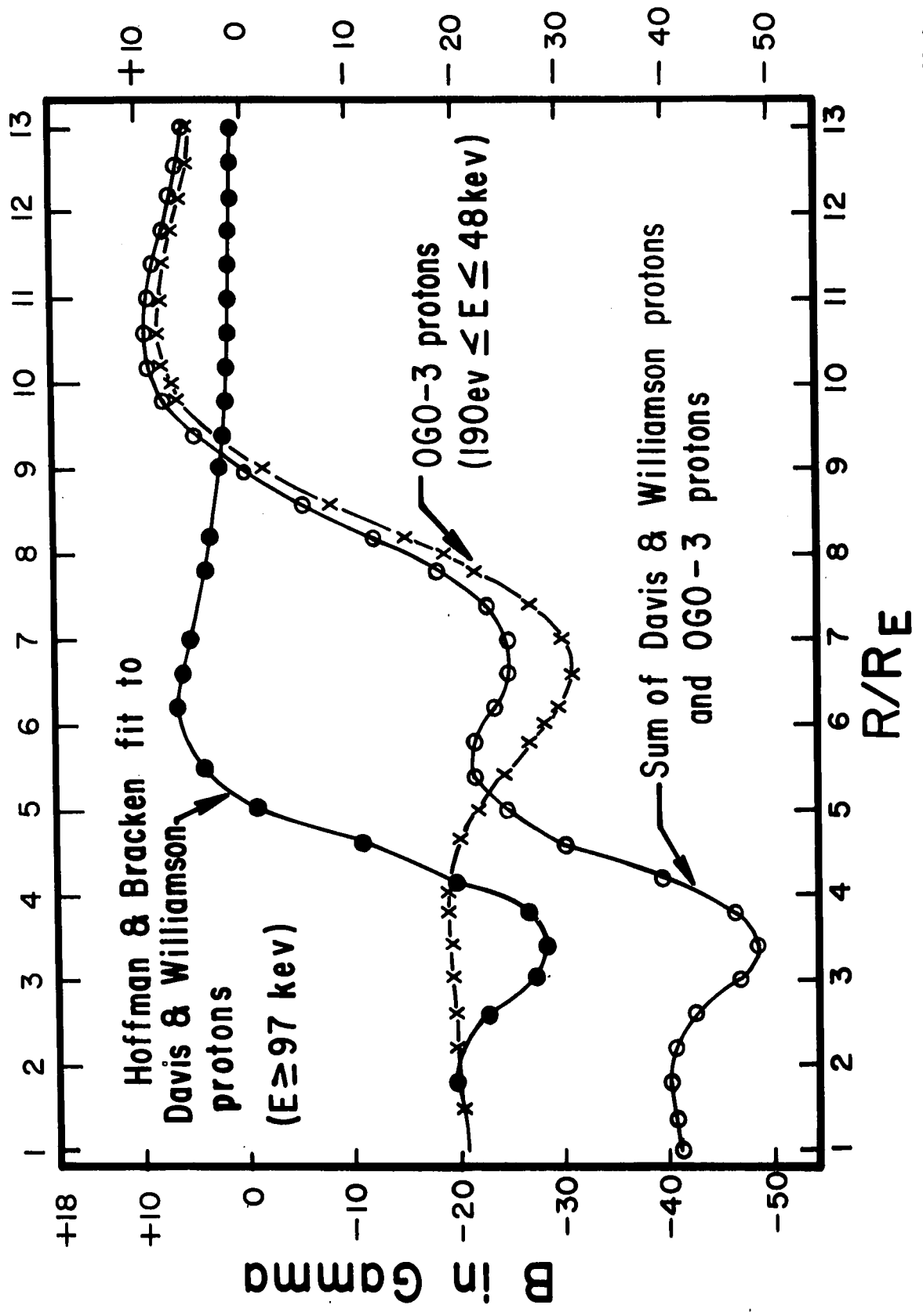


FIGURE 7

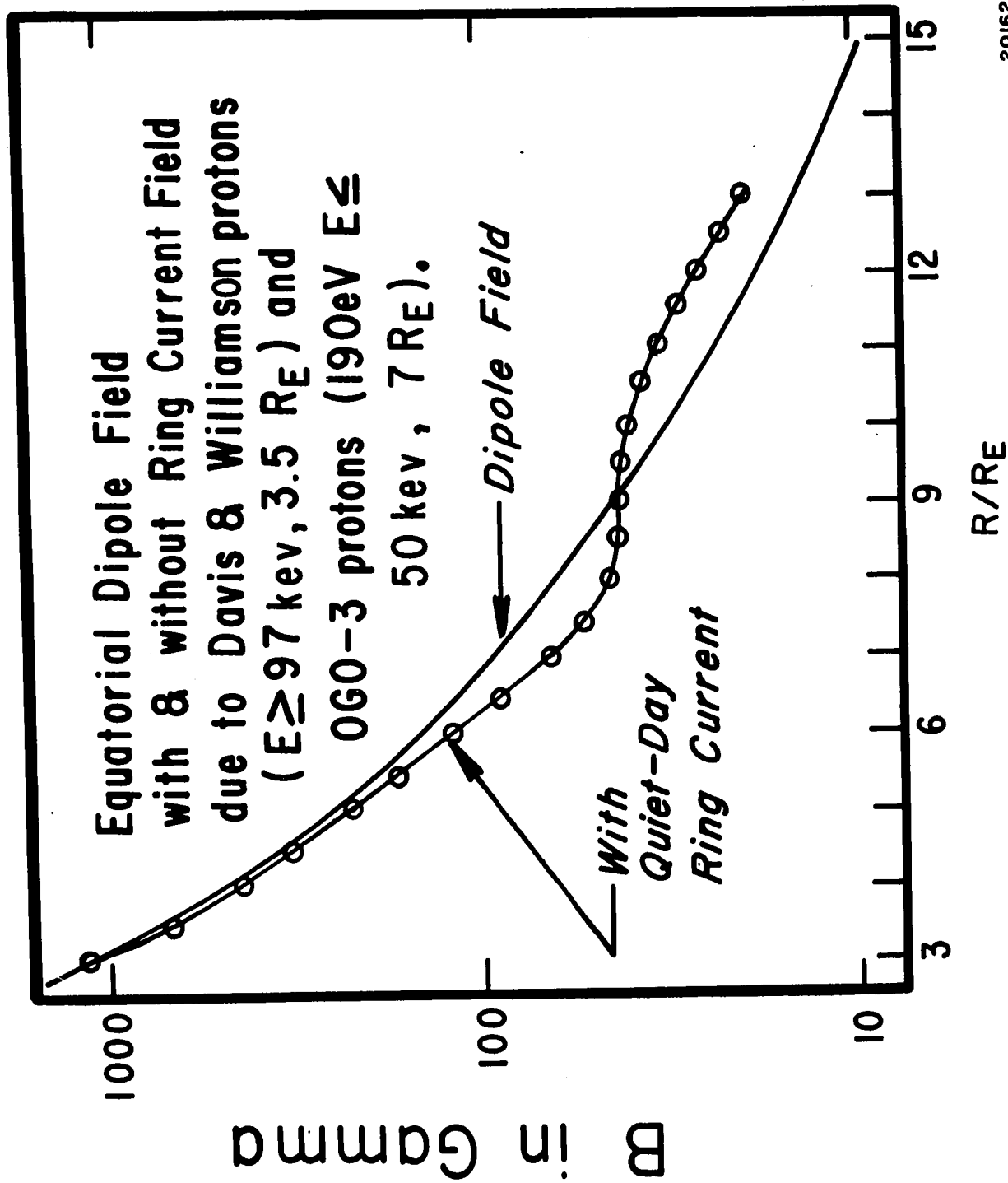


FIGURE 8

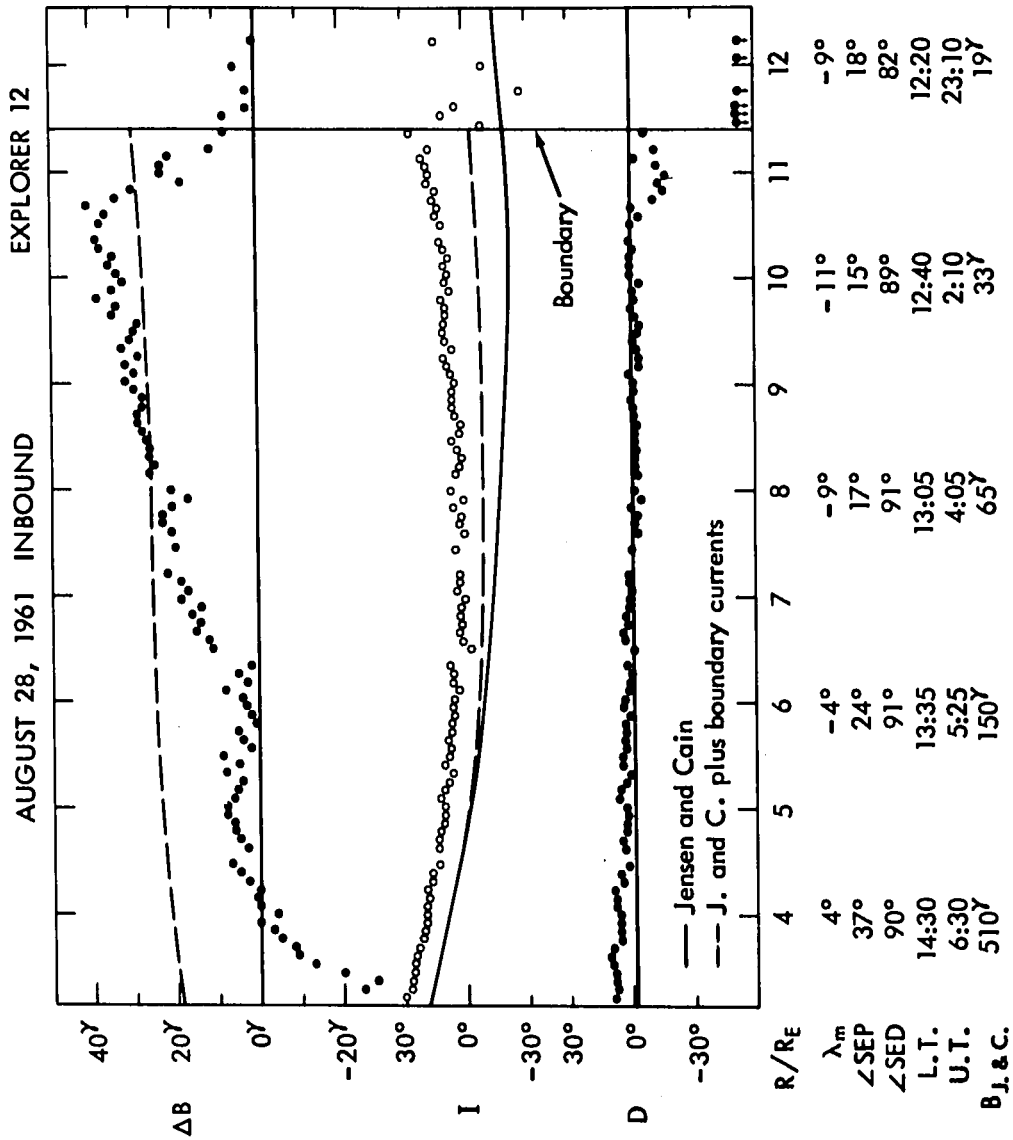


FIGURE 9

August 28, 1961, inbound pass. Note typical low-latitude enhancement of field magnitude near boundary, but decrease inside 4 R_E , indicating some quite-time inflation.

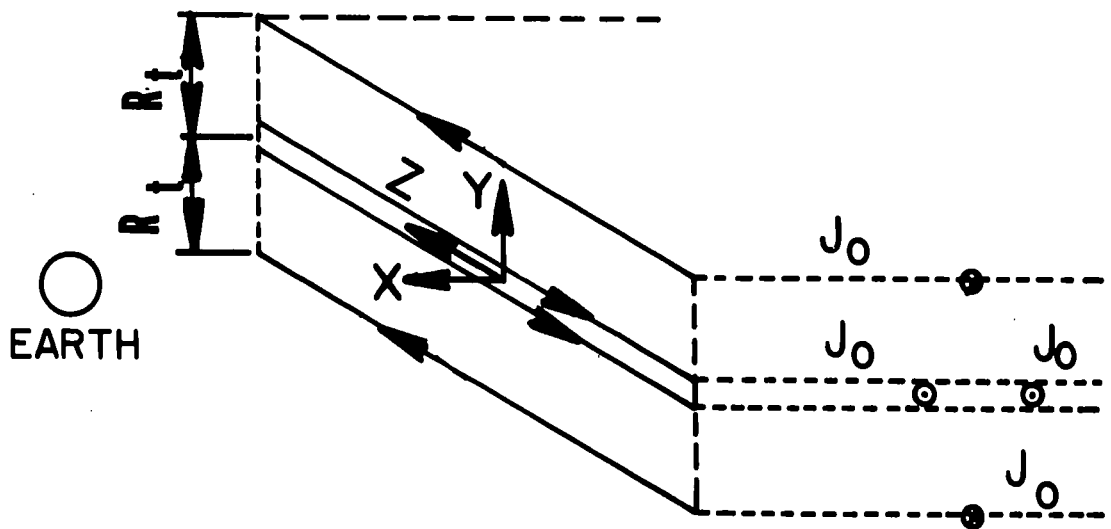


FIGURE 10

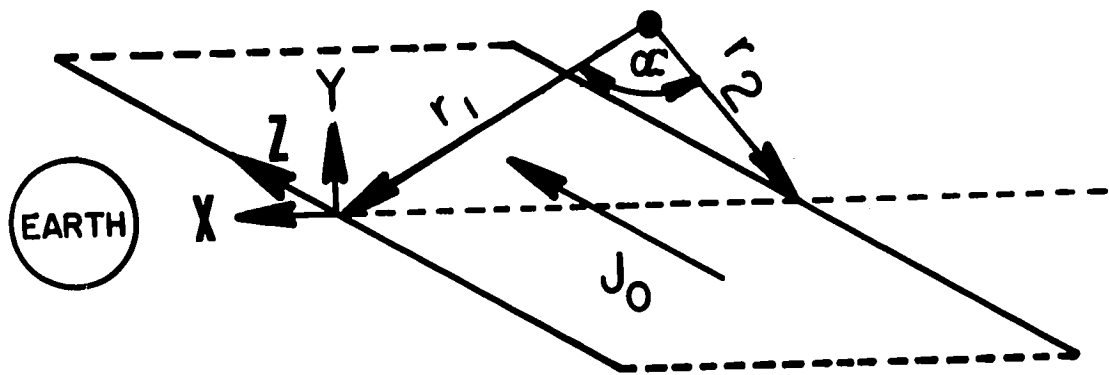


FIGURE 11

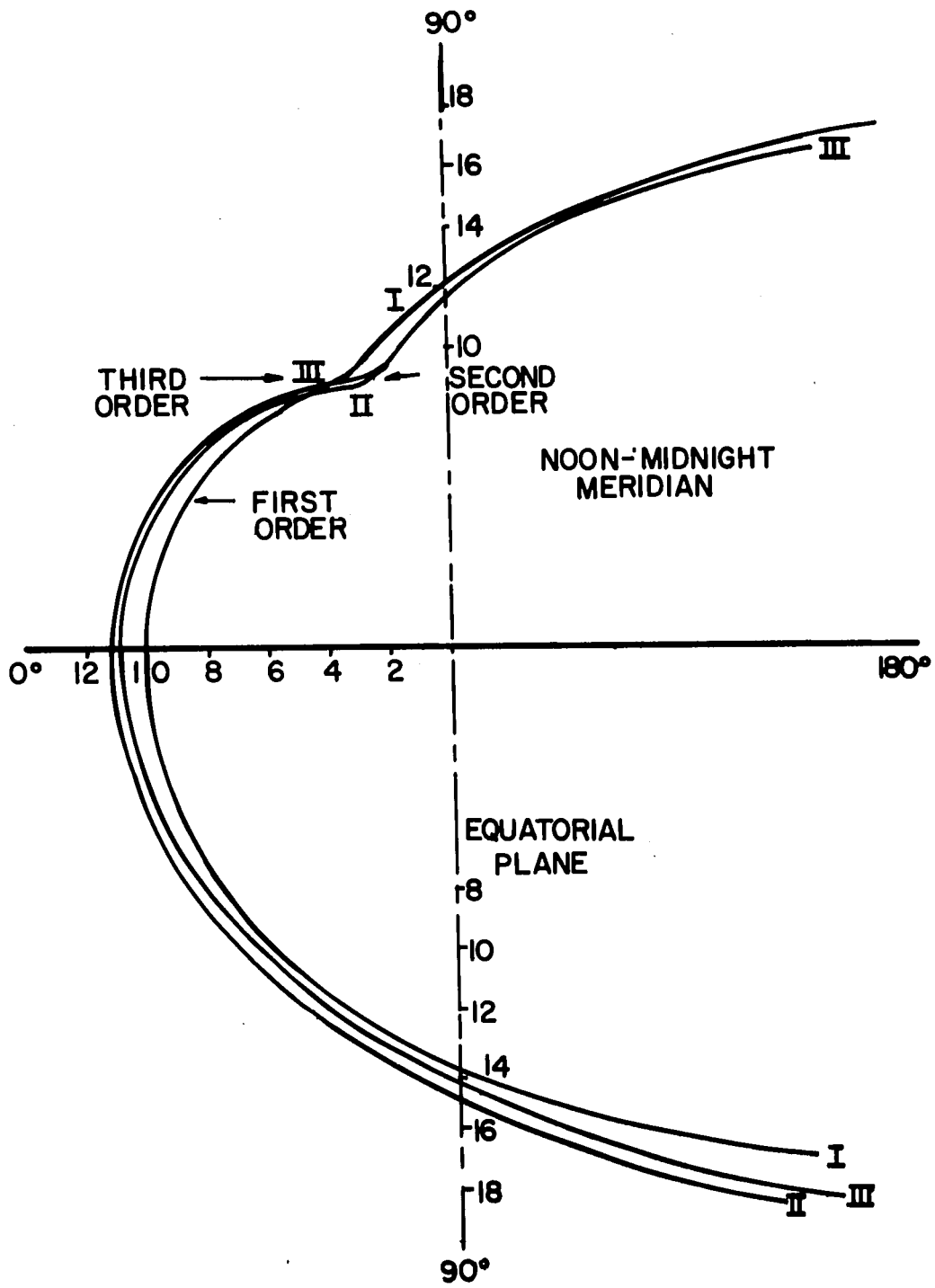


FIGURE 12

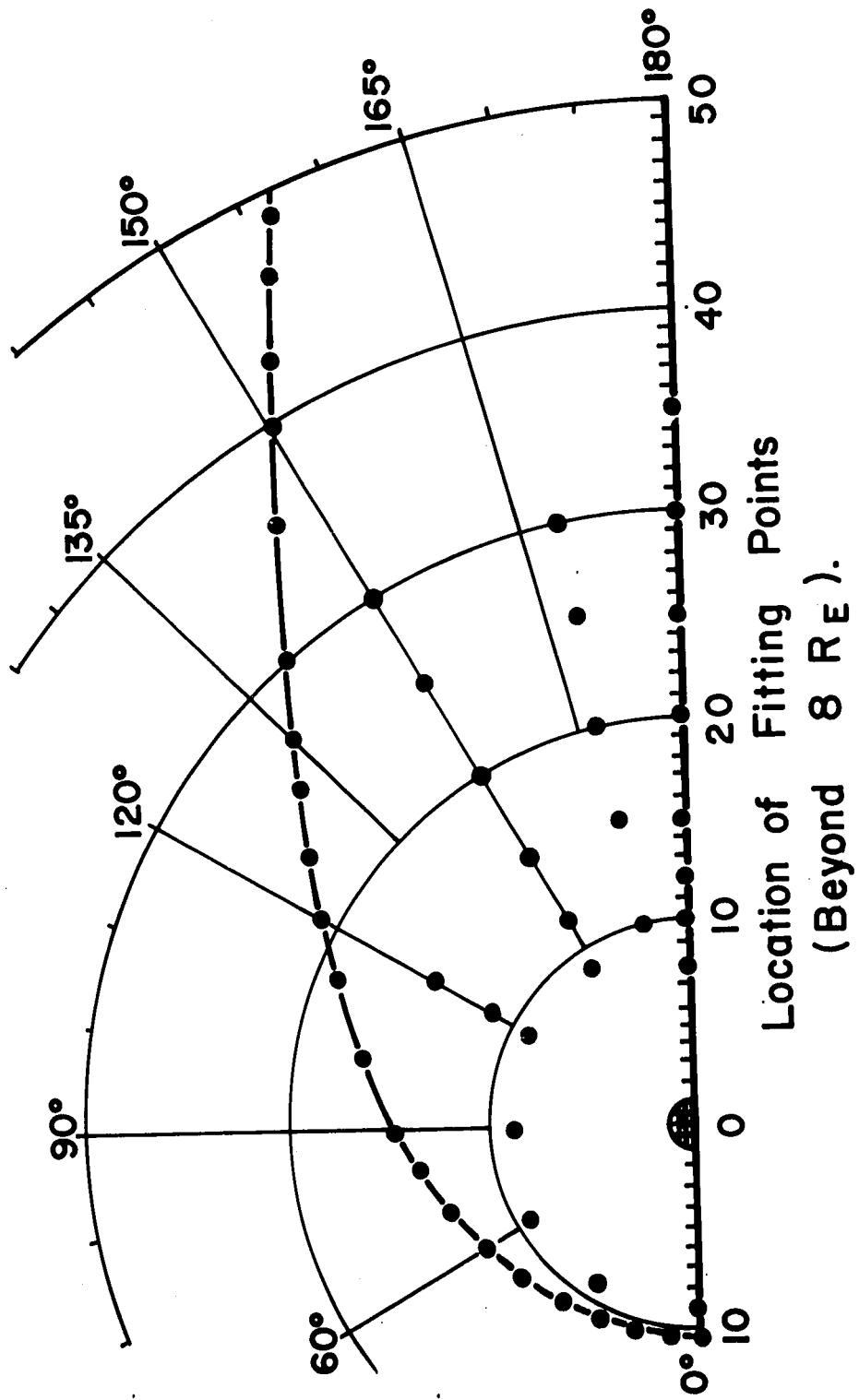


FIGURE 13

—MEAD'S FIELD LINES (WITHOUT QUIET-DAY RING CURRENT)

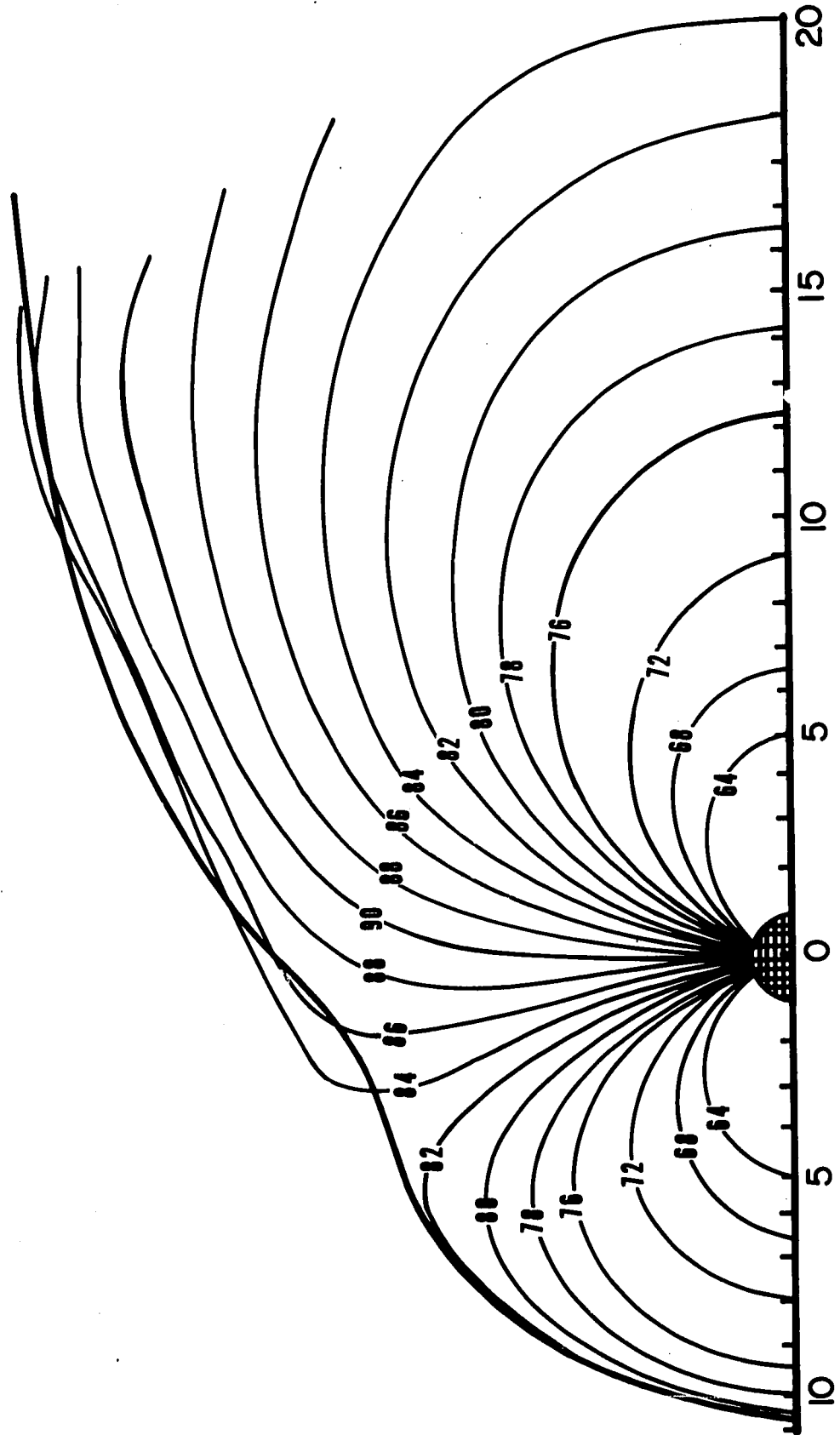


FIGURE 14

— MEAD'S FIELD LINES (WITHOUT QUIET-DAY RING CURRENT)

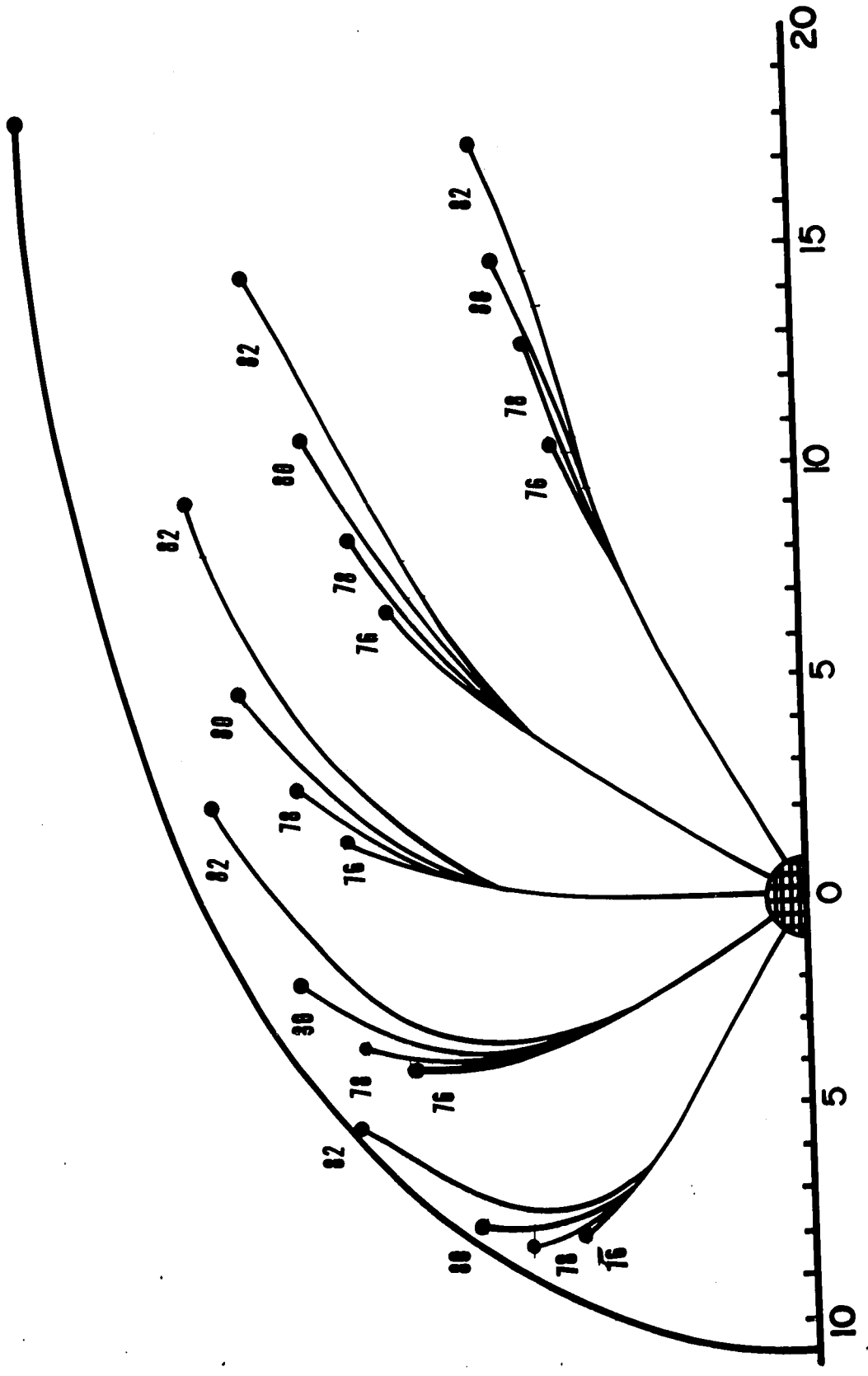


FIGURE 15

—SELF CONSISTENT SOLUTION WITH QUIET-DAY RING CURRENT.

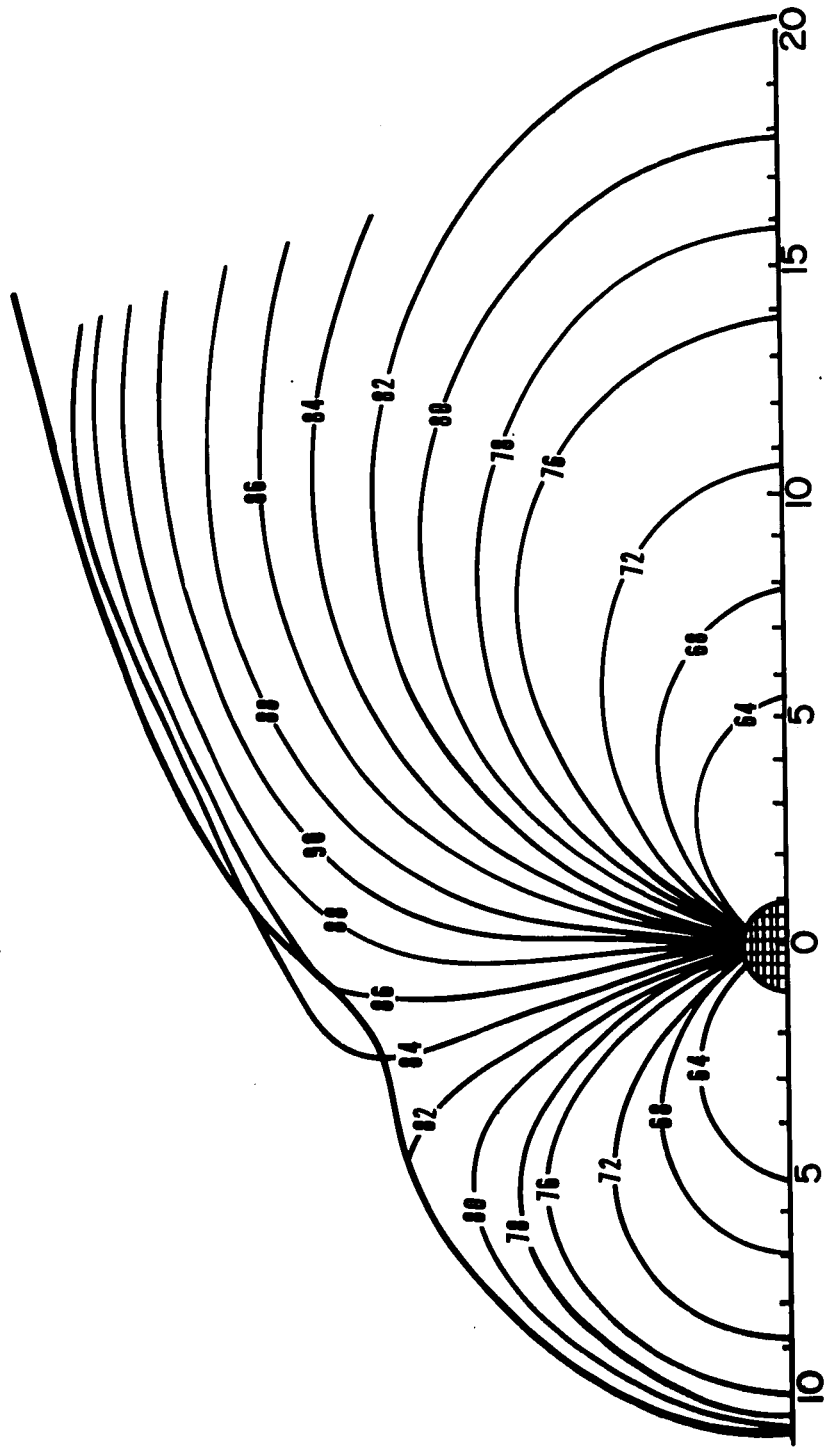


FIGURE 16

— SELF CONSISTENT SOLUTION WITH QUIET-DAY RING CURRENT

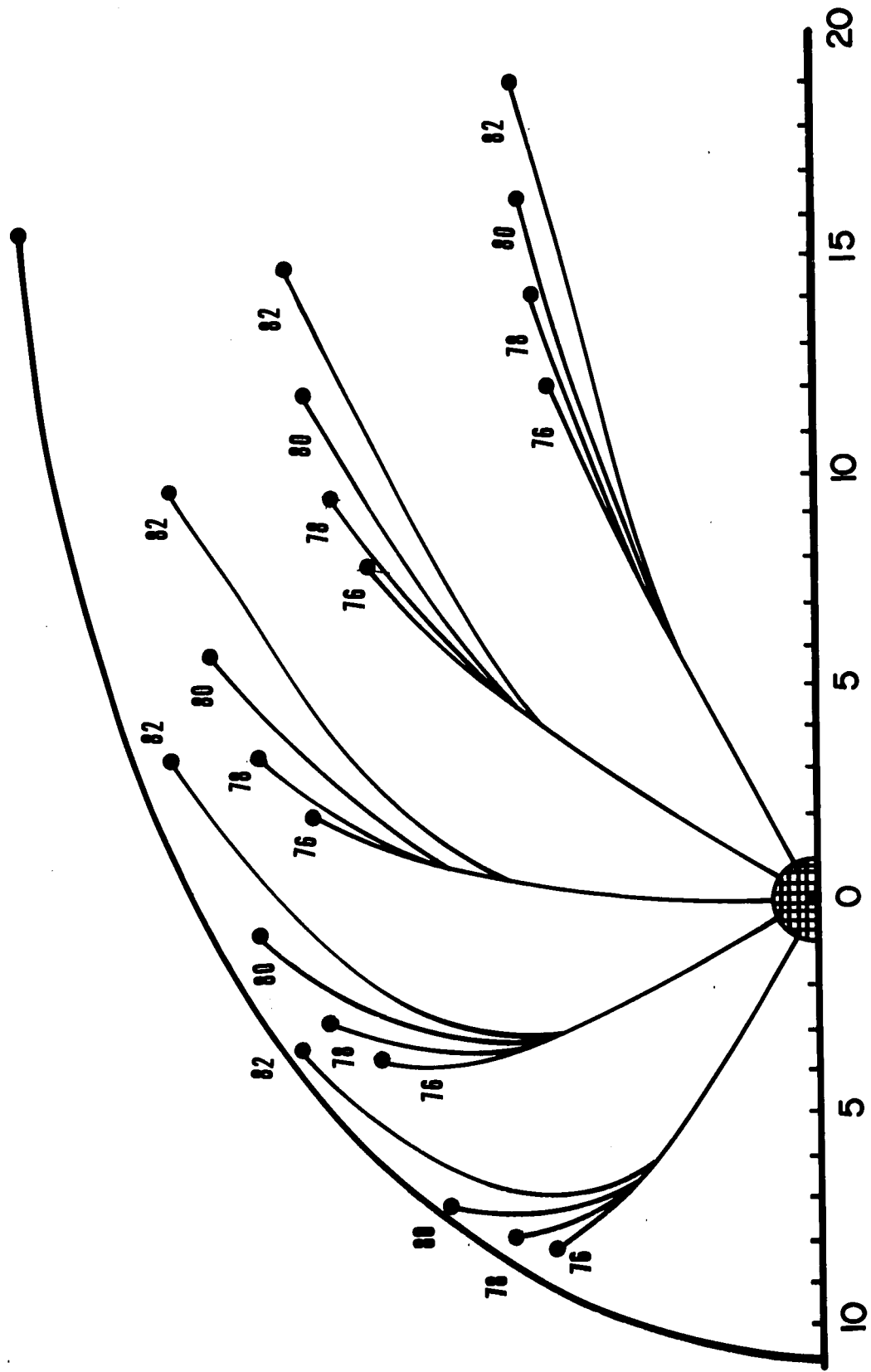


FIGURE 17

— SELF CONSISTENT SOLUTION WITH QUIET-DAY RING CURRENT

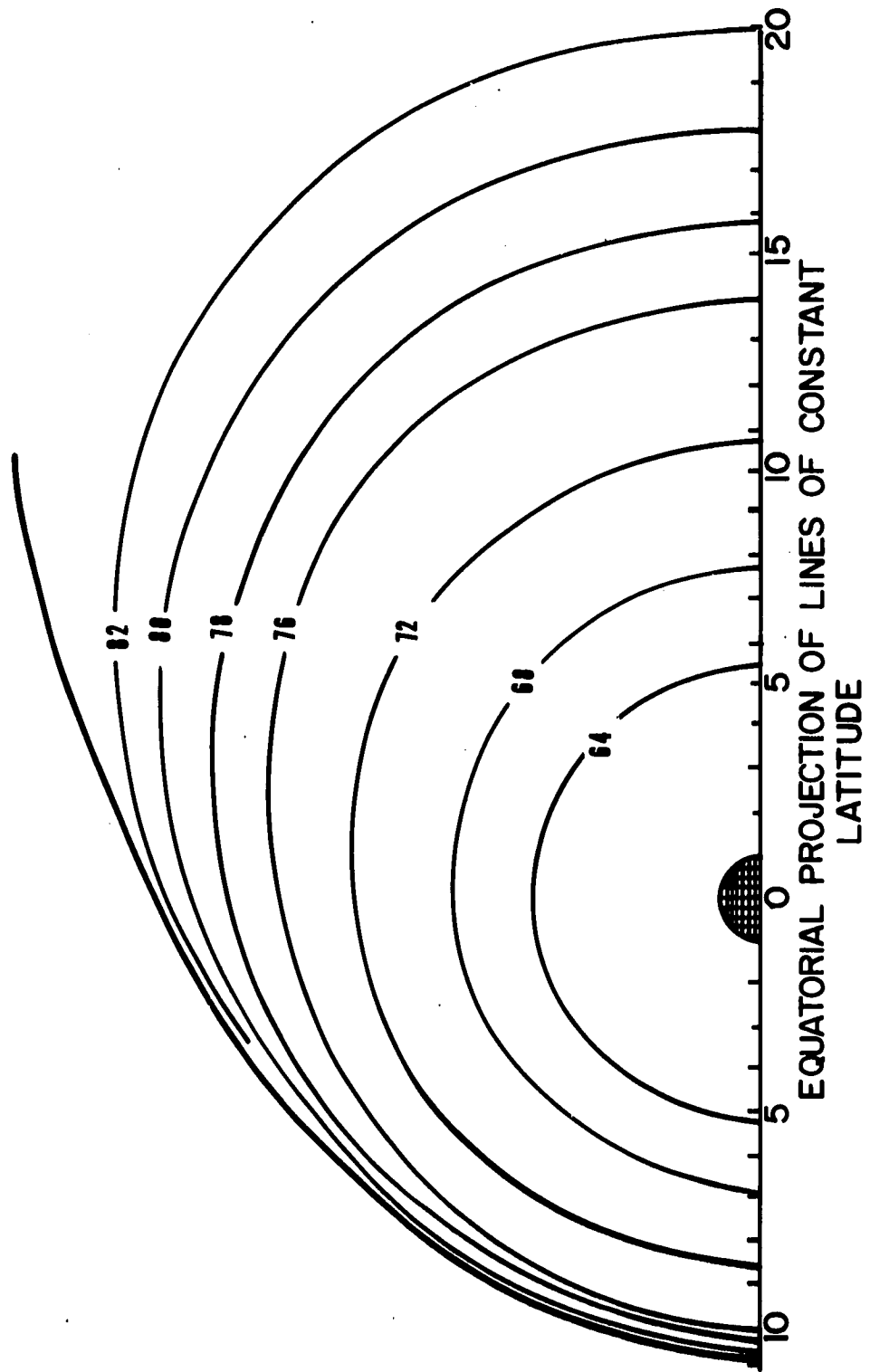


FIGURE 18

-----SELF CONSISTENT SOLUTION WITH QUIET-DAY RING CURRENT.

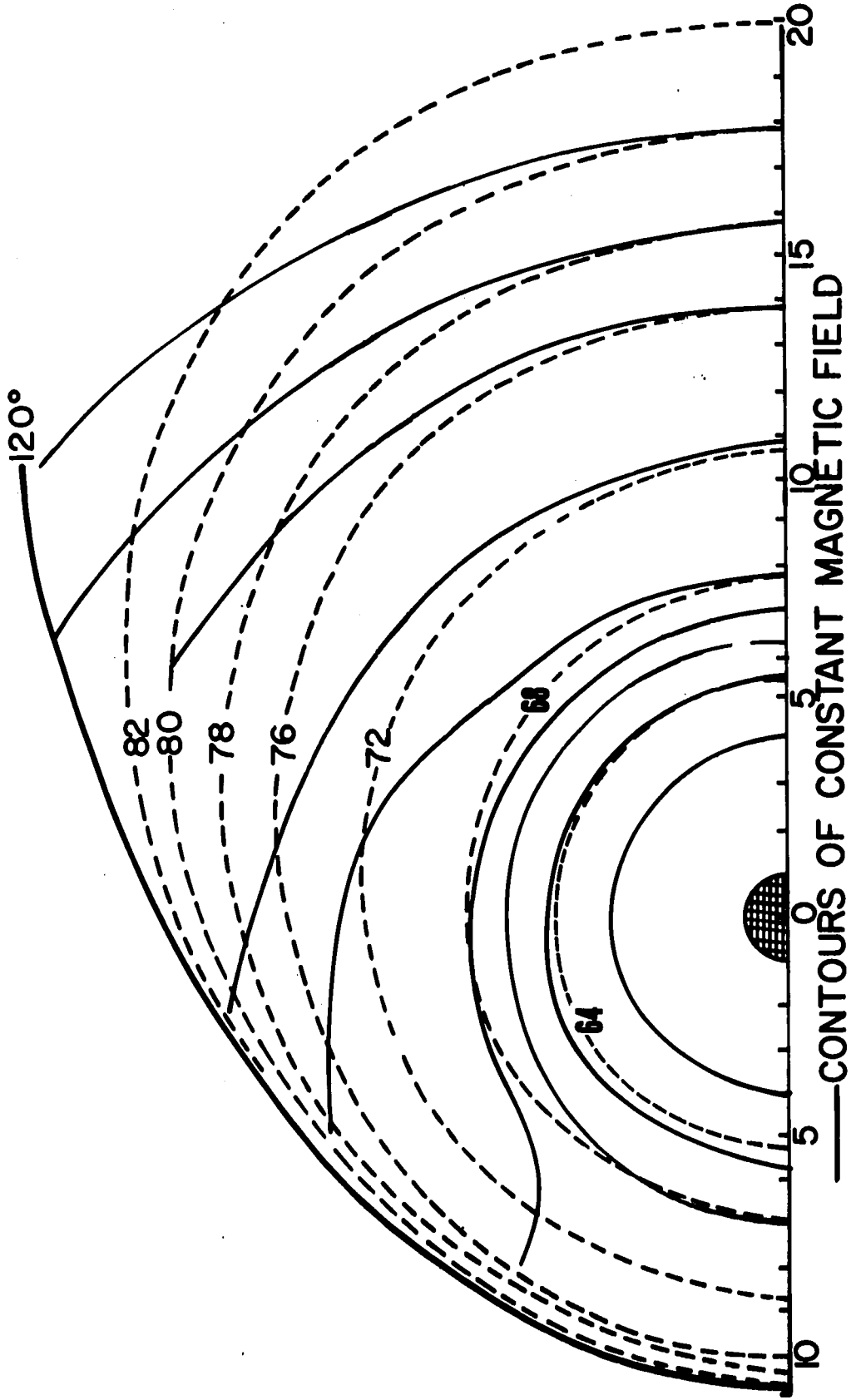
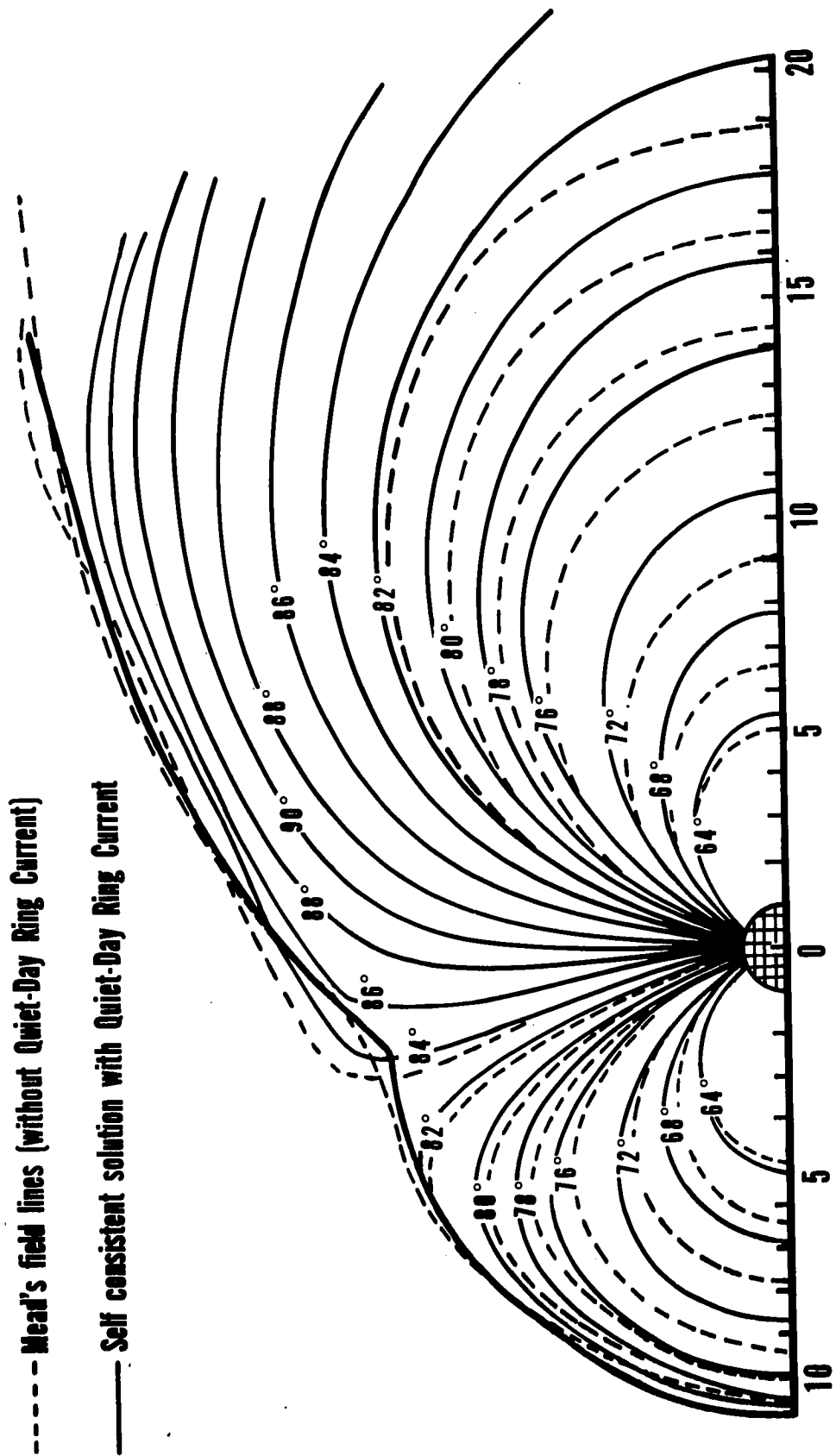


FIGURE 19



----- Mead's field lines (without Quiet-Day Ring Current)

———— Self consistent solution with Quiet-Day Ring Current

FIGURE 20

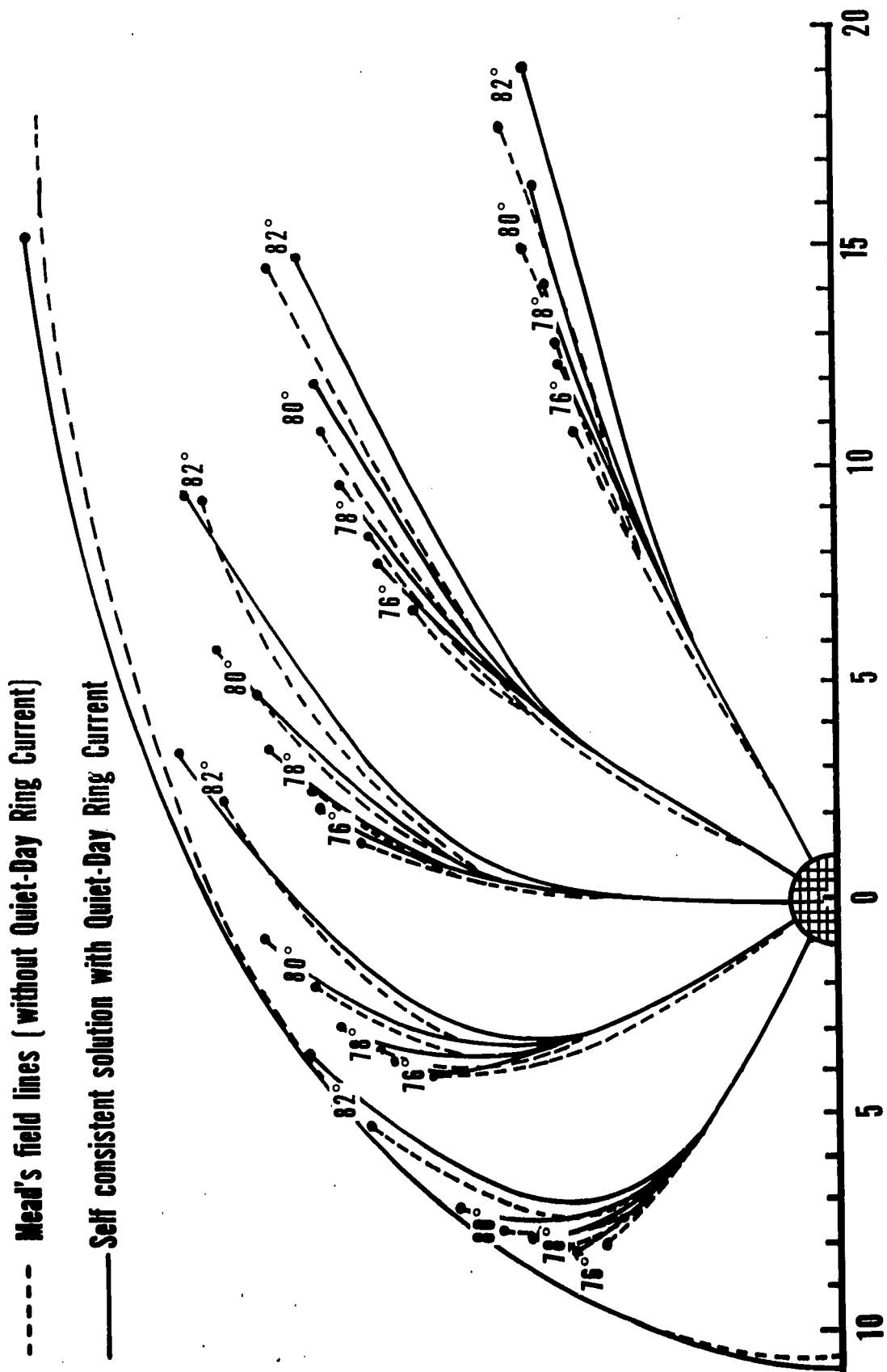


FIGURE 21

Tail Field of 30γ
'beyond' $10 R_E$

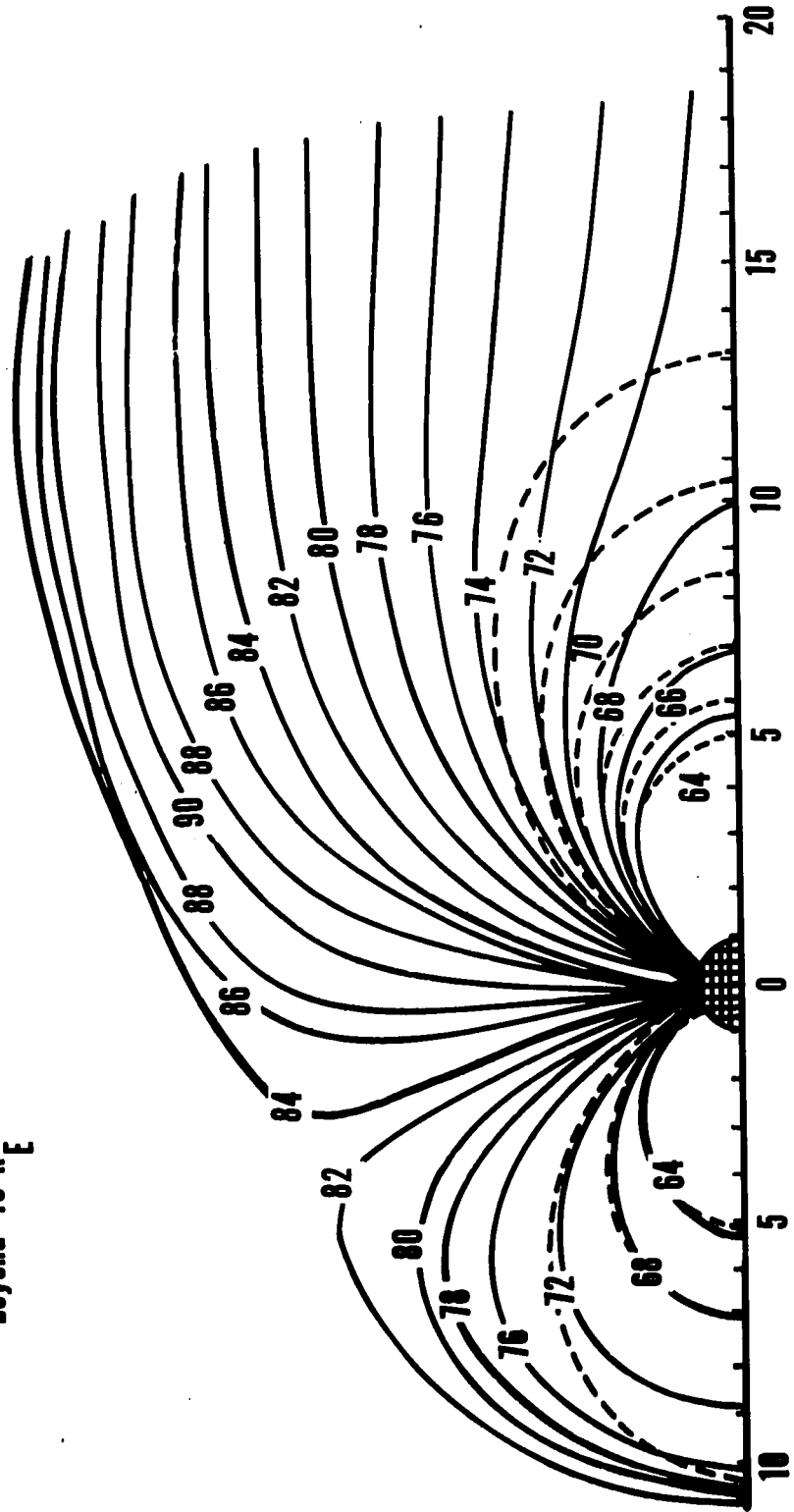


FIGURE 22

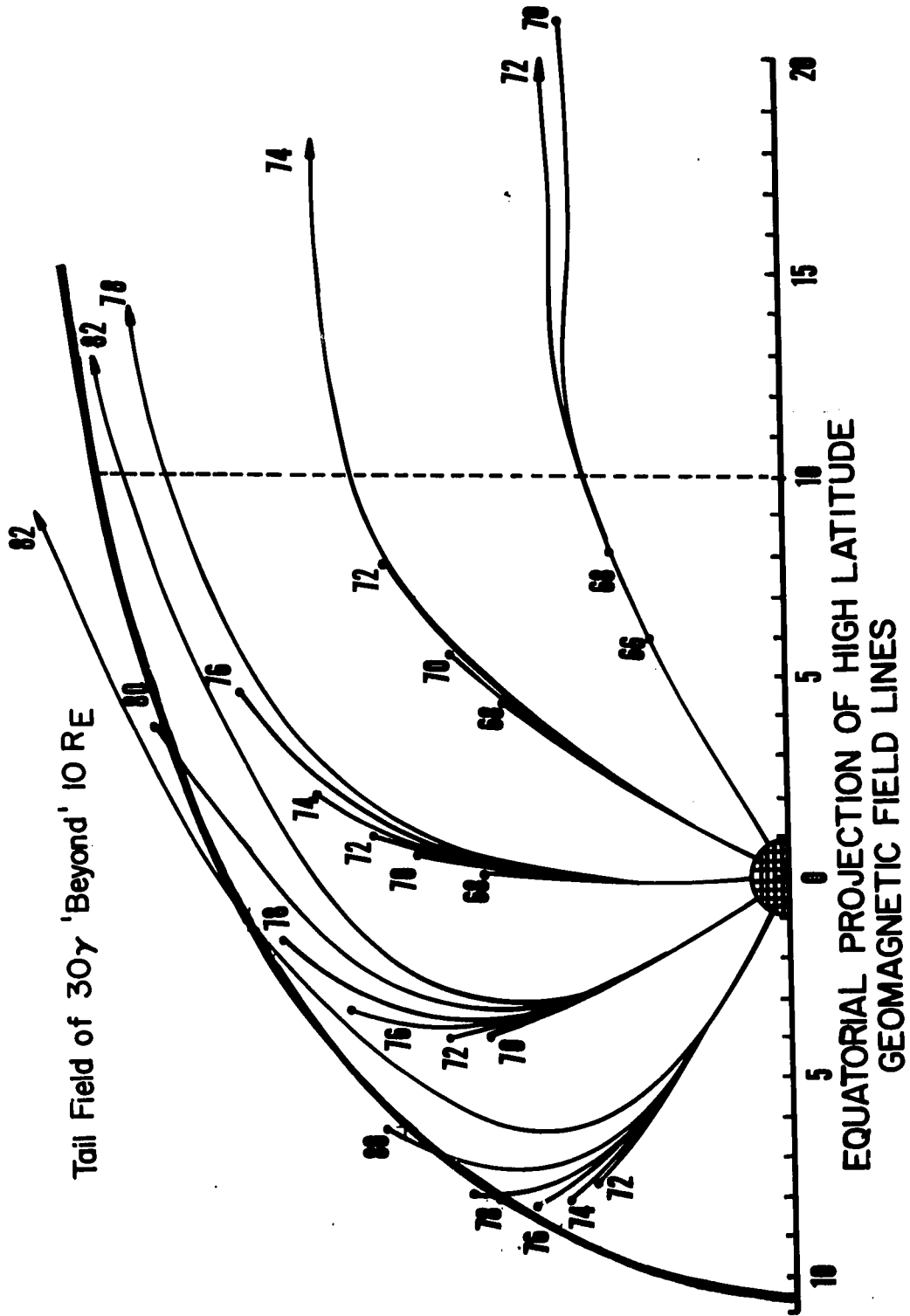


FIGURE 23

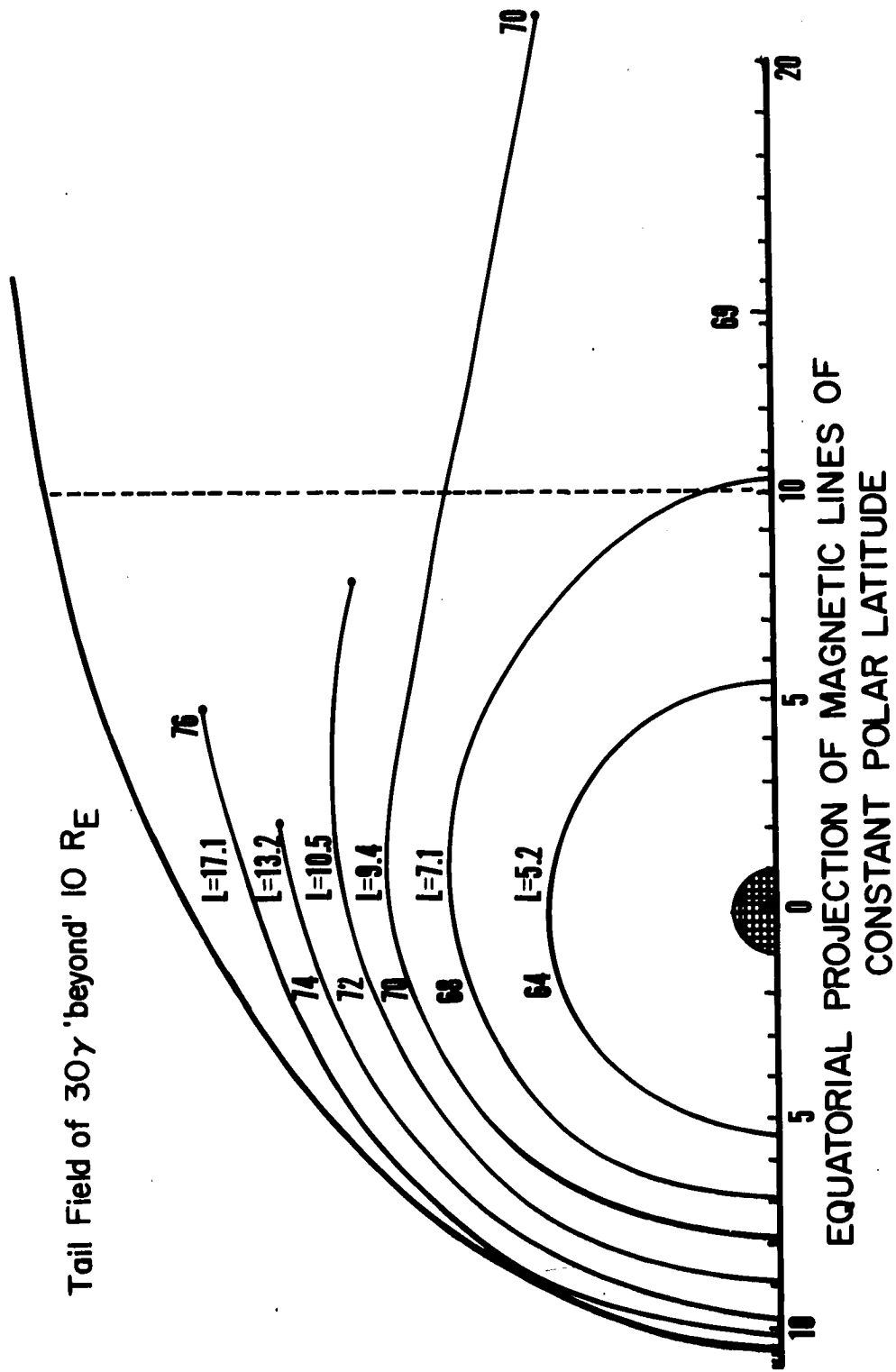


FIGURE 24

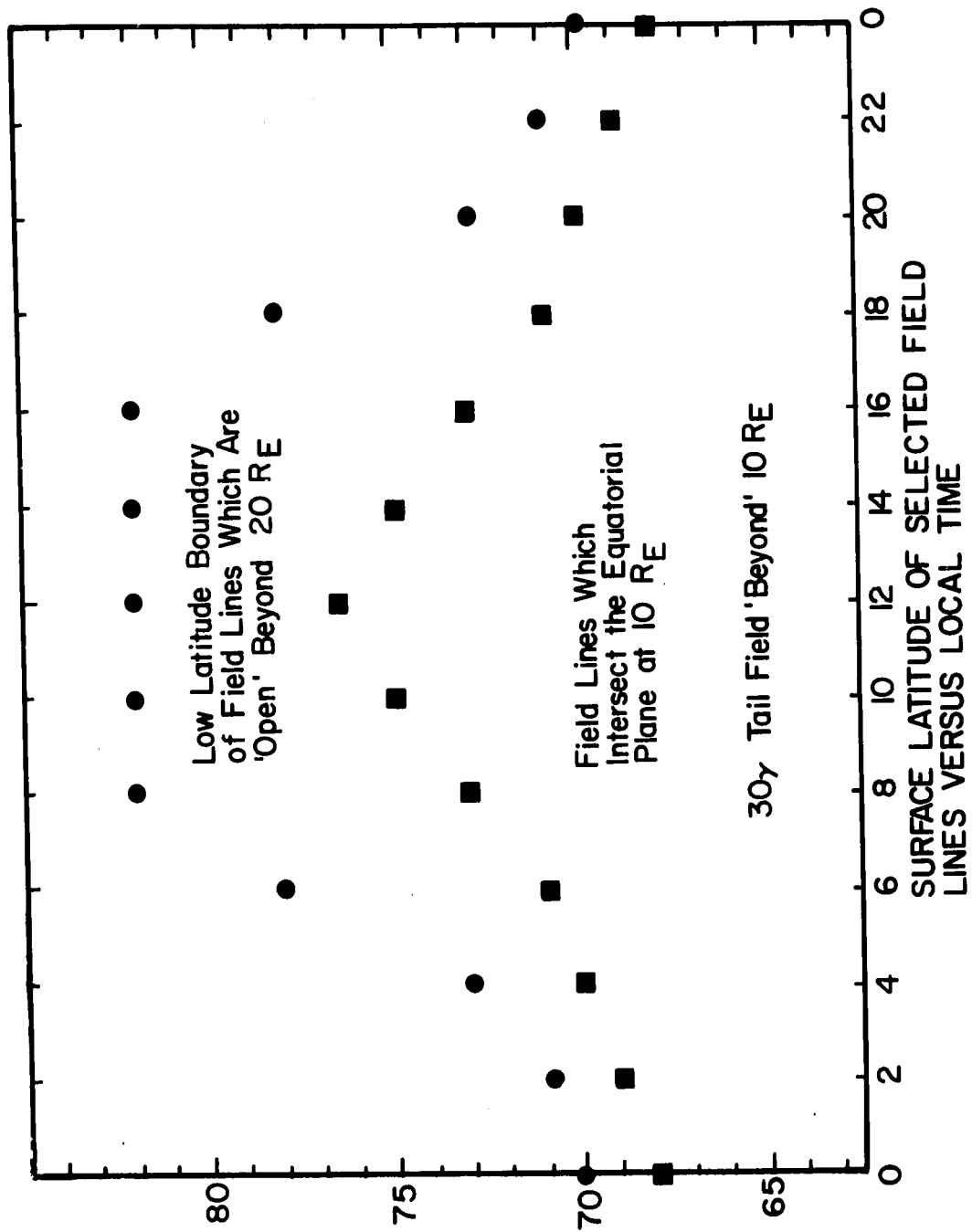


FIGURE 25

B Tail = 30° Rinner = 12 R E

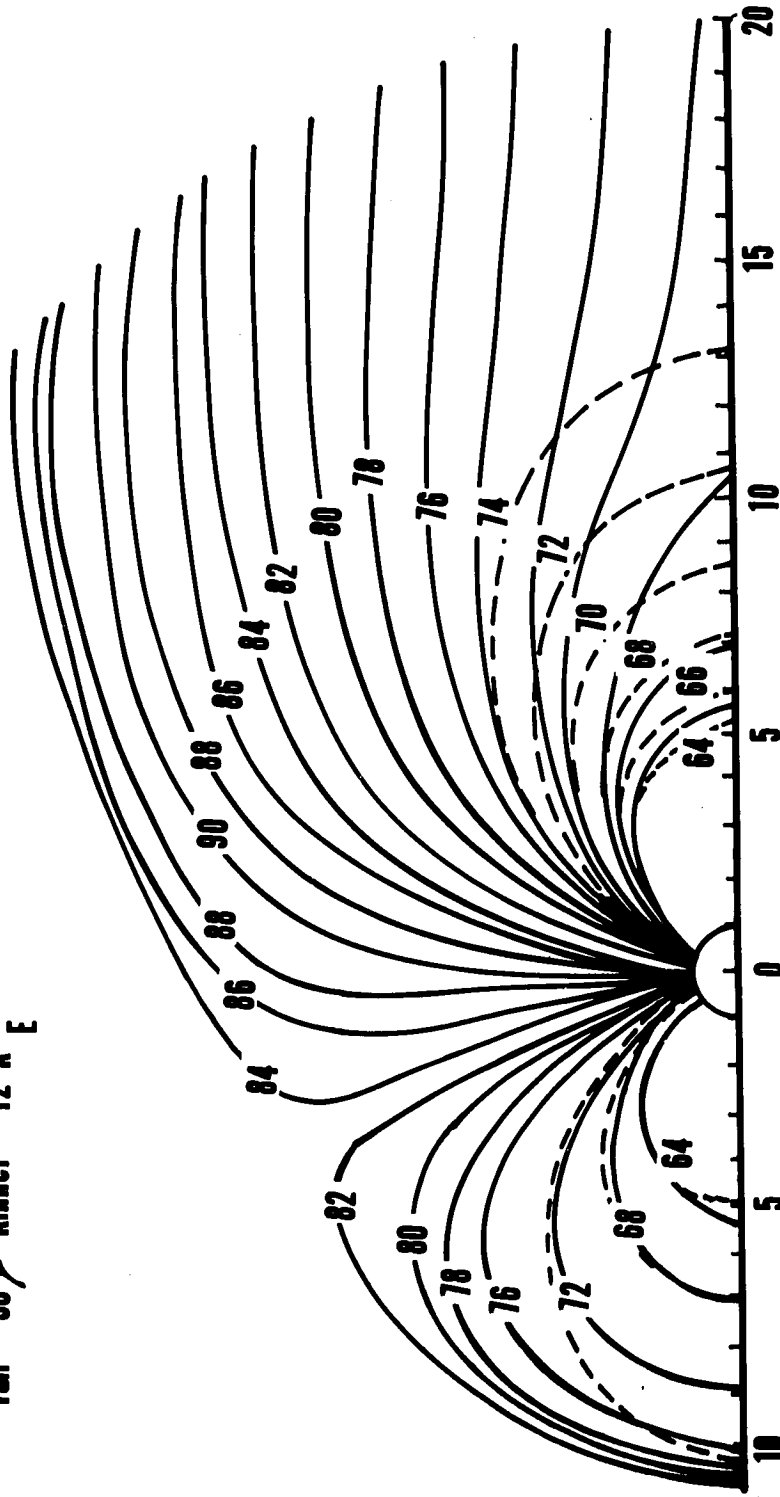
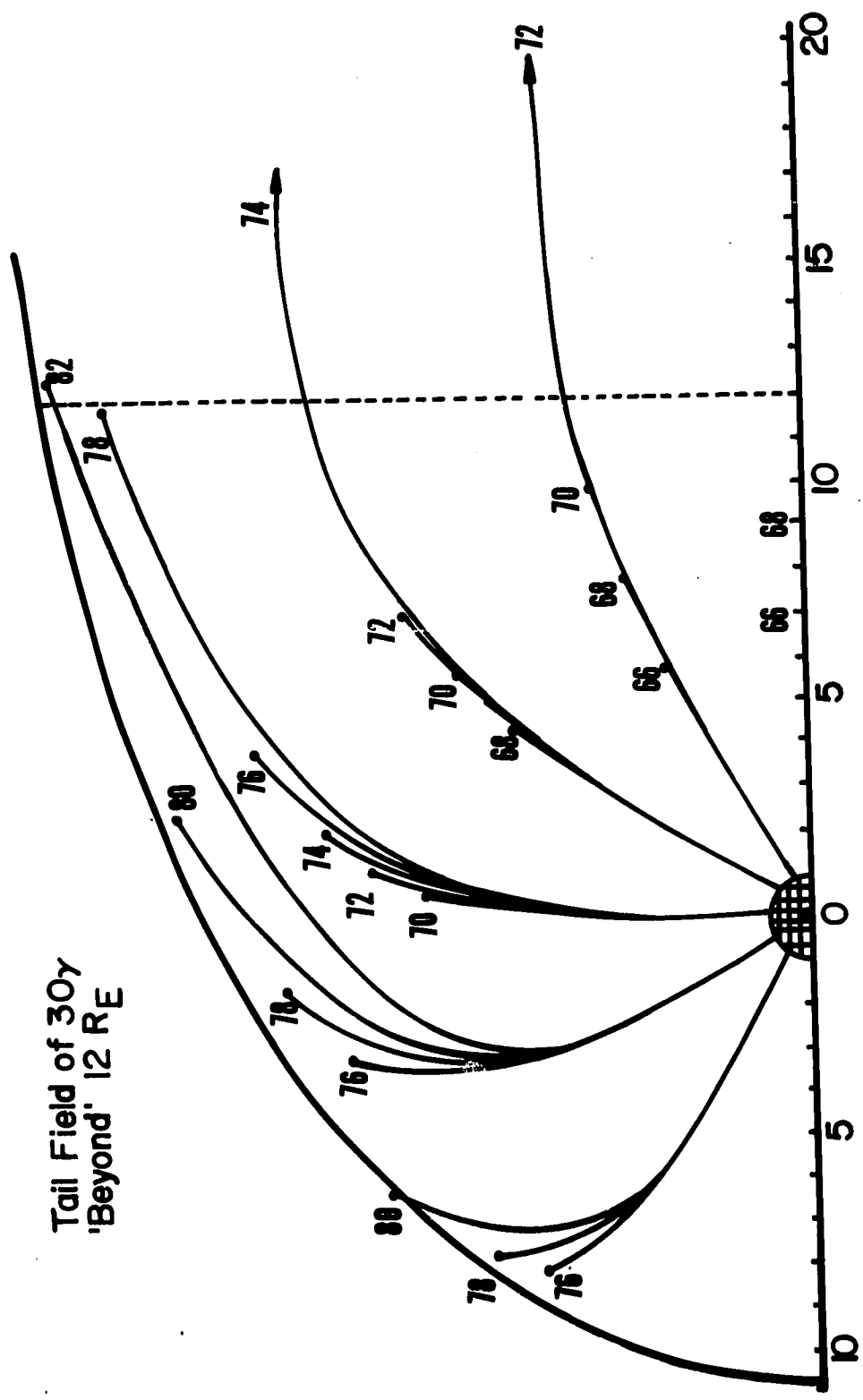


FIGURE 26



Tail Field of 30y
'Beyond' 12 RE

FIGURE 27

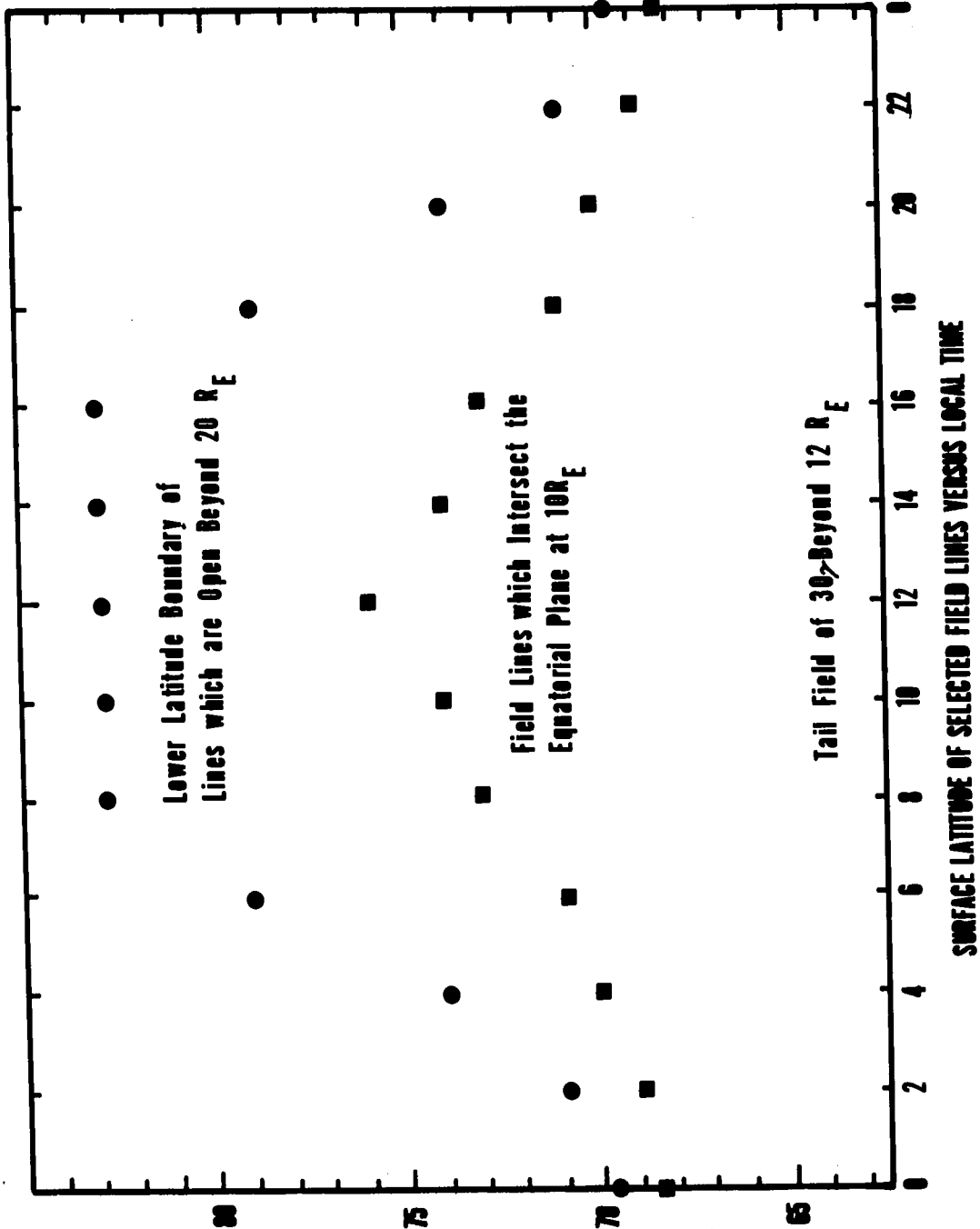


FIGURE 28

Tail Field 15γ 'beyond' 10 R_E

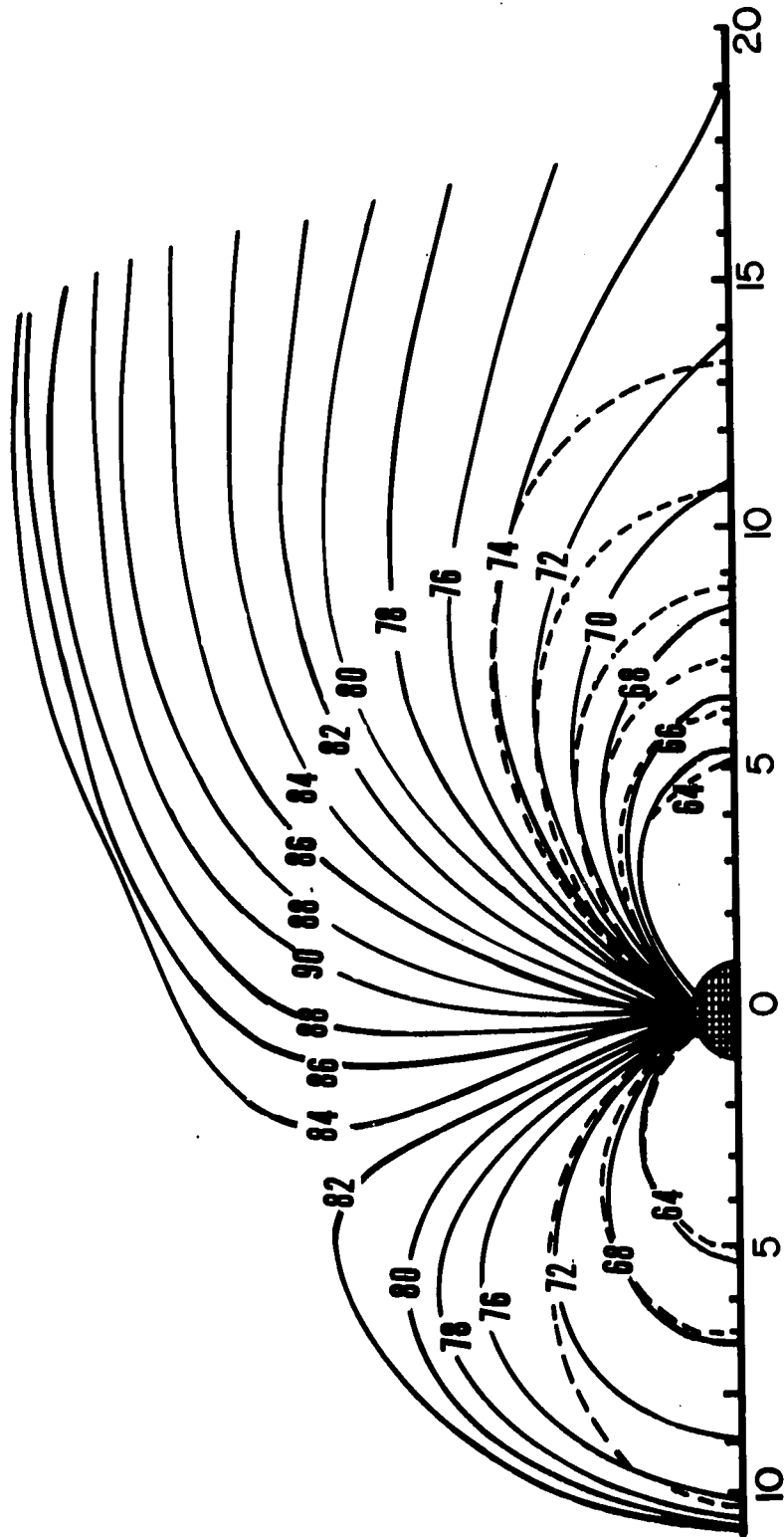


FIGURE 29

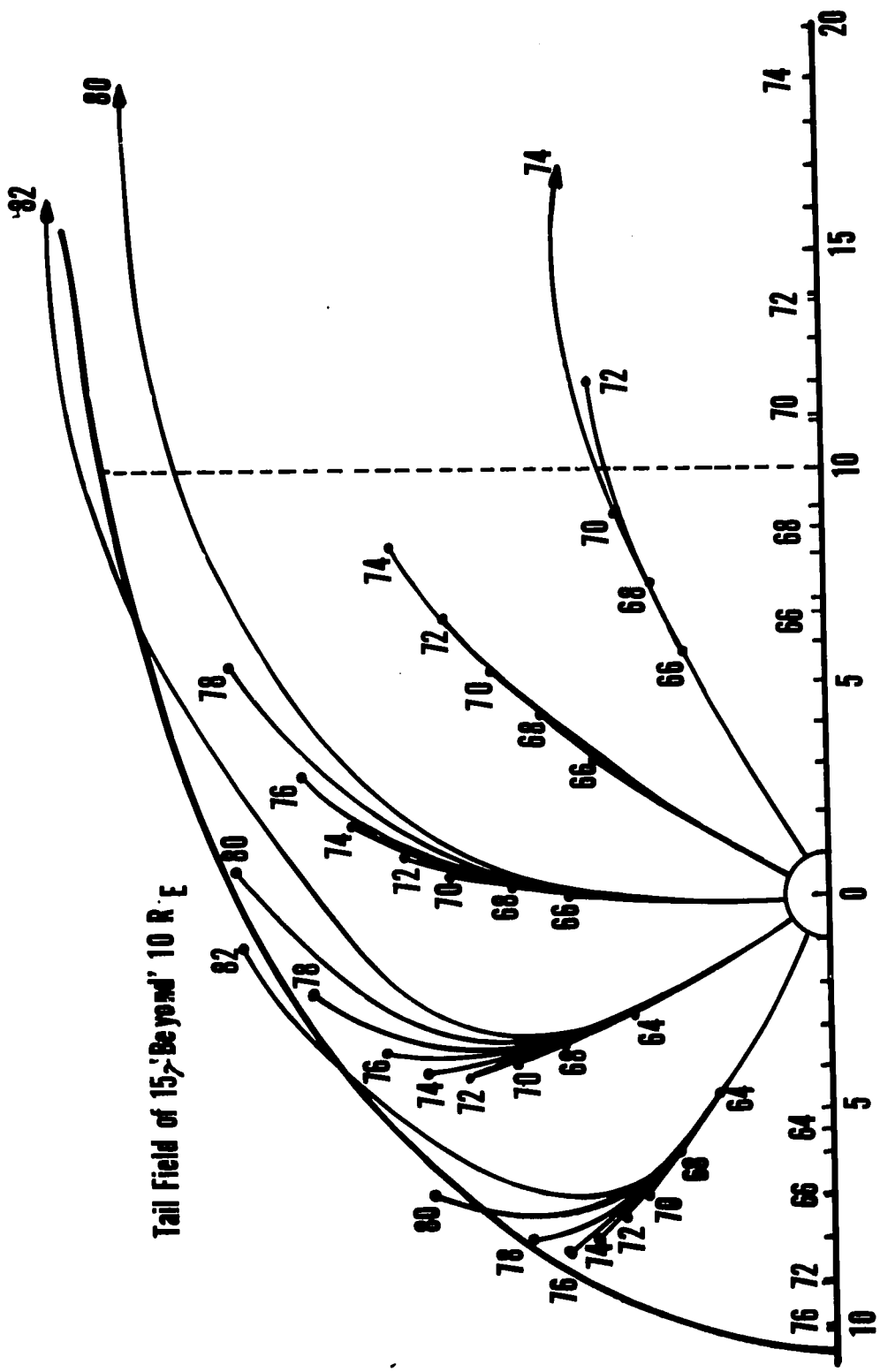


FIGURE 30

Tail Field of 15γ
'Beyond' 10 R E

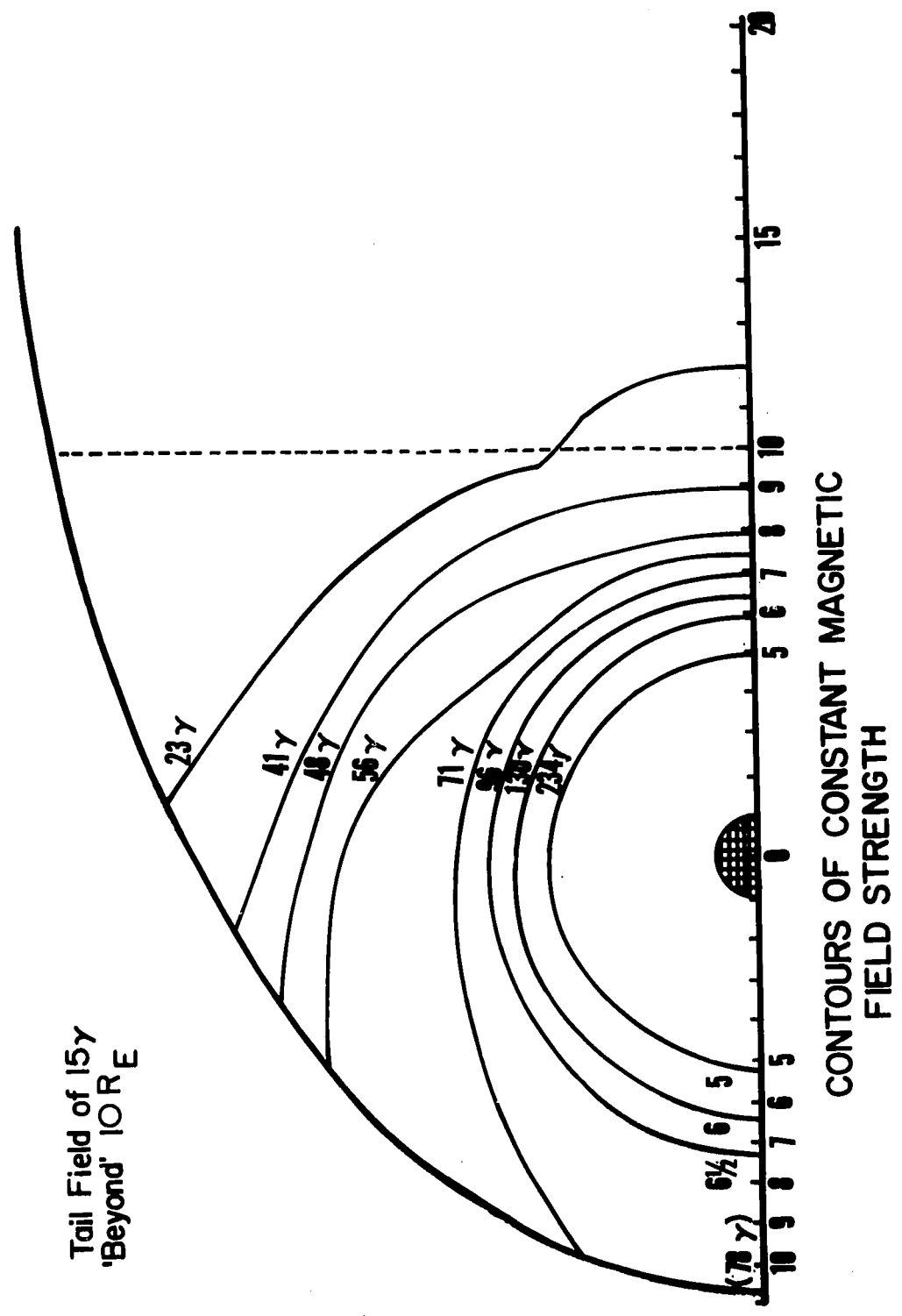


FIGURE 31

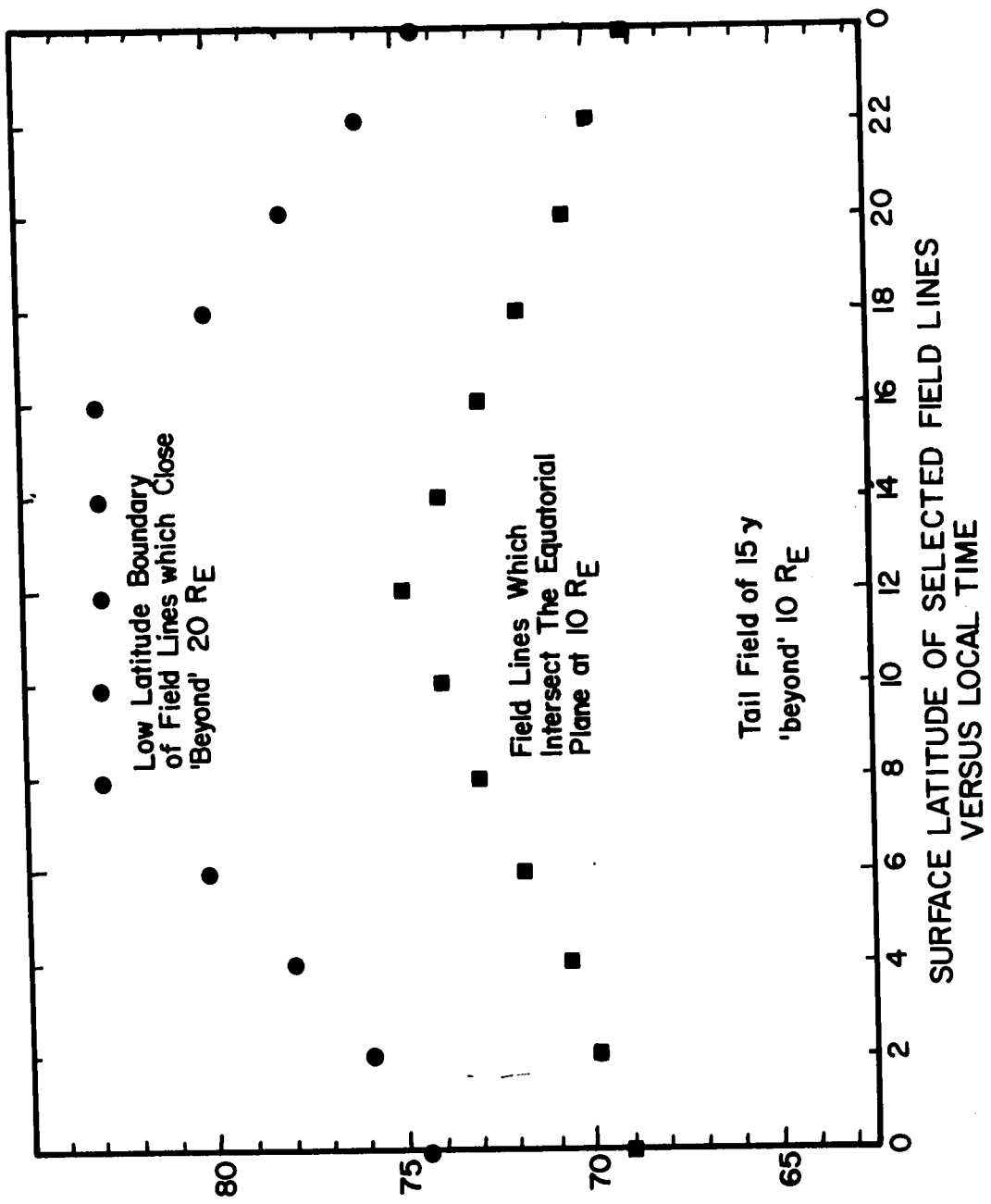


FIGURE 32

Tail Field of 15γ 'Beyond' 12 RE

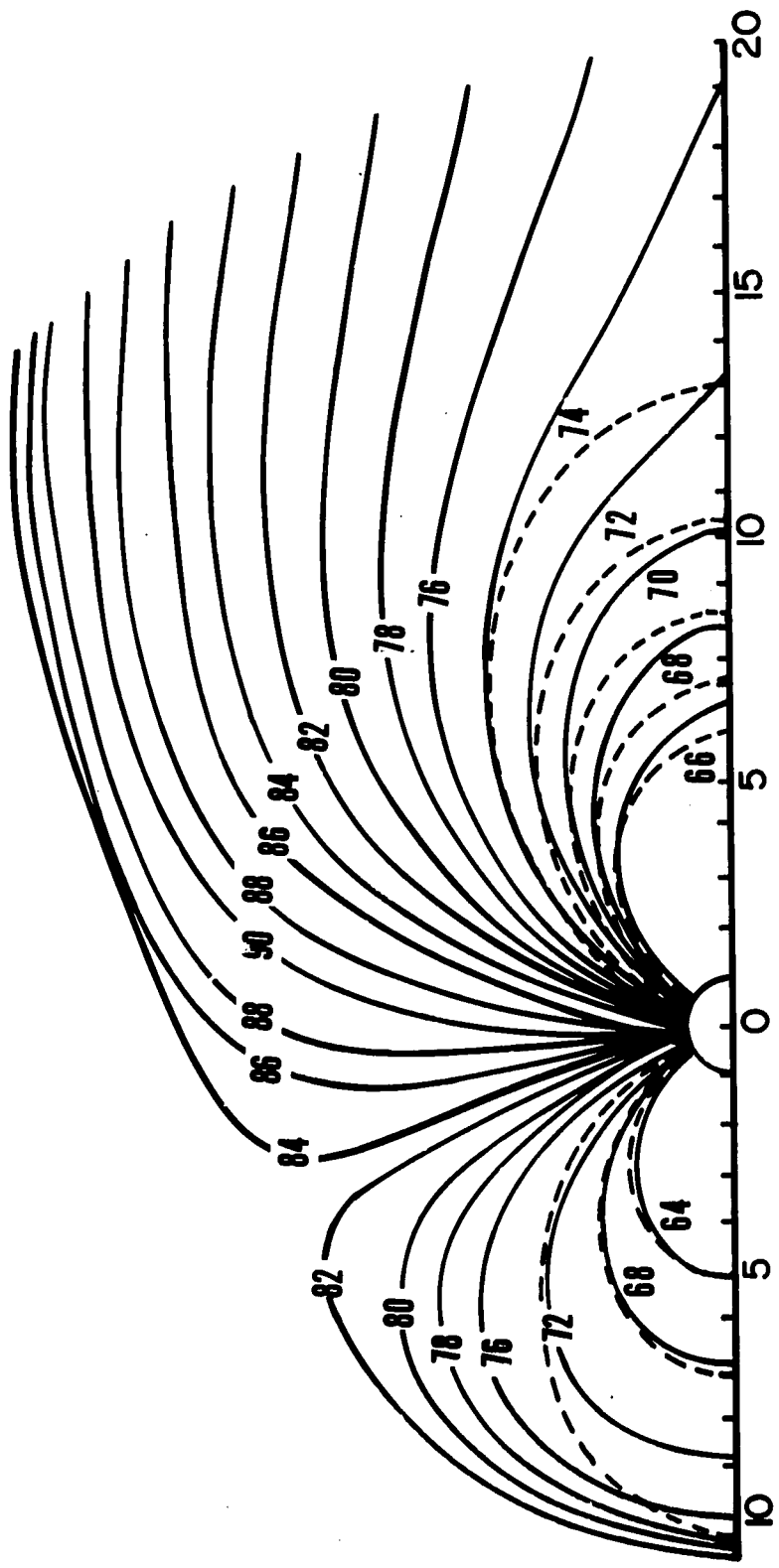


FIGURE 33

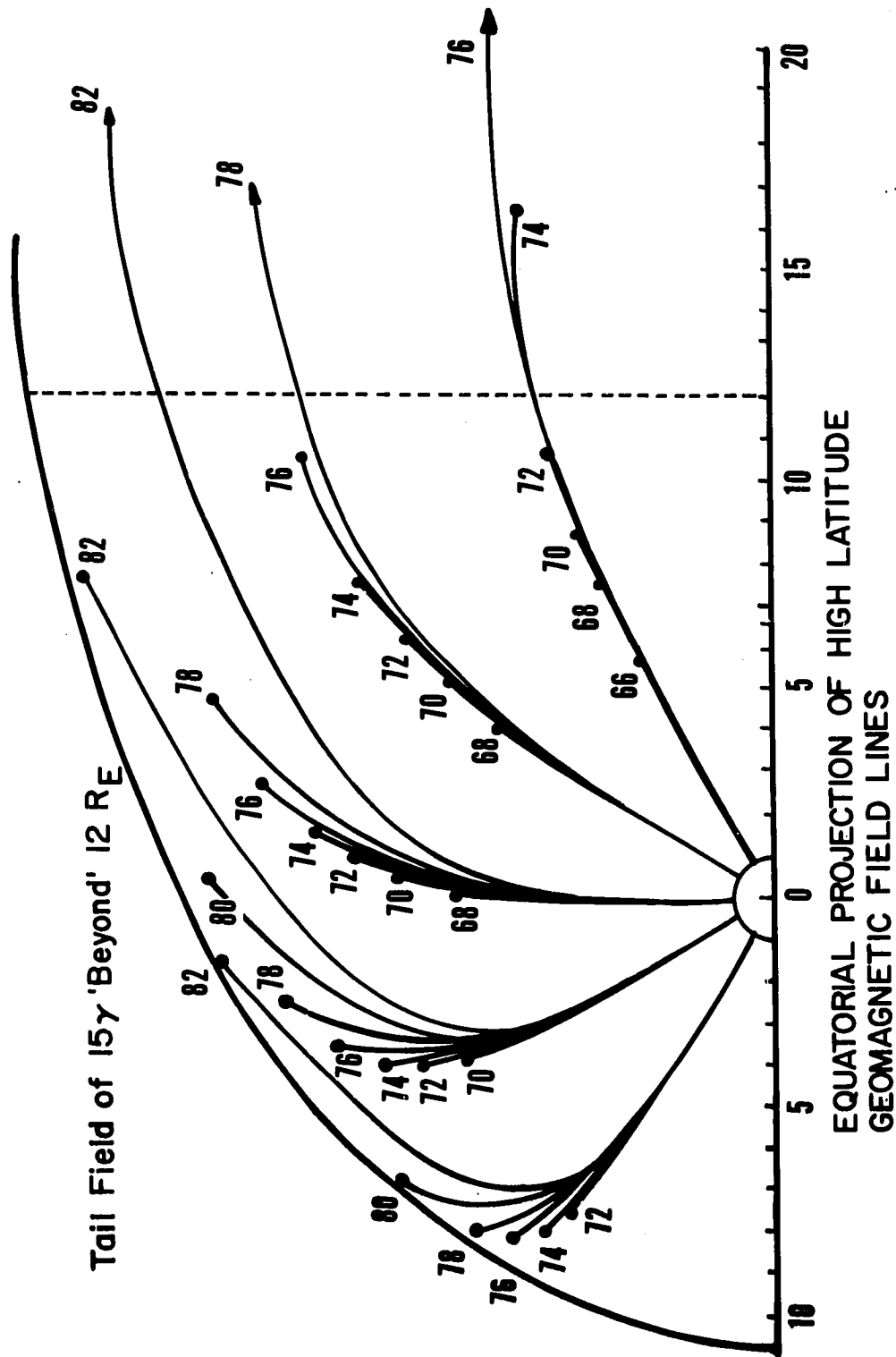


FIGURE 34

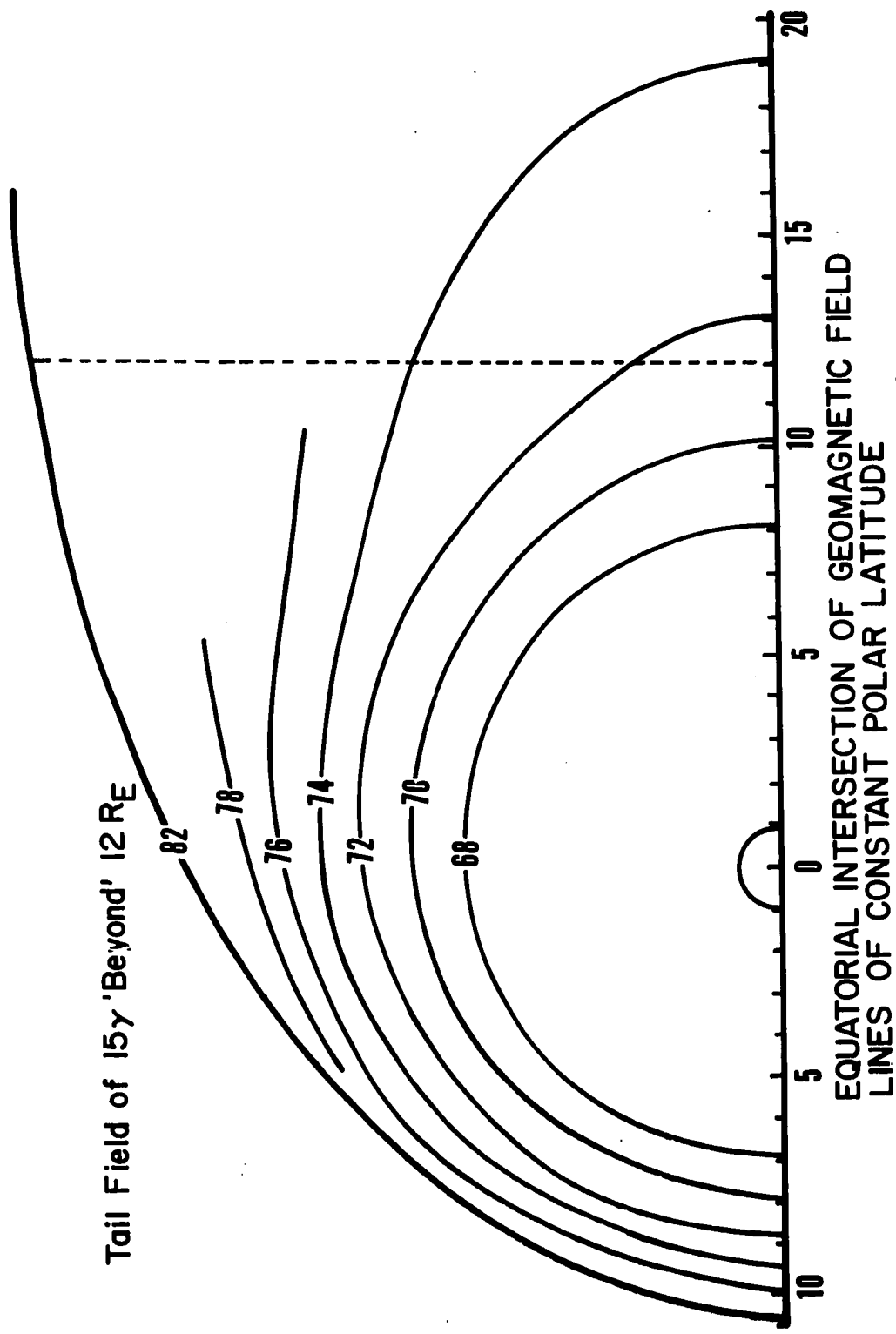


FIGURE 35 1

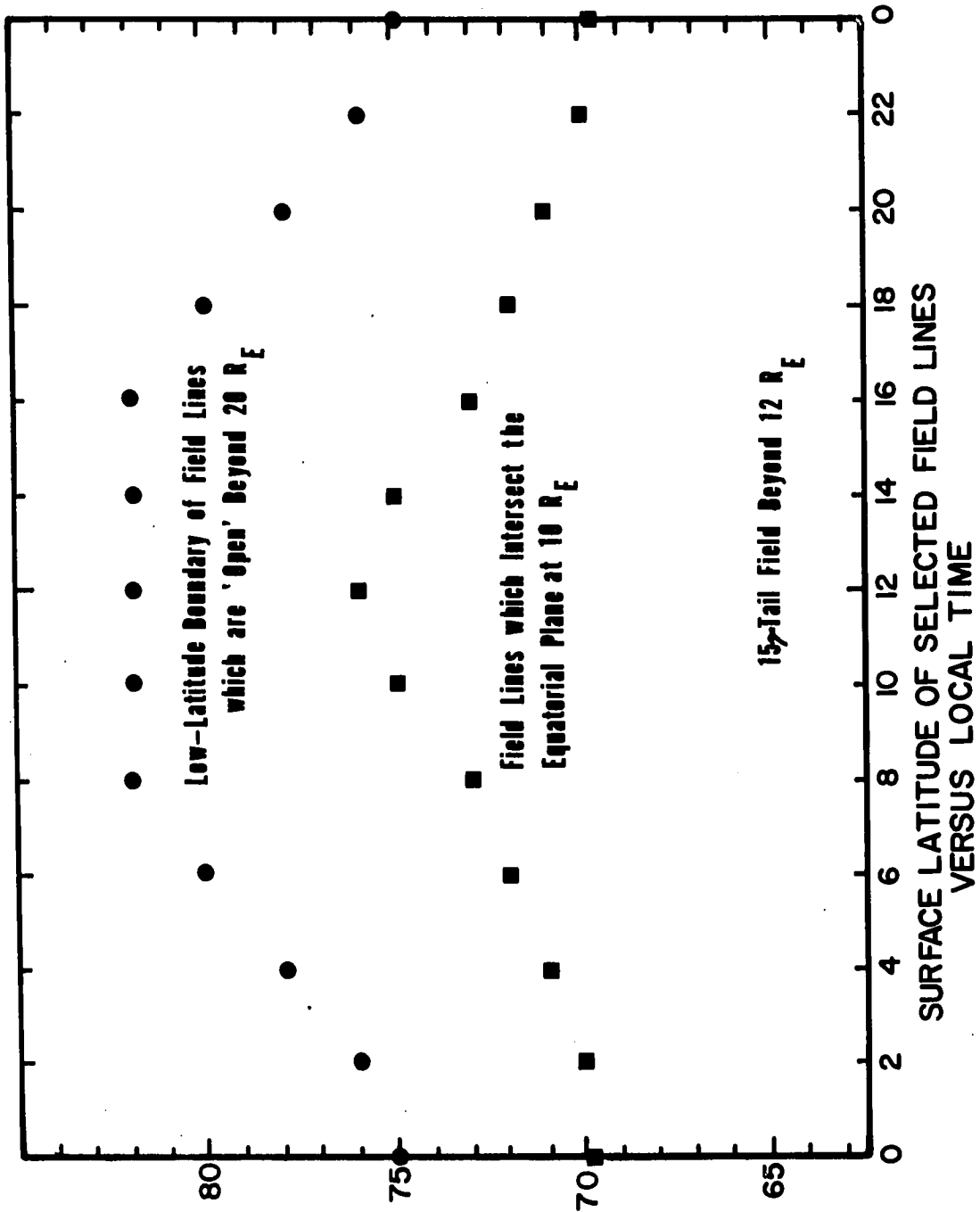


FIGURE 36.

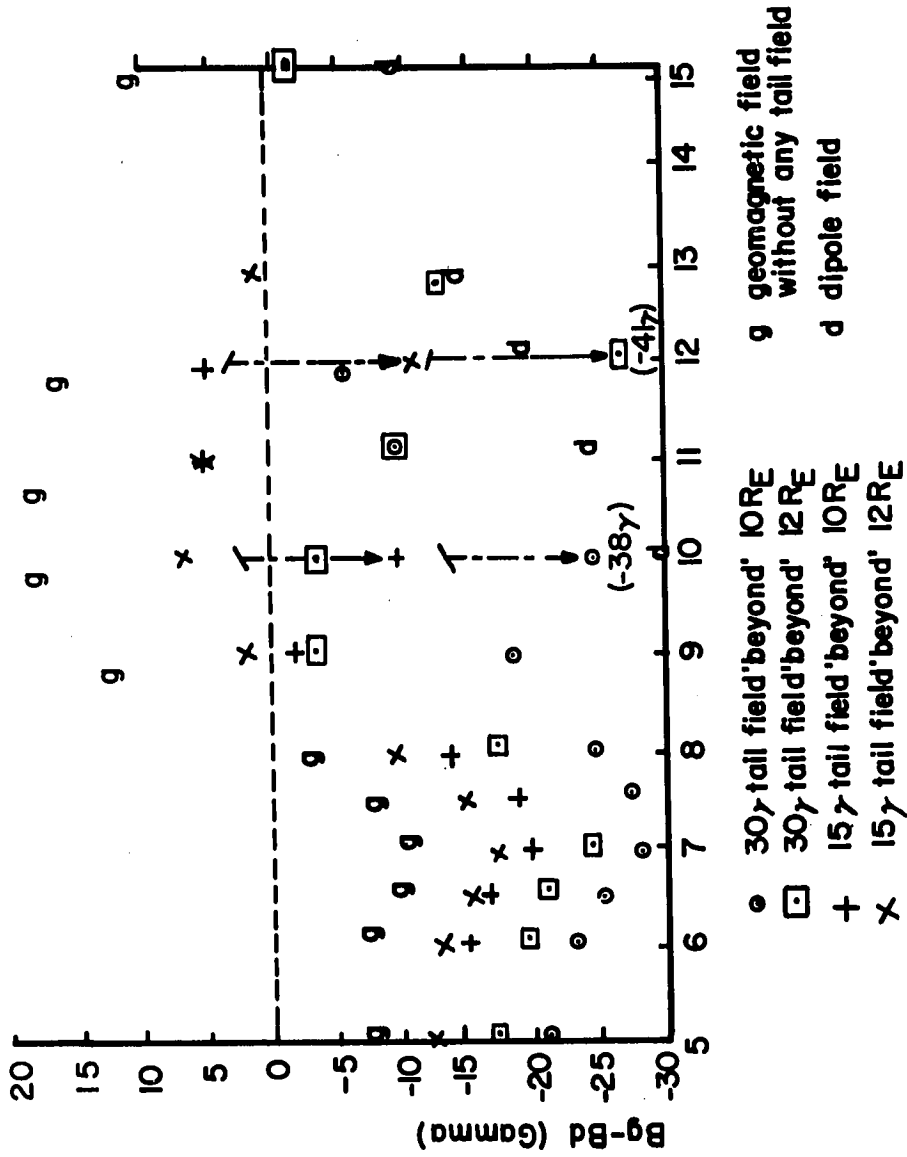


FIGURE 37

EQUATORIAL GEOMAGNETIC FIELD IN THE
MIDNIGHT MERIDIAN

L. A. FRANK

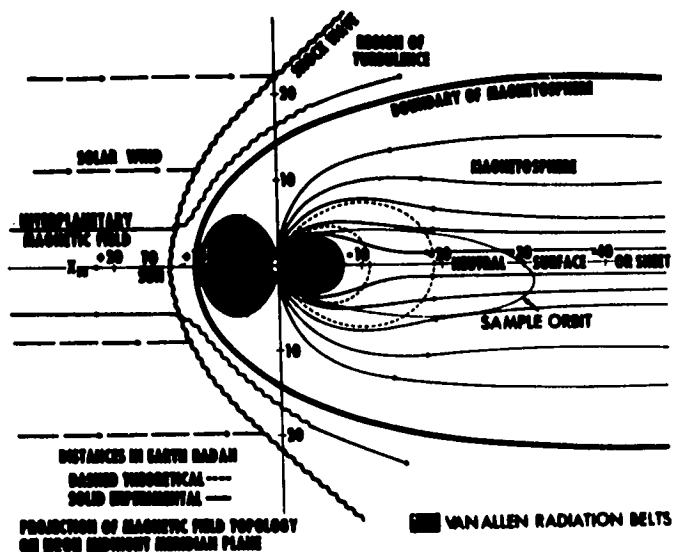


Fig. 6. Illustration of the interpretation of the IMP 1 magnetic field data field topology within the noon-midnight meridian plane. The relative position of the neutral surface or sheet in the earth's magnetic tail and the corotating magnetic field lines supporting trapped particle motion are indicated. These include the classical Van Allen radiation belts. The collisionless shock and magnetosphere boundaries are extrapolated to the polar regions indicating a depression but the relative position of a polar neutral point and the size of the boundary are not experimentally determined. Cylindrical symmetry about the earth-sun line has been assumed for the boundary of the earth's magnetic tail in this presentation (after Ness (1965)).

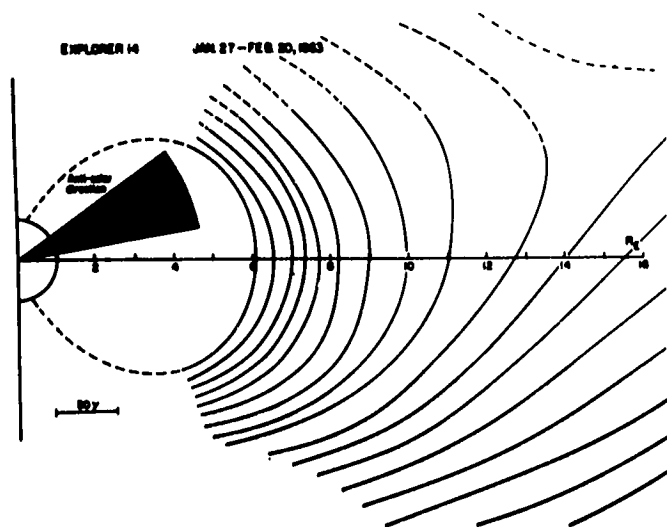


Fig. 7. A schematic representation of the magnetic lines of force projected upon a magnetic meridional plane as observed by Explorer XIV near local midnight (after Cahill (1965)).

Tail Field of
15γ 'Beyond' 12 RE

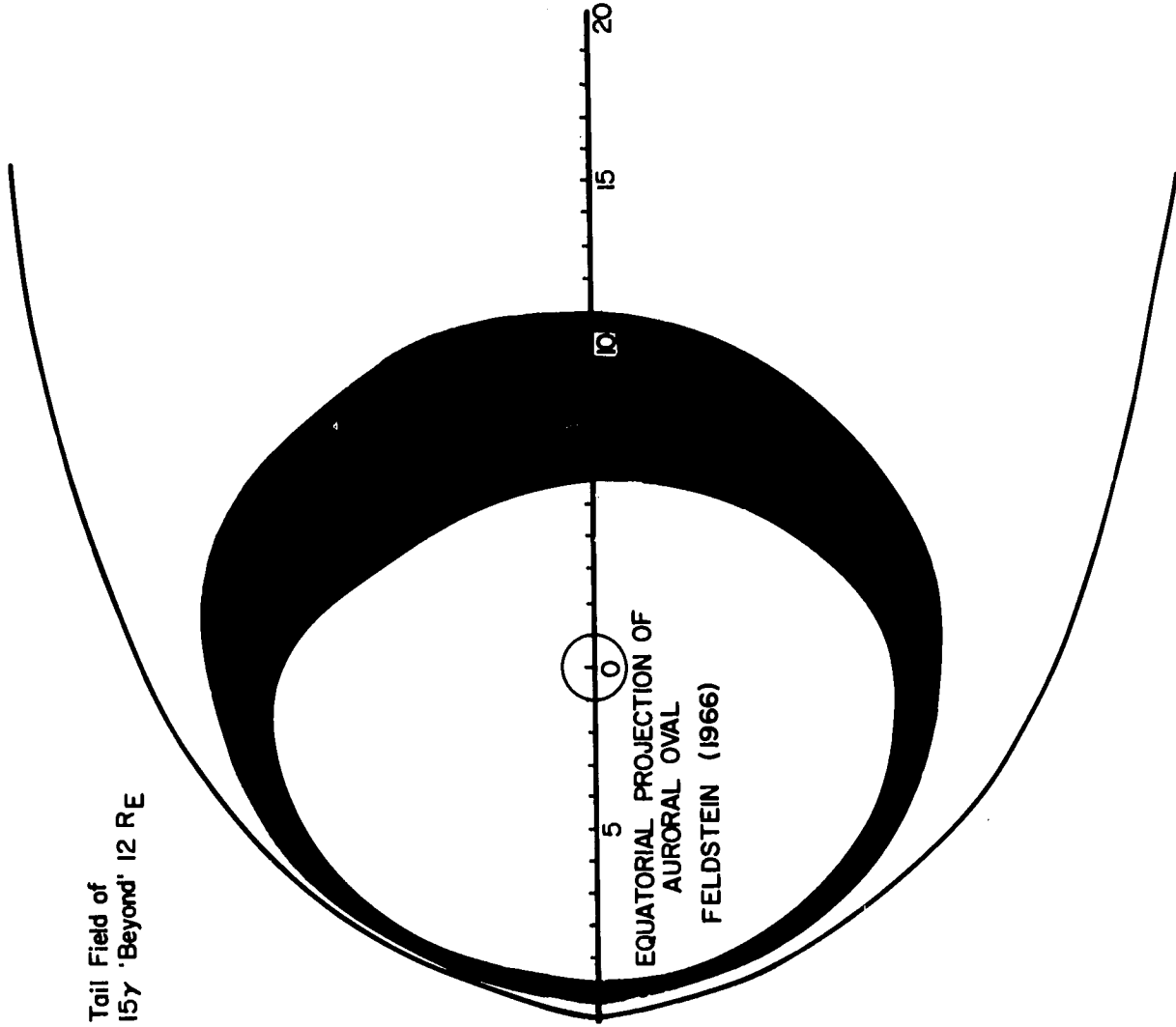
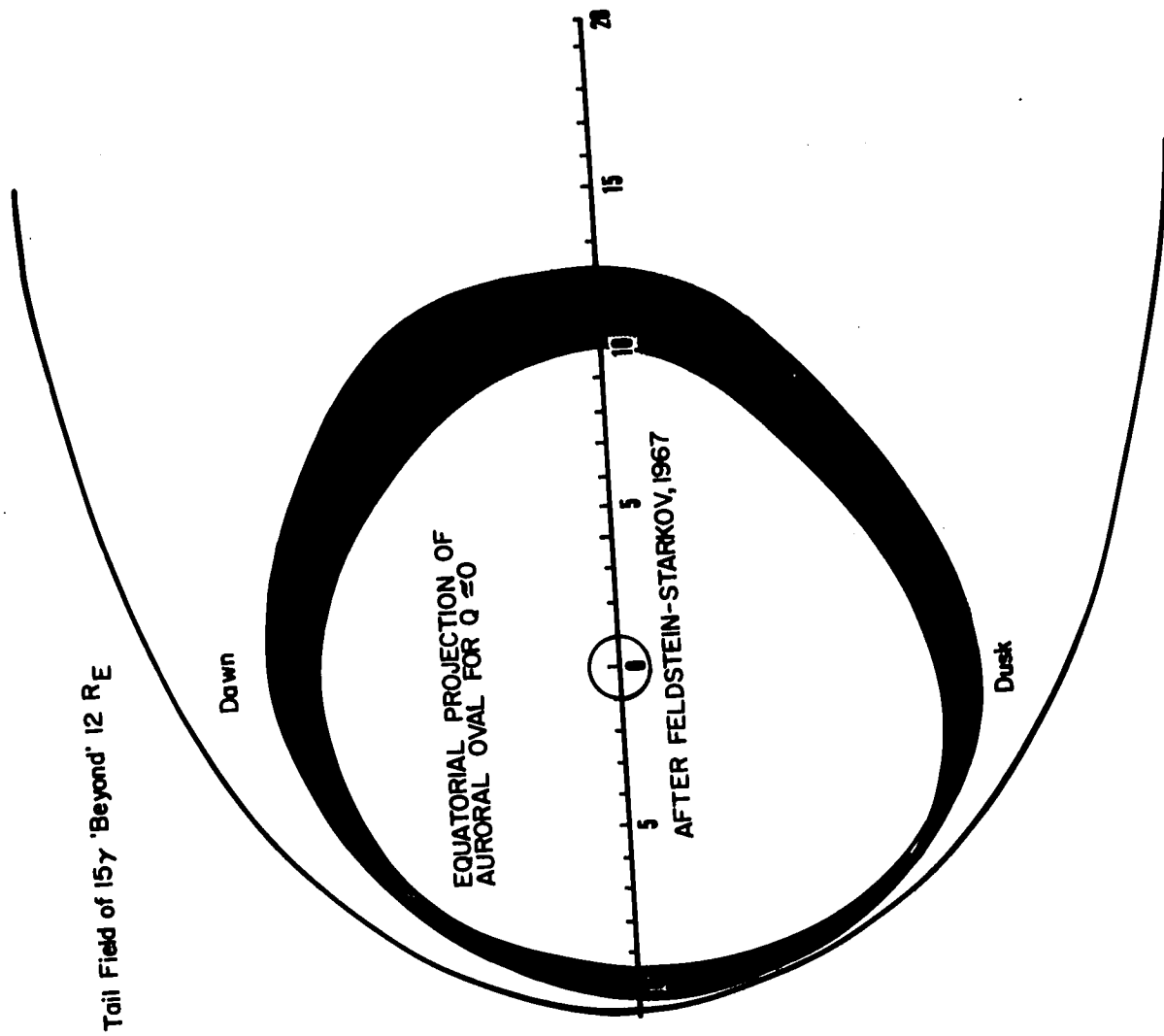


FIGURE 39



Tail Field of 15γ 'Beyond' 12 RE

FIGURE 40

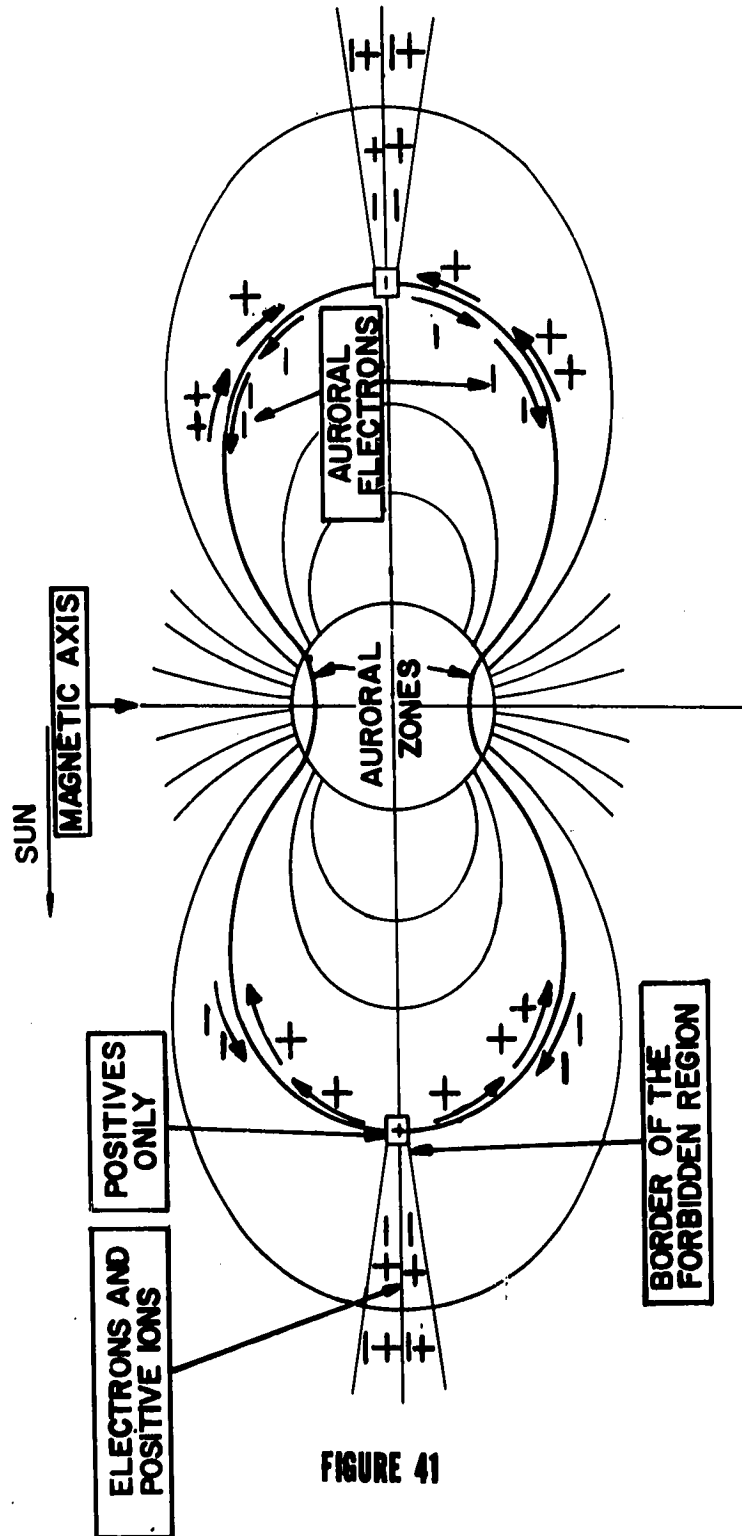


FIGURE 41

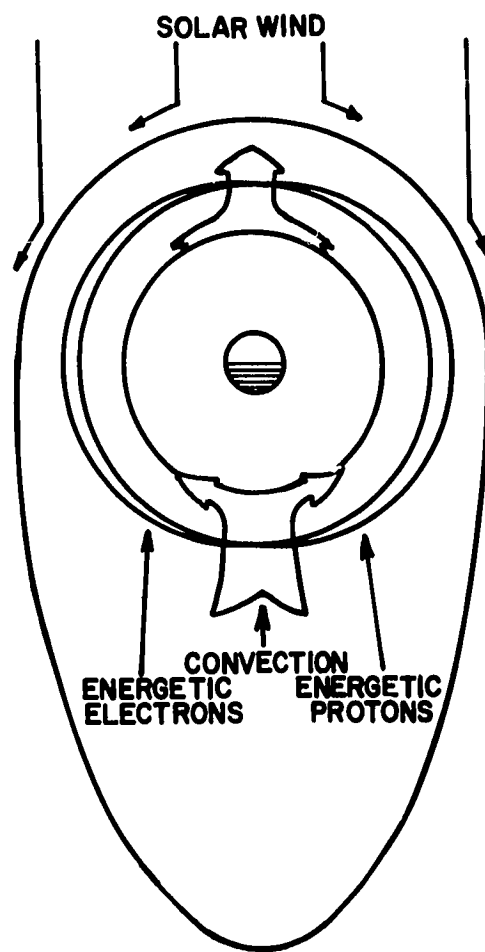
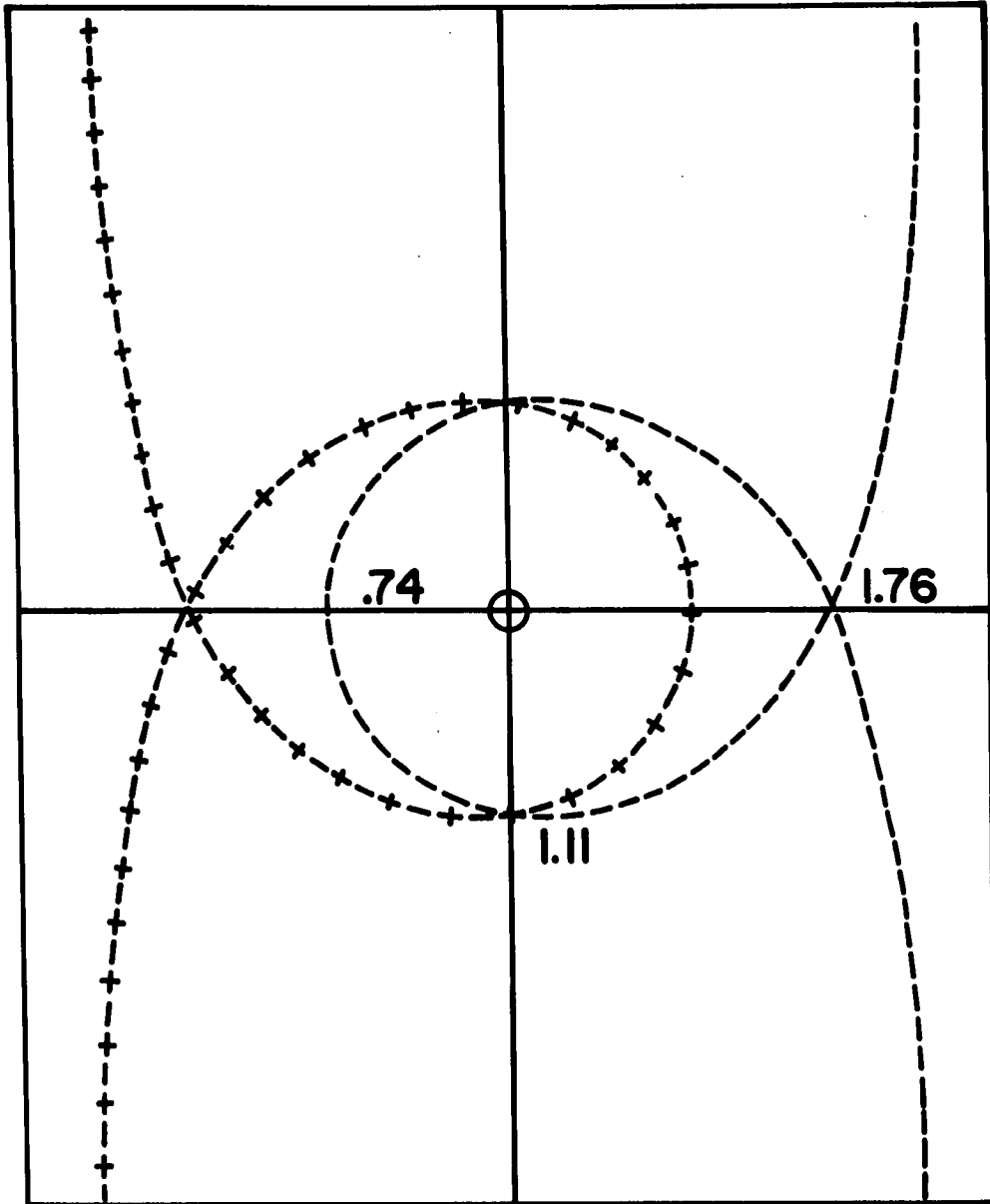


FIGURE 42



In units of L where

$$L = 5.3 R_E \left[\mu (100 \text{eV}/\gamma) / E (\text{mv/m}) \right]^{1/4}$$

FIGURE 43

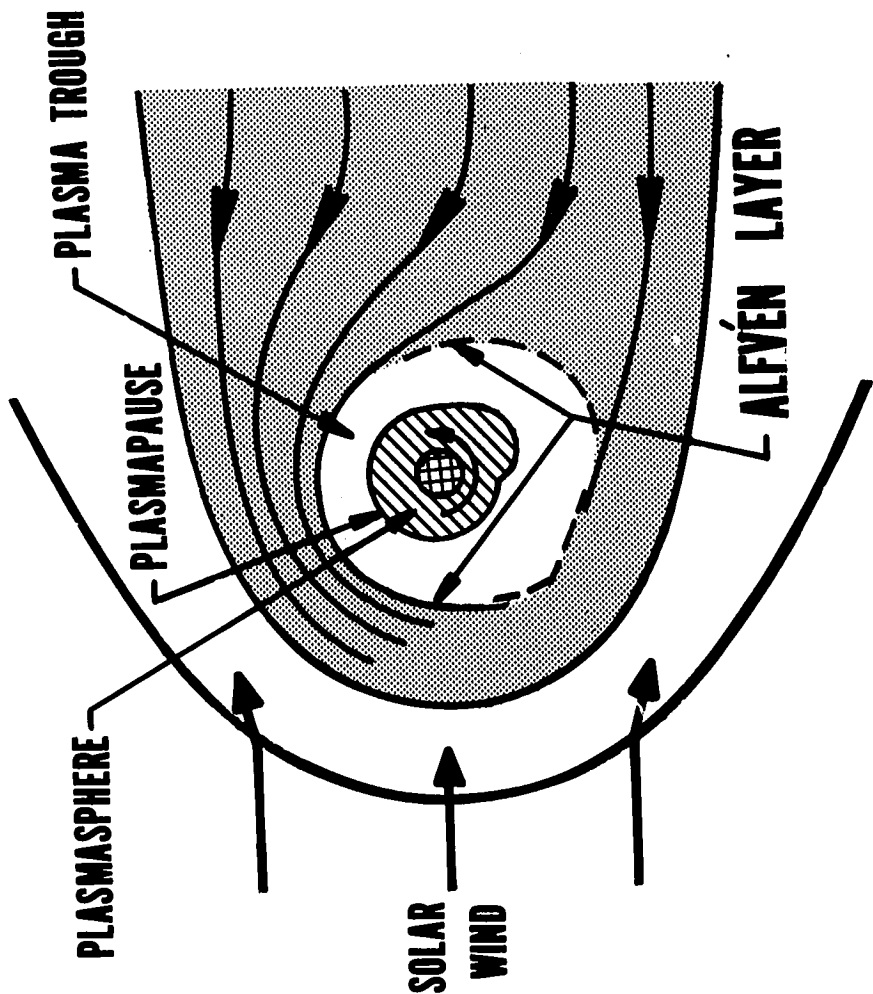


FIGURE 44

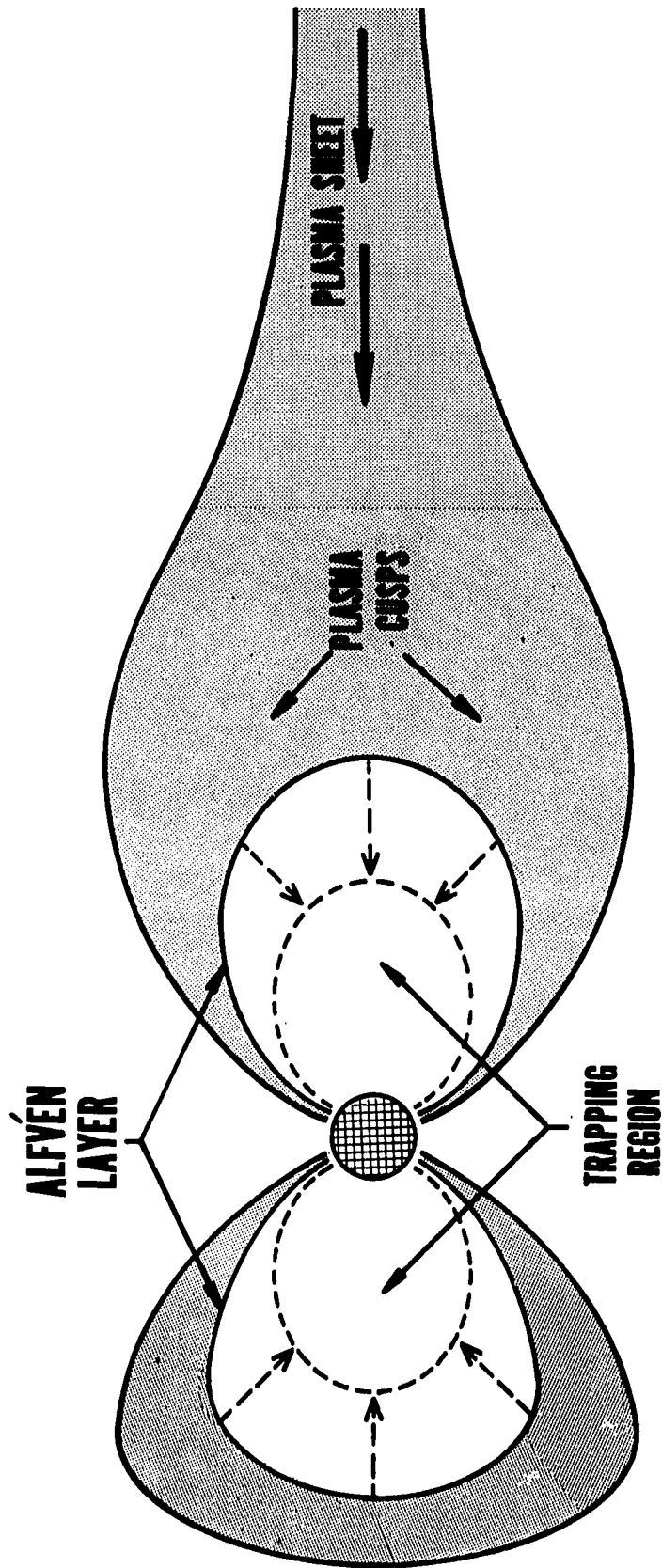


FIGURE 45

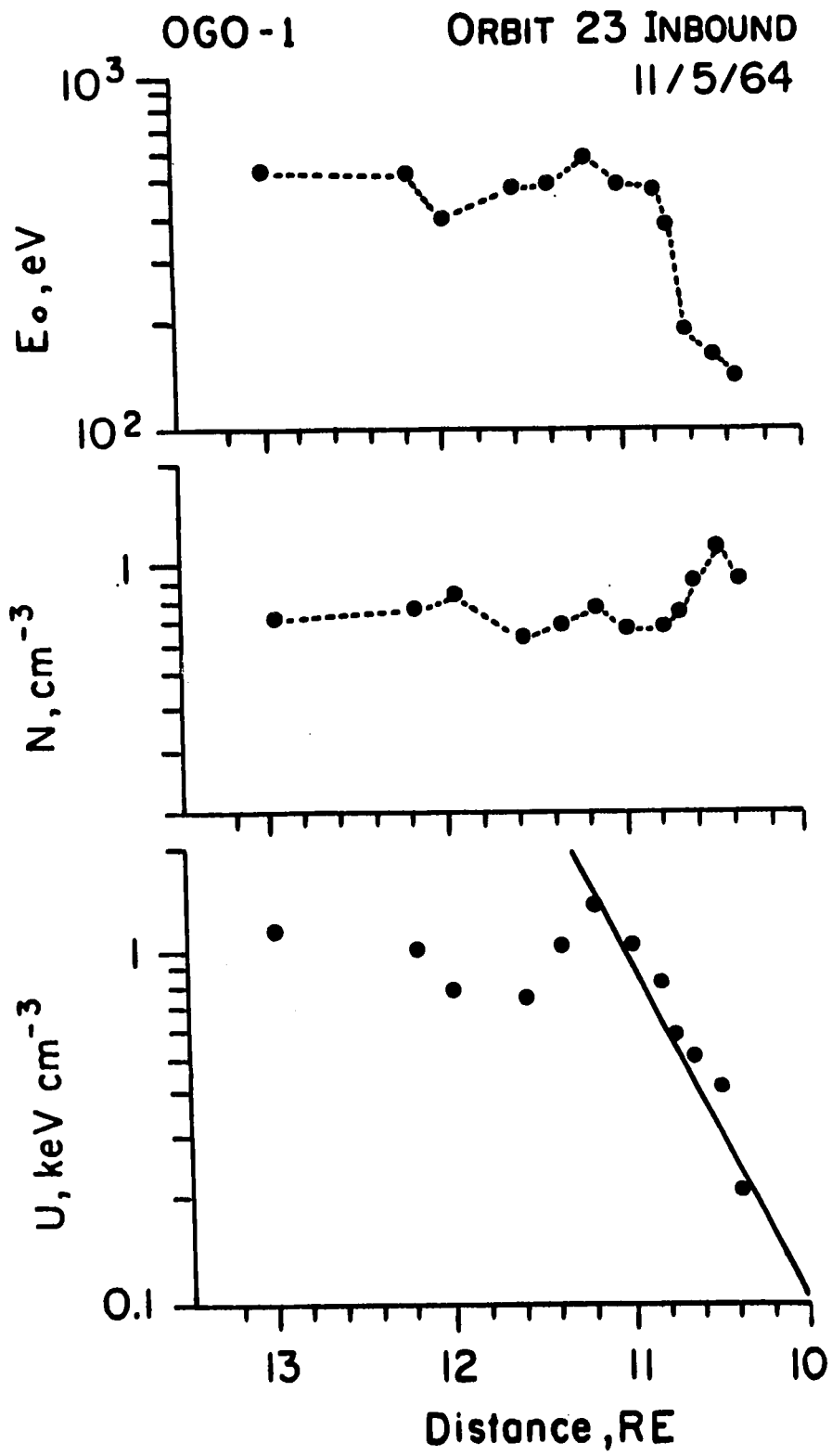
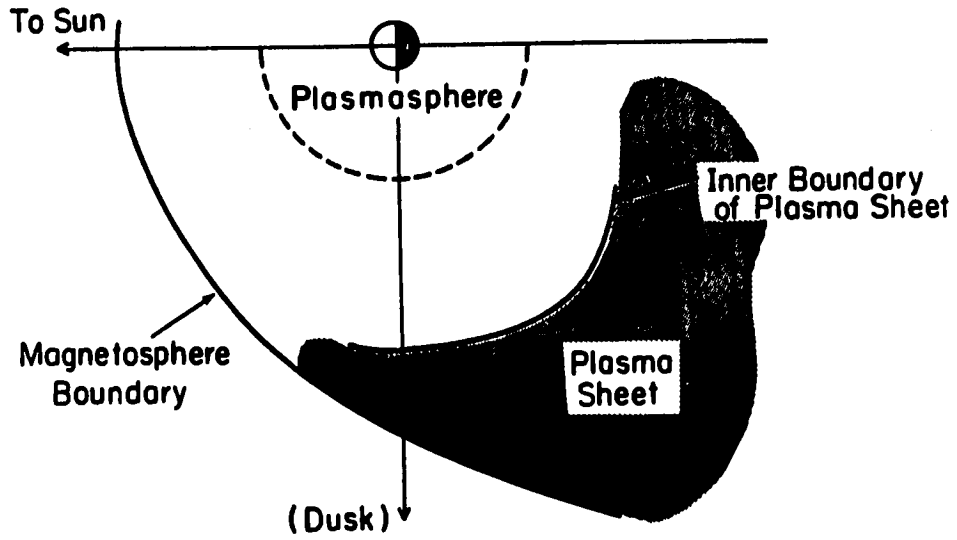


FIGURE 46

**SCHEMATIC PLASMA SHEET CONFIGURATION
(in equatorial plane)**

(a) During quiet times



(b) During magnetic bays

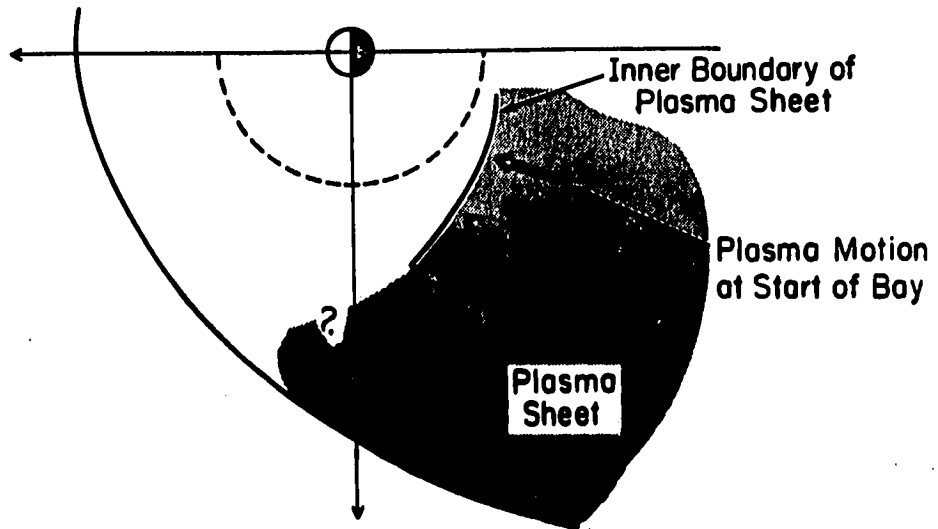


FIGURE 47

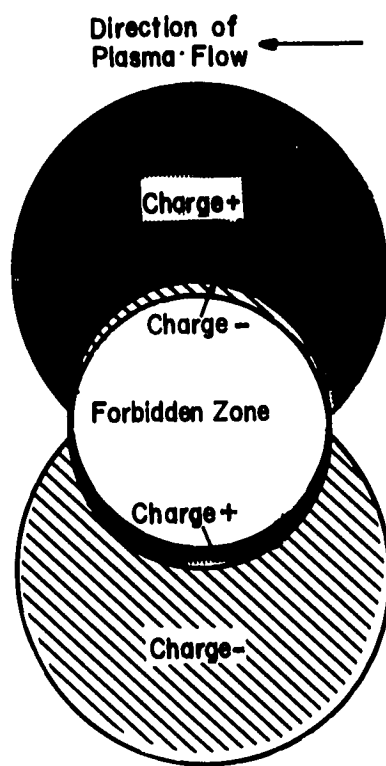


FIGURE 48

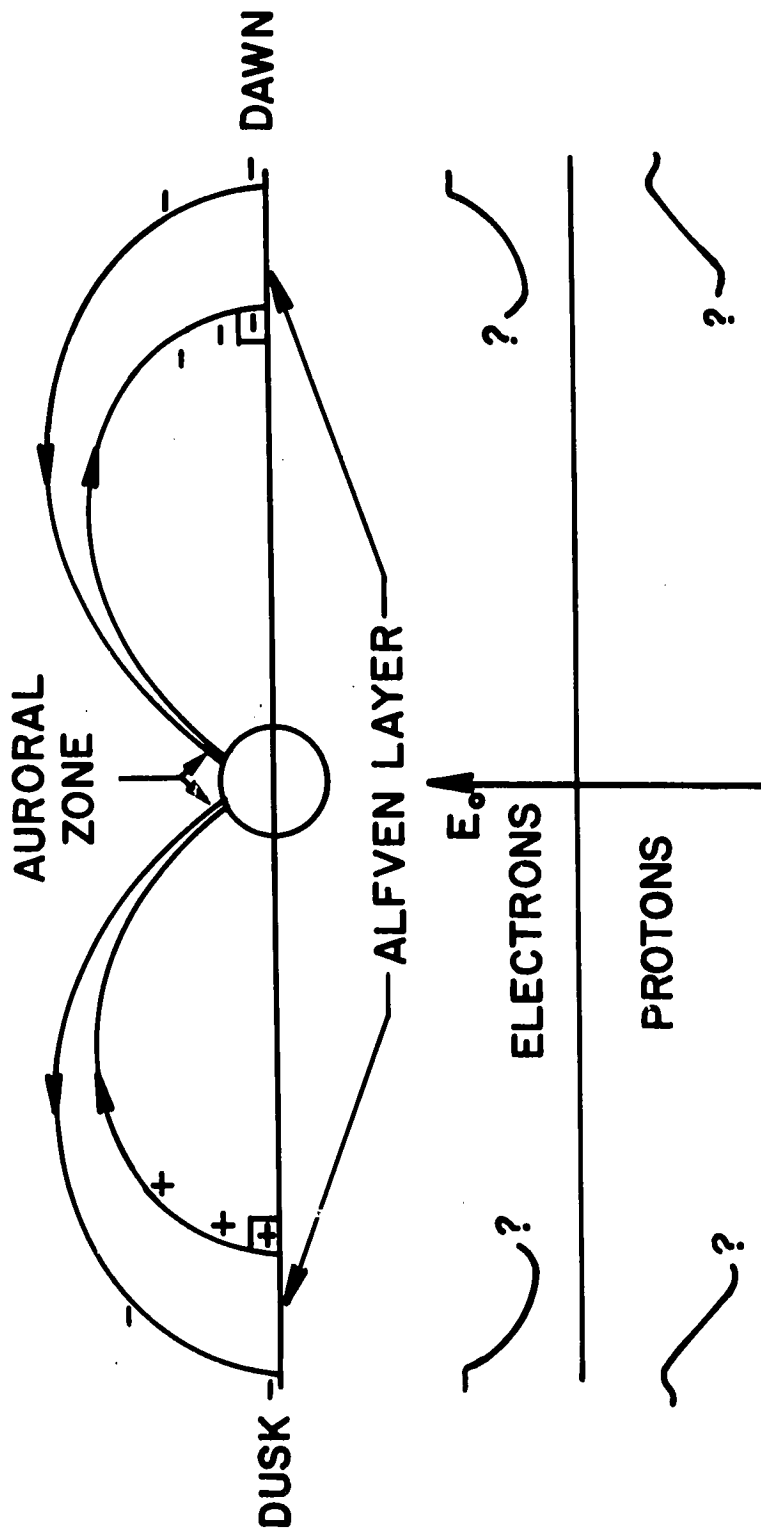


FIGURE 49

ELECTRON DIFFERENTIAL FLUX SPECTRUM

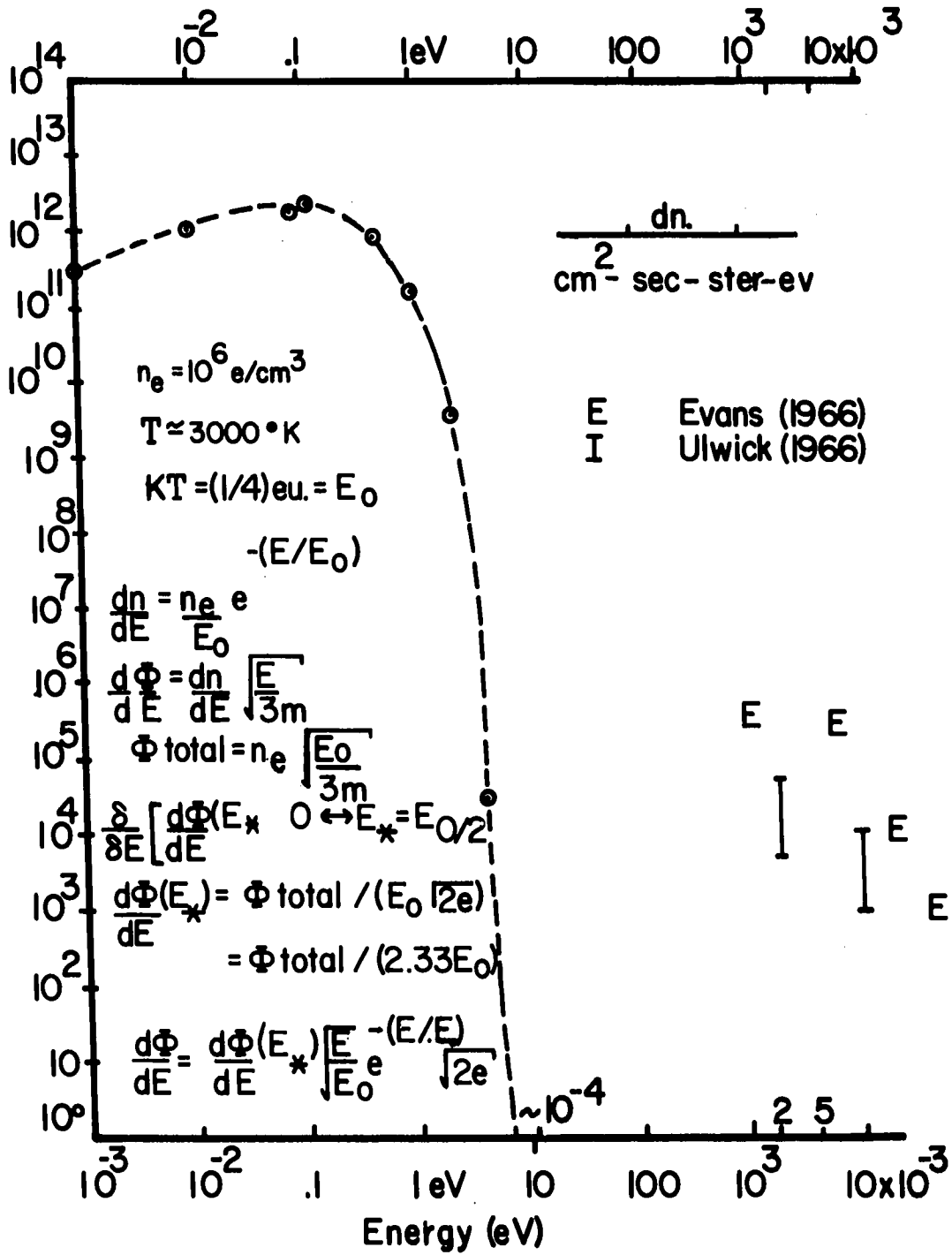


FIGURE 50

TWINS I B
PRECIPITATED AURORAL ELECTRONS

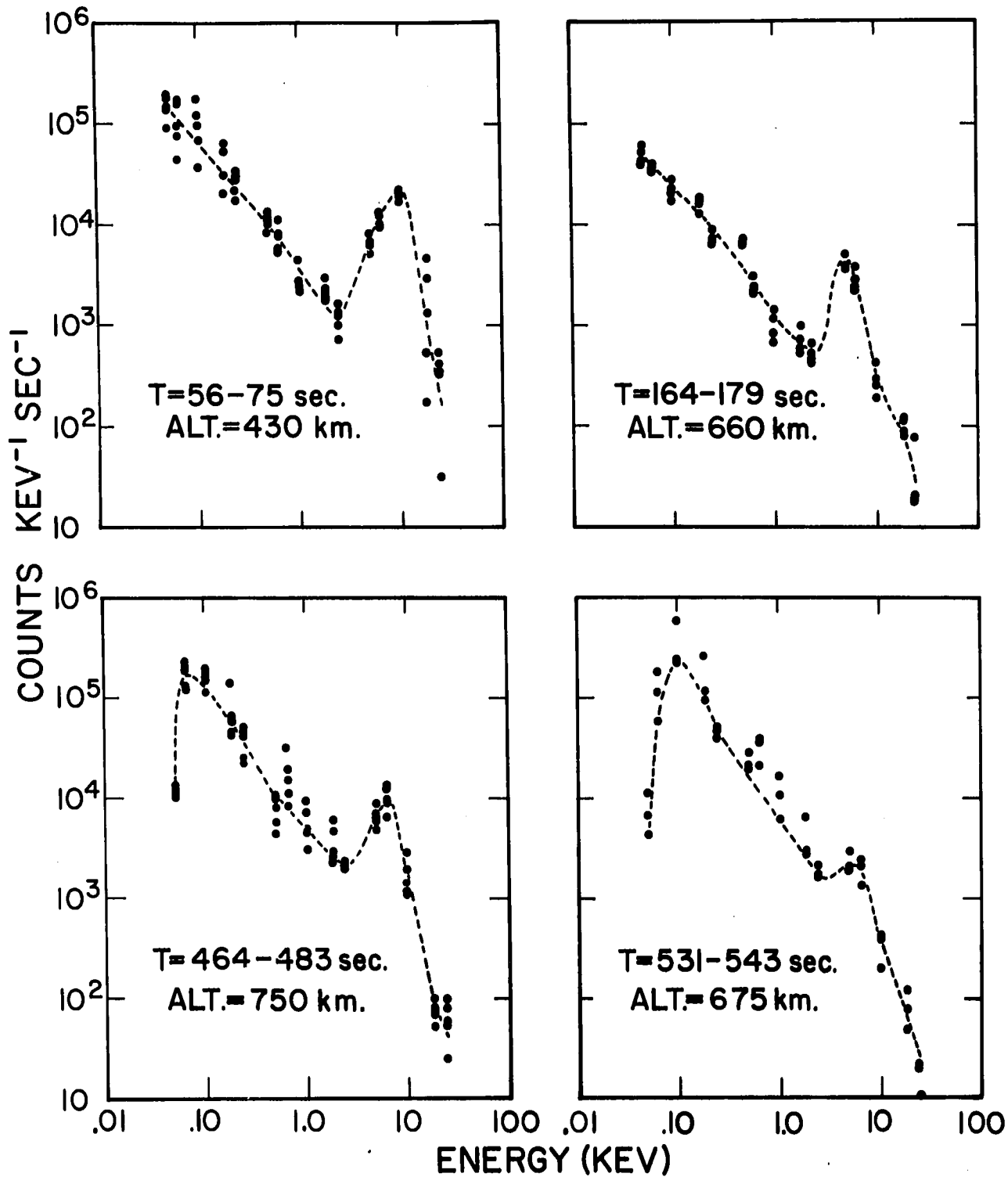


FIGURE 51